2016

Markerless Lung Tumor Trajectory Estimation from Rotating Cone Beam Computed Tomography Projections

Shufei Chen
chens8@vcu.edu

Markerless Lung Tumor Trajectory Estimation from Rotating Cone Beam Computed Tomography Projections

A thesis dissertation submitted in partial fulfillment of the requirements for the degree of Doctor of Philosophy at Virginia Commonwealth University.

by

Shufei Chen
Bachelor of Engineering

Advisor: Geoffrey Hugo Ph.D.
Associate Professor, Medical Physics Graduate Program
Department of Radiation Oncology

Virginia Commonwealth University
Richmond, Virginia
May, 2016

Acknowledgement

I would like to thank my advisor Dr. Geoffrey Hugo for his guidance for all these years in the project. Especially the past few years, we have encountered some difficulties when I had health and mental issues. He has been very supportive and helpful for getting me back in track. I would not be able to accomplish this without his support.

I also want to thank my thesis committee members, Drs. Alan Docef, Jeffrey Williamson and Paul Keall for being supportive and offering helpful insights in the algorithm development, data analysis as well as the full picture of the field.

I would also like to thank Dr. Per Paulsen for providing algorithm for marker segmentation and 2D-3D transform, and Dr. Elisabeth Weiss as well as Nick Roman for contouring all the structures on the images. Special thanks go out to my colleagues and to my friends. Especially, I would like to thank Shana Ryman for offering great help, support and courage toward the defense.

Last but not least, I want to thank my parents Lanhua Luo and Aisheng Chen for their love, encouragement and understanding. This effort is dedicated to them, and to my sisters and brothers.

Table of Contents

List of Tables

List of Figures

List of Abbreviations

Active breathing control (ABC)

Analysis of variance (ANOVA)

Tumor-to-marker displacement (TMD)

Anteroposterior (AP)

Cylinder tumor template (CTT)

Clinical Target Volume (CTV)

Computed tomography (CT)

Cone beam computed tomography (CBCT)

Deformable registration (DIR)

Direct template-based matching (DTM)

Extended GTV (Ex-GTV)

External beam radiotherapy (EBRT)

Ex-GTV tumor template (EGTT)

Field of view (FOV)

Four-dimensional (4D)

Four-dimensional computed tomography (4DCT)

Gross Tumor Volume (GTV)

Image guided radiotherapy (IGRT)

International Commission on Radiation Units and Measurements (ICRU)

Linear accelerator (linac)

Markerless template matching-based trajectory estimation algorithm (MLTM)

Measure projection (MP)

Padded tumor template (STT)

Planning Target Volume (PTV)

Probability distribution function (PDF)

Radiotherapy (RT)

Root mean square error (RMSE)

Superoinferior (SI)

Three dimensional (3D)

Two dimensional (2D)

Tumor template (TT)

Varian Real-time Position Management (RPM)

Abstract

MARKERLESS LUNG TUMOR TRAJECTORY ESTIMATION FROM ROTATING CONE BEAM COMPUTED TOMOGRAPHY PROJECTIONS

By Shufei Chen

A dissertation submitted in partial fulfillment of the requirements for the degree of Doctor of Philosophy at Virginia Commonwealth University.

Virginia Commonwealth University, 2016.

Major Director: Geoffrey Hugo, Ph.D.
Associate Professor and Director, Medical Physics Graduate Program
Department of Radiation Oncology

Respiration introduces large tumor motion in the thoracic region which influences treatment outcome for lung cancer patients. Tumor motion management techniques require characterization of temporal tumor motions because tumor motion varies patient to patient, day to day and cycle to cycle. This work develops a markerless algorithm to estimate 3 dimensional (3D) lung-tumor trajectories on free breathing cone beam computed tomography (CBCT) projections, which are 2 dimensional (2D) sequential images rotating about an axis and are used to reconstruct 3D CBCT images.

A gold standard tumor trajectory is required to guide the algorithm development and estimate the tumor detection accuracy for markerless tracking algorithms. However, a sufficient strategy to validate markerless tracking algorithms is lacking. A validation framework is developed based on fiducial markers. Markers are segmented and marker trajectories are

obtained. The displacement of the tumor to the marker is calculated and added to the segmented marker trajectory to generate reference tumor trajectory. Markerless tumor trajectory estimation (MLTM) algorithm is developed and improved to acquire tumor trajectory with clinical acceptable accuracy for locally advanced lung tumors. The development is separate into two parts. The first part considers none tumor deformation. It investigates shape and appearance of the template, moreover, a constraint method is introduced to narrow down the template matching searching region for more precise matching results. The second part is to accommodate tumor deformation near the end of the treatment. The accuracy of MLTM is calculated and compared against 4D CBCT, which is the current standard of care.

In summary, a validation framework based on fiducial markers is successfully built. MLTM is successfully developed with or without the consideration of tumor deformation with promising accuracy. MLTM outperforms 4D CBCT in temporal tumor trajectory estimation.

1. Introduction

1.1. Radiation Therapy for Lung Cancer

Lung cancer is the most commonly diagnosed and most lethal cancer worldwide.[1] In 2008 for instance, 1.61 million new cases of lung cancer were diagnosed, accounting for 12.7% of the total cancer incidences and meanwhile, 1.38 million deaths were caused by lung cancer, accounting for 18.2% of the total cancer deaths of the year. The survival of lung cancer patients is among the poorest of all cancer types. The overall five-year survival rate (typically used as the measurement of survival) regardless of treatment type is 15% for lung cancer patients in United States.[2] Surgical resection is the primary treatment choice for lung cancer patients with early-stage diseases, but the majority patients (about 80%) are medically inoperable. Radiotherapy (RT) is the primary treatment modality for inoperable patients, but the prognosis is poor. The 5-year survival rate of lung cancer patients who underwent RT-only treatment is about 5%-40% depending on the tumor stage [2,3]. Techniques to improve the RT treatment outcome of lung cancer are highly desired.

The goal of RT is to deliver a high enough radiation dose to kill the tumor cells while minimizing the dose to the normal tissue. To ensure targeting, radiographic imaging, normally a computed tomography (CT) image, is taken to model a patient's anatomy, including tumor and surrounding tissues at the simulation stage. Tumors are identified and delineated by physicians on planning CT images. Figure 1 shows an example of delineated tumor in CT images in a lung cancer case. A treatment plan is created based on the planning CT to meet the RT goal. Before

treatment, the patient should be setup as close to the planned position as possible. After setup, radiation beams are delivered according to the plan. RT is normally prescribed with multi-fractional doses meaning that a treatment course may last up to several weeks. The time lag between the simulation and delivery cause patient geometry variation in relation to the planned geometry (simulation stage) due to the existence of geometric uncertainties, especially for later fractions.

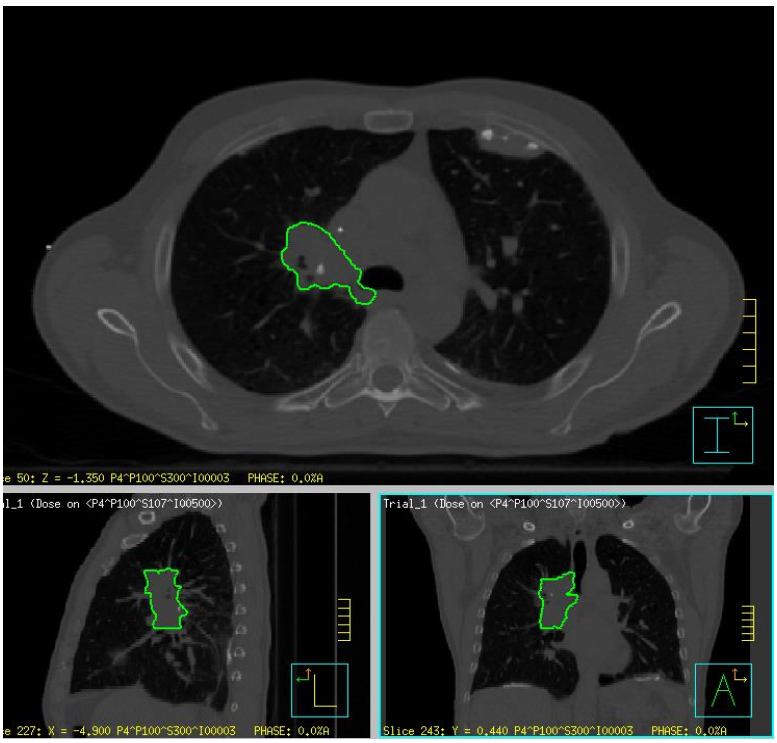

Figure 1. An example of tumor delineation in CT images for a lung cancer patient.

Geometric uncertainties are studied carefully for the purpose of precise targeting. Major sources of geometric uncertainties are the delineation uncertainty of the gross tumor volume (GTV) or other critical structures (e.g. organ-at-risk (OAR)), setup error, uncertain microscopic extension of tumor and organ motion [4]. In the delineation process, the limits in image quality of

imaging modalities (e.g. partial volume effect[5]), as well as inter-and intra-observer uncertainties impact the delineation accuracy and consistency. Delineating on multi-modality images with clear guidelines could help to improve the delineation uncertainty. Setup error is defined as the position difference between the positions of selected anatomical landmarks at the time of treatment in relation to their positions at planning [6]. Image guided radiotherapy (IGRT) and immobilization techniques help improve the setup accuracy, which is about 2-4 mm in the thoracic region[7-10]. To address Microscopic extension of tumor beyond that visualized on the imaging modalities, a margin added to the GTV to create a clinical target volume (CTV) [11,12]. Another major source of geometrical uncertainty is organ motion. Organ motion is defined as the organ position change with respect to the bony anatomy. Interfractional organ motion such as the baseline variation in the location of the respiratory trajectory relative to the bony anatomy is similar in magnitude to bony setup errors and is managed by IGRT[13-15]. Intrafractionally, respiration is an important factor that influences the improvement of treatment outcome in lung cancer because respiration introduces large intrafractional tumor motion during the treatment. Tumor motion at the thoracic region may be greater than 2cm when the tumor is close to the diaphragm[16-18], substantially larger than other regions.

To account for geometric uncertainties, traditionally a safety margin based on the population statistics is added to the target to create planning target volume (PTV) to ensure target dose coverage as recommended by International Commission on Radiation Units and Measurements Reports (ICRU 50 and ICRU 62) [6,19]. The margin added should be large enough to maintain tumor coverage in the target region, while at the same time it should be as small as possible to spare normal tissue. The GTV to PTV margin is larger for lung cancer compared to some other

cancers because of the respiration-induced tumor motion, leading to a larger dose to normal tissue.

To safely spare (reduce dose to) the normal tissue without compromising dose coverage to the tumor is critical to improve treatment outcomes for lung cancer. Normal tissue dose is proportional to the prescription dose and irradiated volume. The irradiated volume of healthy tissue increases when the CTV to PTV margin increases. Hence, margin reduction is beneficial in two ways. On one hand, margin reduction reduces the dose to the normal tissue if prescribing the same dose to the target as in larger PTV margin plans. Reducing the prescription dose is normally not chosen as a way to spare the normal tissue, because the dose coverage of the target will not be enough to kill tumor cells. On the other hand, margin reduction enables safe dose escalation. Dose escalation has been reported to show improved local tumor control with less local failure and increased survival [20-25]. However, dose escalation also increases the risk (dose) to the OAR (e.g. lung, heart, esophagus, and etc.). A safe dose escalation prescribes higher dose to the treatment target while respecting the dose tolerance to the normal tissue. With a smaller margin (irradiated volume), the target can be prescribed with higher dose under the same dose tolerance of the normal tissue as larger margin plans. The increased dose effect to the OAR due to dose escalation is reduced by dose reduction from margin reduction. In sum, reduction of geometric uncertainties and the associated safety margin is crucial at achieving the RT goals, either improving treatment outcome or reducing normal tissue toxicity. Therefore, as an important component of geometric uncertainties in lung cancer, organ motion should be monitored and studied carefully.

Techniques to manage motion during treatment incorporate the tumor motion in the treatment planning or the treatment delivery. Treatment techniques such as breath-hold, respiratory gating, tumor tracking have been developed to manage the respiration-induce motion during RT treatment delivery.[26-30] Breath-hold techniques intend to deliver radiation beams to patients only during the breath-hold intervals. Patients hold their breath voluntarily or through active breathing control (ABC) during the treatment. The whole treatment requires several breath-holds. The treatment efficiency (time cost) depends on the patient's ability to hold their breath. Similar to breath-hold, respiratory gating involves periodically turning radiation on normally at the end-of-exhale phase (EOE) of a patient's breathing cycle. Reducing the beam-on intervals in breathing cycles improves the motion management. But patients are held on the treatment couch longer, causing more discomfort for sick patients and degraded treatment efficiency. Tumor tracking techniques propose to track the tumor movement with the radiation beam, requiring real-time knowledge of tumor locations and prediction accounting for system latency. However, limited knowledge of the real time tumor location is the major complexity preventing the routine implementation of tumor tracking clinically.

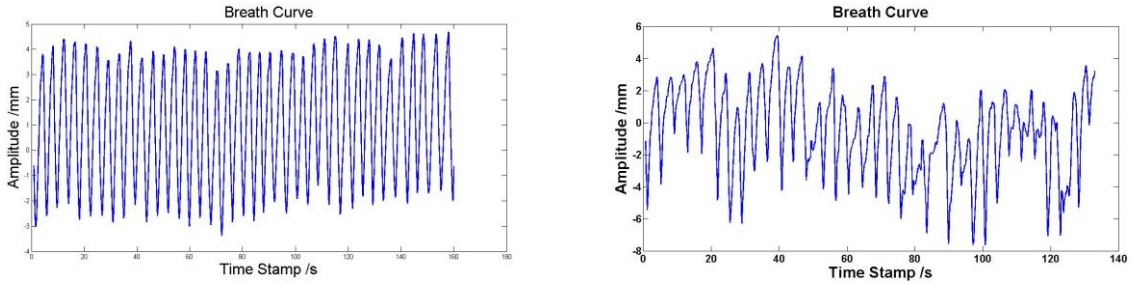

Figure 2 Two examples of breathing curves from RPM system for lung cancer patients. The left curve is more regular and periodic; the right curve is more irregular and aperiodic.

Incorporating temporal variations in patient specific geometric into the treatment planning process is an alternative approach to manage motion[31-39]. Probabilistic treatment planning is able to reduce the safety margin by generating a patient-specific field margin, which is modeled from patient-specific variations (mainly respiratory organ motion) in the repetitive imaging during treatment.[34] Four-dimensional (4D) inverse planning includes the temporal variation in the planning dose evaluation. The hypothesis is that the repetitive breathing motion is treated as random motion. The probability distribution function (PDF) of patient-specific respiratory motion is convolved to blur the dose distribution with respiration to approximate the dose distribution taking account full 4D anatomy in the respiration cycle[36-39]. Incorporating variability models into the treatment planning whether through adaptation or 4D inverse planning requires patient-specific characterization of the tumor motion. In sum, all these motion management treatment techniques require monitoring the tumor motion during simulation for treatment planning and during the treatment delivery for verification of the breathing pattern. The following section will discuss techniques to estimate tumor motion during planning.

1.2. Characterization of Respiratory Motion for Treatment Planning

Current techniques that are used to monitor the tumor trajectory can be grouped into 4 categories: external surrogates, implanted internal fiducial markers, internal anatomical surrogates and direct tumor estimation. The first three categories track the tumor motion indirectly through surrogates. And the last category directly estimates tumor motion from the tumor information. The following will discuss these 4 categories of motion characterization techniques.

1.2.1. External Surrogates

Signals from external surrogates such as tidal volume measured by spirometer[28,40] and abdominal skin surface displacement from external markers[41-43] are used to measure respiratory motion. A spirometer measures patient respiratory volume of air inhaled and exhaled by the patient through a mouthpiece with an electronic pneumotachometer. One common system measuring the abdominal surface displacement signal is the RPM system. The RPM system captures the anterioposterior motion of a block attached to the patient's abdomen through an infrared camera. The captured signal from the camera is imported to the linked computer and processed. A correlation model (normally linear) is applied to the external signal to estimate the internal target motion and position. The model relies on the assumption that the tumor position is consistently correspondent with the external surrogate signal. Several studies have been conducted to assess the correlation between the internal tumor motion and the surrogate signals (denotes as the internal/external correlation).[44-51] The internal/external correlation coefficient is high assuming linear correlation and the internal signal correlates slightly higher to spirometer signal than to the abdominal displacement signal[45-47,49] But the correlation is not temporally invariant, rather changes intra- and interfractionally. The correlation between tumor motion and external marker position is poor under breath-hold conditions[50]. Many studies observed time, phase shift, as well as amplitude mismatch between the tumor motion and abdominal displacement.[44,46,49,51] The internal/external correlation is sensitive to direction.[47,48] The best correlation is between the superoinferior (SI) tumor position and skin marker motion, but at the AP direction, the correlation is poor. The internal/external correlation varies with different tumor locations, skin marker locations as well as patient breathing patterns.[44,47,48] The

internal/external correlation coefficient changes day to day.[46,52] The external surrogates offer no indication of the interfractional baseline(location of the respiratory trajectory relative to the bony anatomy) variation [14,15,34] leading to different internal/external correlation at different days.

The respiratory tumor motion tracking using these external surrogates requires no acquisition of X-ray imaging allowing continuous tracking throughout imaging or treatment delivery. But due to the inconsistency of the inner/external correlation, external surrogate alone is an inaccurate indicator of tumor position and motion.

1.2.2. Internal Implanted Markers

Since external markers fail to correctly represent tumor motion, markers are implanted inside or near the tumor of the patient to represent tumor motion/position. The implantation of markers is through percutaneous needle insertion or bronchoscopy. Markers serve as reliable surrogate to locate or track tumors[53,54]. One type of marker is electromagnetic markers and the positions of markers are detected using a magnetic source and receiver coil array[55,56]. The other is radiopaque fiducial markers (normally gold markers) is detected from segmentation on planar X-ray images most commonly fluoroscopy[53,54,57-61].

The concern of tumor tracking through implanted markers affecting both electromagnetic and radiopaque fiducial markers is the limits and risks of marker implantation. Studies showed that marker implantation through percutaneous needle insertion introduces a risk of pneumothorax up to 45%[62-68], so performing implantation through needle insertion is not widely accepted by clinicians. Inserting markers via bronchoscopy is feasible and safe limited to peripheral-type lung tumors but not the central lung tumors.[59,61] The marker implantation may not be acceptable to patients especially those who might be expecting a ‘non-invasive’ treatment

modality with RT. Another concern that limits marker implantation is the marker migration[67-69], which leads to misrepresentation of the tumor position.

For tumor tracking with radiopaque fiducial makers, the additional dose to patient due to planar X-ray imaging is another concern. In order to reduce the frequency of X-ray imaging and thus the dose to patients, researchers introduce techniques which combine the external surrogate and internal fiducial together to model and predict the tumor position.[42,70,71] A linear model is built at the simulation to derive fiducial marker positions from signal of external surrogates. During the treatment stage, fiducial marker positions are used to update the model at certain time intervals. Updating the model with internal fiducial marker positions can overcome or moderate variations of internal/external correlation which tracking with external surrogate encounters. Since X-ray images are only acquired when updating the model, the imaging frequency and the patient dose is reduced.

1.2.3. Internal Anatomical Surrogates

Due to the risks and limits of tracking tumor with implanted fiducial markers, researchers have increased their interest in obtaining respiratory signal from the internal anatomical features on X-ray images. Diaphragm[72,73], carina[74,75] and other anatomical features[76] are analyzed in fluoroscopic images as internal anatomical surrogates for the estimation of the tumor motion. Studies have shown that diaphragm and carina are well correlated to tumor motion according to studies. A model obtained from the training data is applied to the trajectory of the anatomical to estimate the tumor trajectory. These surrogate anatomical structures are easy to detect in x-ray images. However, when these features are far apart from the tumor, one may need to enlarge the field of view (FOV) to include them in the images resulting in extra radiation dose to the patient.

Furthermore, the baseline shift of the tumor is difficult to be estimated by the feature surrogate modeling.

1.2.4. Direct Tumor Estimation

The limitations or risks of tumor trajectory tracking using external surrogates, implanted marker surrogates as well as internal anatomical surrogates, leads to the research interest in direct the tumor trajectory estimation from the tumor mass. This category is separated into 2 groups. One group is 4D tomography such as four-dimensional computed tomography (4DCT). The other group estimates instantaneous tumor positions in sequential 2D image datasets and the proposed method in this dissertation belongs to this group.

4D Tomography

In the thoracic region, respiratory correlated imaging acquisition techniques, such as 4DCT[77-79], 4D cone beam computed tomography (CBCT)[80,81] are performed to reduce the uncertainties and artifacts induced by the respiration-induced organ motion. A 4D scan consists of a set of three dimensional (3D) images reconstructed from two dimensional (2D) images at multiple phases (normally 10 phases) of the respiratory cycle. 2D images are sorted into different phases by analyzing a respiratory trace, which is simultaneously obtained as the 2D images by external surrogates. The determination of phase is based on either the amplitude or the phase angle. Phase angle is defined as the fraction of time between user-specified phases of breathing. For example, if end-of-inhale is phase 0% of the breathing cycle, end-of-exhale is around 50% to 60%. Tumor is delineated on each 3D phase images and one mean tumor position is obtained for each phase. The trajectory of the tumor motion is formed by these phase

mean tumor positions. Thus, the tumor motion extracted from 4D tomography is an average of all respiratory cycles.

The major disadvantage of 4D tomography is that the output is a single tumor position for each phase of 3D image. However, the tumor motion is not simply periodic but it suffers from cycle to cycle variation and shift of the mean or exhale tumor position (drift)[13,17,82] as shown in Figure 2. Output cycle from 4D tomography cannot provide accurate information to estimate cycle-to-cycle variations and drift. Hence, instantaneous tumor trajectory needs to be estimated in order to accurately measure these variations.

Direct Instantaneous Tumor Estimation

To directly investigate the instantaneous tumor positions, the intensity of the tumor mass is analyzed by tracking[83-85] and gating[86-88] in fluoroscopic images. Support Vector Machine (SVM)-based[87], template-based[83] and optical flow-based[84] algorithms are implemented to obtain the tumor positions directly from the X-ray images. Fluoroscopy provides two dimensional (2D) images of the patient, and thus dual fluoroscopy is required in order to obtain 3D tumor trajectory. However, the dual fluoroscopy imaging causes double dose to the patient and most clinics do not have the modality available. Hence, researchers have investigated tracking in single-imager mounted to the treatment gantry, e.g. linac-integrated cone beam computed tomography (CBCT), which provides rotational images (projections) of the patient enabling the reconstruction of the 3D trajectory. CBCT is widely used in IGRT to assist patient setup, plan evaluation, and adaptive therapy. Many clinics have already installed CBCT in their treatment rooms. Using the projections from the CBCT acquisition already taken in the patient setup to obtain tumor trajectory requires no extra dose to the patient.

One method utilizing the CBCT projections to obtain tumor trajectory information is to reconstruct the 3D anatomy at each time point when a projection is acquired, a method termed 'projection to volume'[89-93]. The method proposes a 4DCT reconstruction technique by deforming a prior source CT to match the measured projections. The technique works well under simulated conditions, but for actual CBCT data from free-breathing patients, the implementation of the 4D deformation model will be much more complicated. Estimation tumor trajectory in CBCT projections is simpler and potentially easier for clinical implementation than the project to volume techniques.

Some studies implement techniques such as Amsterdam Shroud (AS) [81,94] and principal component analysis (PCA)[95] to extract breathing signal from the CBCT projections. AS technique acquires 1D breathing signals extracted from AS images where the SI motion is enhanced. A derivative image is created from the original projection image by computing the derivative along the SI direction. The derivative image is averaged horizontally resulting a 1D column bar for each projection and the 1D bars of all the projections are posted together to from the AS image. Breathing signals are calculated from the pixel shifts by aligning 1D column bars one by one. The technique works only well when there are distinct structures in the FOV (e.g. diaphragm), but there is no guarantee such structures in the view. The other idea of breathing signal extraction is to separate the breathing motion induced intensity changes from the gantry rotation induced changes. PCA technique can be used to separate different motion modes by selecting different principal component eigenvectors. The PCA analysis performed on projection images is more useful at determining breathing phase other than extracting full tumor motion trajectory. Yan ***et al***. implement the PCA on AS image as a more reliable technique compared to

AS[95] alone. The downsides of these techniques are that the breathing signals are 1D (SI direction) and more importantly, the signals do not directly indicate the actual movement of the tumor.

The proposed method template matching-based markerless tumor tracking (MLTM) estimates the full tumor trajectory which includes not only the breathing amplitudes but also the tumor locations. Studies[96-98] have evaluated small, parenchymal lesions such as those amenable to stereotactic body radiotherapy. Solid validation is only available in phantom cases. For the clinical patient cases, some studies rely on physician delineation at the projections as a ground truth[96], which is limited to comparisons in small datasets by the time-consuming nature of the segmentation. Other studies compare the result of the markerless tracking algorithm to an average target trajectory from 4D CBCT[97,98], which does not allow for evaluation of the quality of the tracking on short time scales. Some studies[97,99] implemented a background subtraction step in projections before template matching. The idea is to subtract the digital reconstructed radiograph (DRR) generated from tumor-free 4DCT, where tumor was removed, from the projection image. I first proposed applying this technique in lung cancer patients in my AAPM presentation in 2010[100]. The subtraction technique enhances the tumor contrast. However, concerns include whether the enhanced tumor is the real tumor, for example whether the removal of tumor in either FBCT or CBCT to generate subtraction DRR creates an artificial boundary that could drive the template to an erroneous match.

1.3. Thesis Objective and Outlines

In this work, I extend the template matching-based tumor tracking on CBCT projections to larger lung cancer lesions (late-stage disease) infiltrating the chest wall, hilum, or mediastinum.

The treatment for larger lesions is more challenging because the large volume limits the dose that could be prescribed to the target within the respect of the normal tissue tolerance. The treatment outcome for late-stage disease is worse than early stages and thus treatment techniques for improving the treatment outcome are highly desired. Better understanding the tumor motion of larger lesions could result in smaller safety margins added to the target so that dose escalation could be applied to have better local control. However, larger lesions are more challenging cases to apply template matching-based tumor trajectory estimation. First, the treatment course lasts much longer for larger lesions (may be up to 7 weeks) than those amenable for SBRT (around a week), so the study of breathing pattern change throughout the treatment is more crucial for larger lesions. Tumor volume change as well as shape change in respect to the planning tumor due to the treatment response should also be taken into account in the template matching process. The other reason is that the soft tissue boundary may not be as clear as those well-defined small parenchymal tumors. Therefore, in this thesis, a markerless tumor trajectory estimation technique is developed for locally advanced tumors.

The primary goal of this thesis is the development and evaluation of a template-matching based markerless tumor trajectory estimation algorithm (MLTM) with clinically-acceptable accuracy (about 3mm) for lung tumor localization in CBCT projection images. MLTM will be compared against the clinical standard which is the 4D CBCT to see whether the technique can improve the tumor localization. Four specific aims are introduced to achieve this goal.

(1) The first aim is to develop and evaluate a validation framework to assess MLTM because a reliable validation method is lacking for direct tumor tracking. A validation method based on markers is built from marker segmentation on projection images. Tumor-to-marker displacement

is used to transform the marker trajectory to the tumor trajectory as the reference. Different approaches to calculate tumor-to-marker displacement is evaluated and an appropriate approach is selected to build the validation framework.

(2) The second aim of the thesis is to achieve clinical acceptable accuracy for MLTM with minimal tumor shape and volume change. How to create templates that are best suitable for template matching on projections is an important issue to solve. Template matching on rotating gantry images is challenging. The template matching may not get the true matching for some gantry angles. In this case, a prediction method is needed to guide the matching process. The expected outcome of this goal is an appropriate approach of template and a prediction method that could guide the template-matching.

(3) Patients studied here undergo multi-fractional RT which takes up to 7 weeks to complete the treatment. For later fractions, tumor shape and volume changes are no longer negligible. Therefore, the third aim of the thesis is to adapt the MLTM algorithm account for tumor shape and volume changes with adequate accuracy. Affine transformation and B-spline deformable registration is performed to the planning fan beam CT (FBCT) to transform the planning tumor to the daily tumor. The results of these two registrations are compared to the original method. An approach of registration with the best results is selected.

(4) The clinical standard of tumor trajectory estimation method is 4D CBCT. This work claims to outperform 4D CBCT and a study should be conducted to support this statement. Thus, the fourth aim of the thesis is to analyze the accuracy of the MLTM algorithms and compare it against 4D CBCT.

The outline of the thesis is described as follows. The validation framework and its accuracy estimation are covered in Appendix I and Chapter 2. The development of MLTM despite of tumor shape and volume change is taken place in Appendix II and Chapter 3 and with the existence of significant tumor shape and volume change in Chapter 4. The tumor trajectories obtained from MLTM are compared against clinical standard (4D CBCT) in Chapter 5. Finally in Chapter 6, results of previous chapters are discussed and concluded, and the further direction is suggested.

Appendix I and Appendix II are manuscripts reporting on the first two specific aims in this work. Subsequence chapters supplement the appendices with further details and discussions on the project development and analysis. It is intended that each appendix to be read prior to its corresponding chapter.

2. Validation Framework

2.1. Introduction

A gold standard tumor trajectory is required to guide the algorithm development and estimate the tumor detection accuracy for the MLTM algorithm. However, a sufficient strategy to validate markerless tracking algorithms is lacking. Instead, some validation studies[96] rely on manual segmentation of the target in the projections themselves as a reference, which is limited to comparisons in small datasets by the time-consuming nature of the segmentation. Because a CBCT scan contains about 600 projections (free breathing CBCT) up to 2400 projections (4D CBCT), it's impractical to manually delineate all the projection images. Other studies compare the results of the markerless tracking algorithm to an average target trajectory from 4D CBCT[97,98], which eliminates the time dependent motion pattern variation such as baseline drift and cycle to cycle variation not allowing for evaluation of the quality of the tracking on short time scales. Approaches such as external surrogates and internal anatomical surrogates are not considered due to the deficiency stated in section 1.2.1and 1.2.2. In this work, implanted fiducial markers are used to generate reference tumor trajectory because implanted markers can serve as reliable surrogates for tumor motion detection.

It is suggested to read Appendix I first, then proceed to read the remainder of this chapter. A validation framework to generate a gold standard tumor trajectory from implanted fiducial

markers is introduced in Appendix I. And the current chapter emphasizes on the rationale of the framework formation.

2.2. Patient Database

Table 1. Patient and marker characteristic.

Patient	Stage	Location	GTV (cm^3)	Markers Implanted	Markers Detected
1	T4N3M0	RUL	88.9	2	2
2	T4N2M0	Right Hilum	30.3	3	4
3	T4N2M0	Right Hilum/RLL	58.3	3	2
4	T3N1M0	LLL	42.7	2	1
5	T3N2M0	Right Hilum	144.2	3	5
6	T2N3M0	Left Hilum	46.2	2	1

As in Table 1, 5 patients with either a stage IIIA or IIIB pathologically-confirmed non-small-cell lung cancer (NSCLC) are studied in this dissertation. All the research work in this thesis is performed on these 5 patients. Patients were implanted with fiducial gold markers (Visicoil, RadioMed Corporation, Tyngsboro, MA). 2 to 3 fiducial markers were implanted via bronchoscopy in tumor or lymph node regions for each patient. The numbers of markers implanted and visible are summarized in Table 1. The discrepancy of the marker implanted and marker detected in the projections may due to marker breakage and marker migration. All patients were treated with 3D conformal RT (62.6-70 Gy) with standard fractionation (1.8-2 Gy, five days per week). A respiration-correlated 4D FBCT (Brilliance Big Bore, Philips Medical Systems, Andover, MA) is obtained as the planning CT for each patient before treatment. Slow gantry 4D CBCT were obtained at each treatment fraction of the treatment, denoted as daily CBCT, via a commercially available on board imaging device (Varian Medical Systems, Palo

Alto, CA) for each patient. The scan conditions were 125 kVp, 20 mA and 20 ms per projection with half-fan geometry. There are about 2400 projections in each 4D CBCT scan and they covered all 360 degrees of gantry rotation. Fiducial markers and primary tumor were contoured for all 10 phases of all 4D FBCT, and weekly (about 7 CBCT scans per patient) for 4D CBCT. Those weekly delineated 4D CBCT are denoted as weekly CBCT in the following chapters.

2.3. Background on 3D Medical Image registration

Currently, multiple radiological images are generally used to guide diagnosis and treatment in healthcare. A technique to accurately relate information in different images is required to fully exploit the image information for physicians and researchers. Image registration is the solution, which determines the spatial correspondence between two images of a scene. In the process, points from one image could find the corresponding points in the other image. The outcomes of registration include fusion information, transformation, change detection and object recognition.

Image registration provides a means to accurately relate information in different images, most widely used to align tomographic images in 3D space, e.g. aligning FBCT and CBCT. The most often used registration techniques assume a 'rigid body' meaning that the structure of interest deforms and distorts negligibly. This type of techniques is called rigid image registration. In reality, organs do deform substantially in images due to organ motion, treatment response and different imaging modalities. Non-rigid registration techniques that can compensate tissue deformation are of high requirement. The outcome of image registration is a major part of the research method in this thesis. In the rest of this chapter specifically, image registration is used

to obtain target positions without delineation, and the transformation is also employed to transform a structure of interest to match the target structure in Chapters 3 and 4.

2.3.1. Rigid Image Registration

The definition of rigid is that the distances between all points of the target image remain constant compared to the source image. The rigid transformation is 6 degrees of freedom for 3D images, including translation, rotation and reflection. Rotation is rotating an object about a fixed point without changing its size or shape; translation is moving an object in space without changing its shape, size or orientation; reflection is flipping an object across a line without changing its shape or size. Assuming a point f in the source image and the transformed position is f', the function to conduct the transformation is shown below:

$$f' = \mathbf{R}(f - c) + \mathbf{T} + c \quad (1)$$

where the matrix **R** is a rotation matrix, c is the center of rotation (usually the center of the image), and matrix **T** is translation matrix. The rotation matrix is parameterized by the Euler angles (one in 2D, three in 3D).

Rigid image registration can be accomplished automatically and manually. Automatic rigid image registration is used in routine clinical practice. The registration of the source and target images is obtained by iteration and comparison of various possible matches of the two images. The process is formulated as an optimization problem by a ranking function based on some physical considerations (correlation, mutual information and etc.). Manual rigid registration is also in popular use to compare images and it is employed in the following study of

this chapter. This process manually rotates and moves the source image around the target image and obtains the registration by comparing the critical features in the fusion images.

2.3.2. Affine Transformation

Affine transformation includes dilation, which expands and contracts an object without changing shape or orientation. An affine transformation is a transformation which preserves straight lines and ratios of distances between points on any straight line. Scaling, translation, rotation, reflection, shear, similarity transformations, spiral similarities as well as any combination and sequence of above are all affine transformations. The affine transformation adds scaling and shearing to the rigid transformation matrix leading to 12 degrees of freedom in the registration parameters for 3D images. The function of affine transform is shown below:

$$f' = \mathbf{A}(f - c) + \mathbf{T} + c \quad (2)$$

where other variables are defined the same as in equation (**1**) except the matrix **A** has no restrictions compare to matrix **R** meaning that the image can be translated, rotated, scaled, and sheared. Affine transformation does not increase the applicability of image registration dramatically relative to rigid body transformation, as tissues deform in more complicated ways. Therefore, affine transformation is not incorporated into the study of this chapter, but will be used in Chapter 4.

2.3.3. Deformable Image Registration

Deformable image registration (DIR) is more complicated compared to rigid registration and it models individual voxel dependent distortion, which can be made using either finite element model[101,102], B-splines[103,104], thin-plate splines[105,106], optical flow algorithms[107], or fluid

flow algorithms[108]. The process of DIR requires 4 components: an interpolator to sample the voxels, a transformation to specify how a volume can change during the various steps in the optimization, a similarity metric (such as mutual information, cross correlation, and etc.) to measure the score for optimization, and an optimizer to find the best possible solution. The optimizer compares the scores given by the similarity metric for the evaluated transformed spaces and obtains the best solution by marching over a subset of solution space.

The DIR components chosen in this dissertation are B-Spline interpolator, B-Spline transformation, mutual information, and gradient decent optimizer. The software used to perform DIR is *Elastix*[109,110]. B-spline DIR can represent smooth and continuous motion which is anatomically realistic and it is computationally efficient because changes to one region do not affect the remainder of the transform since B-splines only have local support. B-spline is short for "basis spline". A function is represented as a linear combination of basis functions.

$$v(x) = \sum p_i \beta_i \ (x) \tag{3}$$

Where β_i is a piecewise cubic polynomial, p_i is a scaling factor. Noting F_i is the fixing image intensity at voxel i, and M_i is the moving image intensity. In the registration process, mutual information (MI) was calculated and used to optimize the B-spline coefficients. The registration contains a global transformation and a local transformation. The global transformation describes the overall motion of an object which can be estimated simply by rigid registration. The local transformation defines the deformation of the object. The idea of the transformation is to deform the object by manipulating an underlying mesh of control points. The control points are defined on the fixed image and they are normally on a regular grid. The transformation of a point can be

computed from only a few surrounding control points and it benefits the modelling of the local transformation and enables fast computation.

In this work, the average CT of the free breathing planning CT and average CBCT are registered and the resulting transformation is used to transform the phase images. The image quality of the CBCT phase images is poor and hence the average CBCT is used to obtain better registration results. The patient image data are stored in *Pinnacle* format and needed to transform to *MetaImage* (**.mhd*) as the input of *Elastix*. The spacing of the grid for defining control points is 8.0, 4.0, 2.0, and 1.0 voxels. The DIR is running at multi-resolution with down-sampling and the resolution pyramid is 8.0, 4.0, 2.0, and 1.0 voxels.

2.4. Validation Framework Formation

2.4.1. Framework Outline

The marker-based validation framework setup in Appendix I is summarized as following. For each scan of CBCT projections, markers are segmented in projections $p \in (1, 2, 3 \cdots N)$ using a MATLAB GUI developed by collaborators[111] , where N is the number of projections of the scan. The resulting marker trajectory is denoted as $\mathbf{M} = \{\vec{m}_1, \vec{m}_2, \vec{m}_3, \cdots \vec{m}_N\}$, where $\vec{m}_p$ is the marker position vector at left-right (LR), anterior-posterior (AP), and superior-inferior (SI) directions. Markers are implanted inside the tumor, but the marker centroid does not necessarily represent the tumor centroid and an offset often exists. Tumor-to-marker displacement (TMD) is added to $\vec{m}_p$ for the generation of the reference tumor trace $\mathbf{R} = \{\vec{t}_1, \vec{t}_2, \vec{t}_3, \cdots \vec{t}_N\}$ where vector $\vec{t}_p$ is the tumor position vector. TMD can be computed from the mean tumor positons minus the mean marker position of the marker trace segmented in the CBCT projection images. The mean tumor

positions can be obtained either from contours on the reconstructed CBCT or image registration of an image with known tumor positions to the CBCT.

The relationship over the treatment course between marker and tumor is not well known and TMD is considered as the factor to represent the relationship in this work. One strong factor influences TMD is marker migration. In a treatment, normally about 3 markers are implanted to each patient and the distances between the markers are checked to detect possible migration[112]. Significant marker migration (e.g. migrating into the pleural space) normally happens within 6 days after the insertion of the marker [67]. Marker positions are stable for 2–4 weeks from the beginning of radiotherapy[112]. With the exception of migration, TMD changes slowly, continuously due to the slow, continuous change in tumor volume and shape during therapy. Thus, a linear relationship should reasonably model for the marker and tumor relationship as shown in Figure 1 of Appendix I. A linear model for each patient is obtained through linear regression which minimizes the sum of squared residuals and leads to a close expression for the estimated value $\boldsymbol{\delta}$ of TMD.

$$\boldsymbol{\delta} = \boldsymbol{\alpha} + \boldsymbol{\beta} d \tag{4}$$

where d is the scan day of the CBCT relative to the planning CT which is day 1, $\boldsymbol{\alpha}$ and $\boldsymbol{\beta}$ are variables computed from the minimization of the sum of squared residuals. This estimated value $\boldsymbol{\delta}$ is used to obtain non-delineated scans. However, due to tumor motion and deformation, marker position may not be reliable after 1 month[112]. For example, Patient 6 demonstrates a non-linear relationship in TMD at the last measurement after 1 month of treatment, as shown in Figure 1(f) of Appendix I. In this case, marker migrates and TMD should be calculated directly other than through equation (**1**).

2.4.2. TMD Approaches

For the calculation of TMD, besides physician delineated tumor contours, tumor centroid positions can be obtained from image registration with aligned critical structures. Different approaches are compared to decide which approach is compatible with delineated contours. As mentioned in Section 2.2, only weekly CBCT scans were delineated by physicians in our datset, so TMD for each approach is calculated and compared against contour based method on weekly CBCT scans. TMD calculated from delineated tumor contours is denoted as TMD_c. In image registration approaches, the tumor positions of the daily CBCT are obtained by transforming the known tumor positions from a delineated scan (either planning CT or CBCT).

Three image registration approaches were compared to TMD_c. The first approach is to manually align tumors (rigid registration) of the planning FBCT and the daily CBCT in the treatment planning system (Pinnacle), and the calculated TMD is denoted as TMD_rigid_tumor. The differences between the TMD_rigid_tumor and TMD_c are calculated for each weekly CBCT and the root mean square errors (RMSE) are listed in Table 2. There are large discrepancies between the TMD_rigid_tumor and TMD_c due to registration errors caused by tumor regression, which is up to 60% volume reduction throughout the treatment course.

The other attempt is to rigidly register the nearest delineated CBCT to the daily unsegmented CBCT automatically by aligning tumors, and the resulting TMD is TMD_CBCT. The rationale behind this is to accommodate tumor deformation in the registration without the employment of deformable registration. The calculation is done on weekly delineated CBCT scans, and the transformed tumor position is also compared against the delineated tumor position in Table 3. The errors are significantly reduced compared to TMD_rigid_tumor. The last

attempt is to register the planning CT and the daily CBCT to the tumor through deformable image registration (DIR), resulting TMD_DIR. The errors of TMD_DIR as shown in Table 4 and they are similar to TMD_CBCT, slightly better. However, the errors of both attempts are still larger than the errors (1.2/1.6/2.6 mm at LR/AP/SI directions from Appendix I) of expected TMD, $\boldsymbol{\delta}$, estimated from the linear model built on TMD_c. The advantage of TMD_DIR is that it does not require physician delineation and could be automatic.

Table 2. RMSE of TMD_rigid_tumor.

Patient	LR/mm	AP/mm	SI/mm
1	2.0	1.3	2.0
2	1.0	0.7	2.5
3	5.1	2.0	6.0
4	4.1	2.3	2.7
5	4.5	6.1	4.4
6	10.0	4.8	5.7
Mean	5.3	3.5	4.2

Table 3. RMSE of TMD_CBCT.

Patient	LR/mm	AP/mm	SI/mm
1	1.2	0.6	1.2
2	2.0	1.9	2.3
3	3.0	0.4	1.8
4	2.0	0.3	1.9
5	1.1	2.0	2.1
6	4.0	4.5	4.9
Mean	2.4	2.2	2.6

Table 4. RMSE of TMD_DIR.

Patient	LR/mm	AP/mm	SI/mm
1	0.8	1.9	2.1
2	1.1	1.3	0.8
3	2.4	2.8	1.7
4	1.7	0.8	0.6
5	2.7	2.1	2.1
6	3.3	2.4	3.8
Mean	2.2	2.0	2.1

2.4.3. Intrafractional Consideration of TMD

TMD is not constant during breathing, and the difference between TMD at different breathing phases calculated from TMD_c is up to 5 mm with a standard deviation of 1.5 mm. However in this work, the marker trace was not corrected phase to phase. A mean TMD is computed for each CBCT scan and used as the correction factor to generate reference tumor trajectory from markers instead of phase to phase calculation of TMD. There are two reasons behind this. First of all, the goal of the validation framework is for application to both normal CBCT scans and 4D CBCT scans. Phase-to-phase computation of TMD is not available on the normal CBCT scans. Secondly, the delineation uncertainty is highly involved in the calculation of phase TMD. The image quality of the phase-specific image in the 4D CBCT is poor compared with the average image, leading to larger delineation uncertainty of the targets. Figure 3 shows two examples of the average cycles of tumor positions (TC) obtained from the first two delineated weekly 4D CBCT. Average cycles of marker trajectory (MS) generated from the direct marker segmentation in the projection images are also plotted as references. Even though the amplitude of tumor movement and marker movement may not be the same, they should have the same moving pattern, in other words when the amplitude of the marker movement increases, the amplitude of tumor movement should increase respectively. For patient 3, the amplitude of tumor movement increases as does the marker amplitude in the plots. However, in week 2 of patient 2, the amplitude of marker motion deceases compared to week 1 but the amplitude of tumor motion increases. Furthermore, the shape of the average cycle of tumor positions, especially TC2 for both patients, is not as expected to be a smooth curve. This is mainly due to

delineation uncertainties caused by poor image quality of CBCT phase image and observer uncertainties. The phase TMD obtained from the phase contours are not necessarily more accurate than a single TMD from the average position, therefore the average TMD is used as the correction factor for the whole CBCT scan in this work.

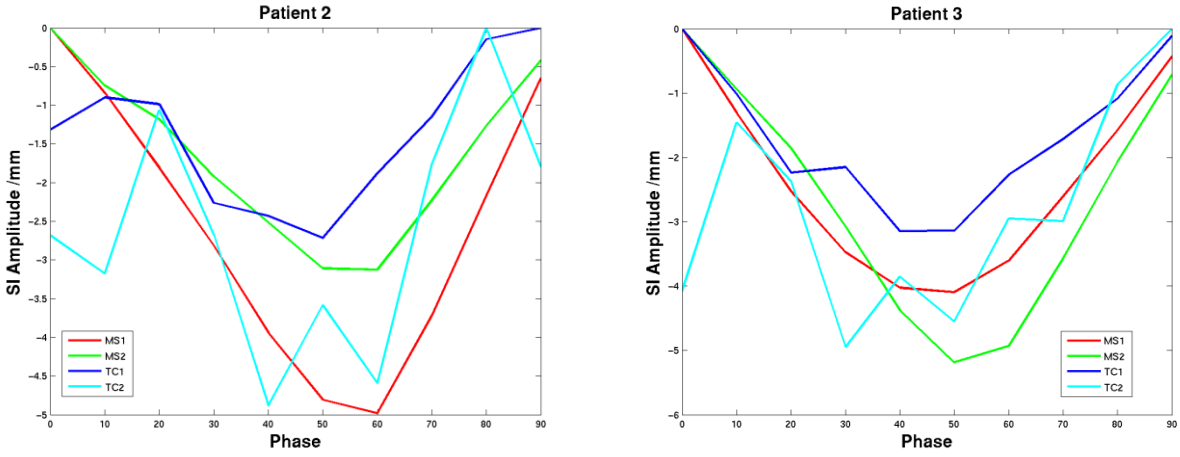

Figure 3. Tumor and marker trajectories for the first two weekly CBCT of Patient 2 and 3 at the SI direction. MS1 and TC1 are the marker and tumor trajectories respectively for week one, MS2 and TC2 for week two.

2.5. Conclusion

In the remaining of this thesis, TMD is computed from TMD_DIR for the framework formation. The validation framework is demonstrated to be an accurate approach to generate reference tumor trajectory for MLTM with an accuracy of 2.2/2.0/2.6 mm at LR/AP/SI directions.

3. MLTM in the Context of Minimal Target Deformation

3.1. Introduction

The validation framework set up in Chapter 2 is used to guide the development of MLTM. The next major aim of this dissertation is to implement and improve MLTM for tumors with minimal shape or volume change. The more difficult task of adapting MLTM accounting for shape and volume change is deferred to the following chapter. Appendix II describes the major analyses and conclusions. The current chapter provides the supplementary information in the development of the algorithm design. The major contributions of this chapter are to extend an existing MLTM in the following ways. Firstly, projection images are preprocessed to obtain higher quality projections. The main goal is to improve soft tissue contrast (the tumor visibility). Secondly, a study is conducted to investigate the shape and the appearance of the tumor template, which is the key component in the template matching process. The creation of tumor templates may introduce artifacts or artificial boundaries that could cause errors in the template matching process. In the following, more results, which lead to the selection of the template type, will be discussed. Finally, a prediction method is introduced to constrain the searching region for template matching in order to obtain more precise matching results. The advantages and limitations of this method will be discussed.

(a)

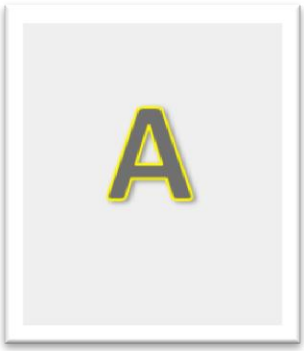

(b)

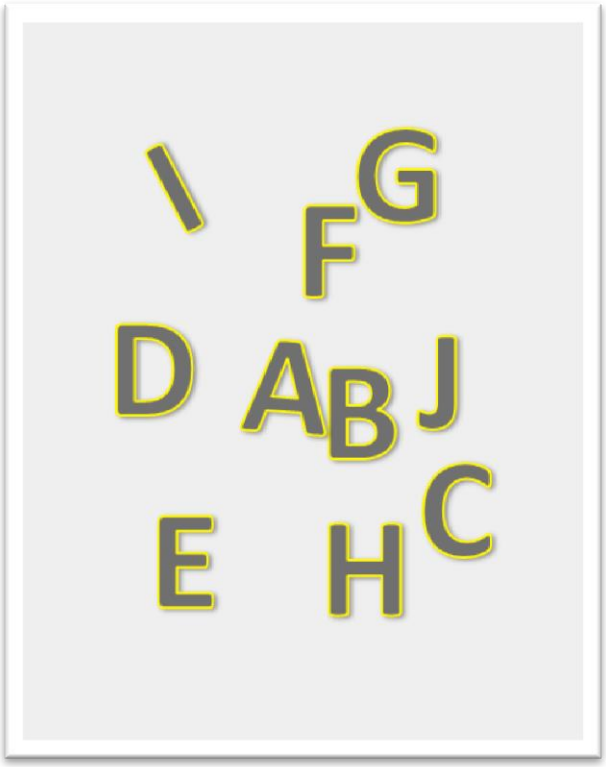

Figure 4. An example of template and search image.

3.2. The Principles of MLTM

3.2.1. Overview of Template Matching

Template matching[113,114] is a technique used to classify objects in an image by matching a set of templates to the image. If an image contains an unknown object, a set of templates with known objects are matching to the image to find out the best match which determines what the object is. Template matching is also position sensitive, meaning that it can also be used to register images. In this chapter, template matching is implemented to estimate the position of an object in an image.

In order to identify an object A in a search image $\mathbf{S}(x, y)$ as listed in Figure 4 (b), where (x, y) represent the horizontal and vertical coordinates of each pixel, a template image $\mathbf{T}(u, v)$ of the object shown in Figure 4 (a), where (u, v) represent the horizontal and vertical coordinates of each pixel in the template image, is made from a part of the search image

or a different image which contains the shape and intensity information of the object. When conducting template matching, the template $\mathbf{T}(\mathrm{u},\mathrm{v})$ moves over the whole search image and the similarity score at each pixel position (x, y) of the search image is calculated. The position with the highest score is considered as the best match. One commonly used similarity measure is the sum of squared differences (SSD) of the intensity between the two images. The intensity of pixel (x, y) in the search image is defined as $I_s(x, y)$ and the intensity of pixel (u,v) in the template image as $I_t(\mathrm{u},\mathrm{v})$. The SSD is calculated at each pixel (x, y) in the search image as listed below:

$$SSD(x,y) = \sum_{i=0}^{T_{cols}} \sum_{j=0}^{T_{rows}} \left(I_s(x+i, y+j) - I_t(i,j) \right)^2 \tag{5}$$

where T_{rows} and T_{cols} denote the number of rows and columns of the template images. This method to compute the similarity is computationally expensive, so more efficient ways to compute the coefficients are needed. The calculation in Equation (**5**) can be expanded as

$$SSD(x,y) = \sum_{i=0}^{T_{cols}} \sum_{j=0}^{T_{rows}} I_s(x+i, y+j)^2 + I_t(i,j)^2 - 2I_s(x+i, y+j) I_t(i,j) \tag{6}$$

where the terms $\sum_{i=0}^{T_{cols}} \sum_{j=0}^{T_{rows}} I_s(x+i, y+j)^2 + I_t(i,j)^2$ could be considered to be constant across all possible matches (i,j) and the remaining term $-2I_s(x+i, y+j) I_t(i,j)$ is depends on the 2D shift (I,j). Hence, cross correlation coefficient (CC) defined in the following equation is utilized to simplify the calculation of SSD. The expression of CC is similar to convolution as shown below:

$$\mathrm{CC}(x,y) = \sum_{i=0}^{T_{cols}} \sum_{j=0}^{T_{rows}} I_s(x+i, y+j) I_t(i,j) \tag{7}$$

Thus, convolution, which is calculated by Fast Fourier Transform (FFT), was implemented in the computation of CC to improve computation efficiency. Given F_s as the FFT of I_s, F_t as the FFT of I_t, and $IFFT()$ as the Inverse Fast Fourier Transform function, the correlation matching surface is:

$$\Re\left\{IFFT(F_s G_t^*)\right\} \tag{8}$$

In practice, the normalized version of the cross correlation, noted as normalized cross correlation (NCC) is used to eliminate effects caused by different illumination situations of the images.

$$\mathrm{NCC}(x,y) = \frac{\sum_{i=0}^{T_{cols}}\sum_{j=0}^{T_{rows}}(I_s(x+i,y+j)-\overline{I_s})(I_t(i,j)-\overline{I_t})}{\sqrt{\sum_{i=0}^{T_{cols}}\sum_{j=0}^{T_{rows}}(I_s(x+i,y+j)-\overline{I_s})^2(I_t(i,j)-\overline{I_t})^2}} \tag{9}$$

where $\overline{I_s}$ and $\overline{I_t}$ are the mean intensity of the search image and the template image respectively. NCC is not robust if there are occlusions in the search image, which are extraneous features and overlying tissues (bones, tables, and etc.). To overcome this deficiency, a more robust approach noted as Orientation Correlation (OC)[115] was implemented in this thesis. OC is the CC calculated on orientation images (orientation of intensity gradient) instead of the original intensity images. The orientation image f of an image with intensity I is calculated by:

$$f(x,y) = \mathrm{sgn}\left(\frac{\partial I(x,y)}{\partial x} + i\frac{\partial I(x,y)}{\partial y}\right) \tag{10}$$

where i is the complex imaginary unit and $\mathrm{sgn}(x) = \begin{cases} 0 & \text{if } |x| = 0 \\ \dfrac{x}{|x|} & \text{otherwise} \end{cases}$

f_s and f_t are calculated for intensity images of the search image I_s and the template I_t correspondingly. And the OC of the template and the search image is the CC of f_s and f_t. Orientation correlation matches the orientation of the gradient for each pixel and thus it is insensitive to high density noise and occlusions. This advantage is important for this work because the target images, CBCT projections, have high noise levels and the matching of tumor are influenced by occlusions such as bones, treatment table, cables and etc.

3.2.2. Workflow of MLTM Tumor Detection

Template matching has been employed to extract tumor trajectories or breathing signals in fluoroscopic images of RT[83,86,116,117]. Reference templates which correspond to different breathing phases and tumor positions are generated from either 4DCT or fluoroscopy images taken at the simulation stage (refer to Appendix II for more detail). The tumor position or the breathing phase of a search image is obtained by matching the template to the search image. The full tumor trajectory or breathing signal is generated by running the template matching at a set of sequential images of a time period.

In this thesis, the author implements template matching in tumor trajectory estimation at CBCT projections instead of fluoroscopic images. The latter are acquired at a fixed gantry angle, usually the AP view, in fluoroscopy, while the CBCT projections are rotated over 360 degrees or 200 degrees. The rotational geometry of CBCT makes it more challenging to implement the technique. First of all, more templates need to be generated to cover the different geometry due to gantry rotation. Secondly, contrast and motion enhancement techniques cannot be applied the structure of interest due to the changing geometry for the rotating images. Furthermore, the

variations in tumor visibility at different gantry angles also complicate the template matching. The purpose of this work is to achieve clinically-acceptable tracking accuracy of lung cancers using template matching-based algorithm in CBCT projections.

The basic framework of MLTM was developed previously by Hugo et al. for small, well-define and radiosurgery eligible tumors [98]. Briefly, the procedure consists of five steps as shown in Figure 5: 1) Gross tumor volume (GTV) (in green) was delineated at each phase of the planning 4DCT by physicians and it was expanded with a margin to obtain the expanded GTV (Ex-GTV, in purple). Note that the Ex-GTV was not equivalent to the clinical target volume used to plan for microscopic disease, but instead was used exclusively for template generation. 2) A masked CT was generated by zero padding regions outside the Ex-GTV of each phase of the 4D scan, and the masked CT was shifted to the daily tumor position by registering the planning CT and the daily free breathing reconstructed CBCT to the tumor. 3) The shifted masked CT was forward projected onto the virtual detector plane to generate digitally-reconstructed radiographs (DRR) at all breathing phases and at periodically-spaced gantry angles, which are termed the tumor templates (TT). 4) The TT was cropped and 2D/2D registration of TT to the measured projection (MP) was performed by template matching (TM) within a search region. The 2D tumor position in each MP of the free breathing CBCT was calculated by matching the MP with its corresponding TT. The 2D registration searched in a window of ±4 mm around the 2D tumor position at the detector plane (equivalent to ±2.7 mm at the room coordinate system) to find the best match of the TT and the MP. The red contour in Figure 1 showed a matching result. 5) The 2D tumor positions are reconstructed to the 3D tumor trajectory by backprojection. The masked CT was shifted to the daily tumor position in step 2) because the difference between the real

daily tumor position and the tumor position of the masked CT should be small enough in order to obtain correct tumor template in step 3) and use small template searching windows in step 4). The angle between an object and the radiation source as well as the length of tissue travelled by radiation beams are different if the position of the object is different. The shape and the intensity of the tumor in the template are related to the radiated angle and the beam travel length. If the tumor position the masked CT is far away from the real daily tumor position, the shape and intensity of the tumor template would be incorrect. The masked CT is shifted to be closer to the real daily tumor position to obtain more accurate tumor template. Furthermore, if the tumor position in the tumor template is closer to the daily tumor position, the searching window in step 4) could be smaller so that the matching results are more refined and the computation is faster.

The following simple enhancements were added to this basic framework, but are not the main focus of the aim:

1) Histogram equalization is applied to the search region in the projection images to improve the contrast.
2) The search window for template matching is adapted to ±22.5 mm, which is ±15 mm in the room coordinates, instead of the ±4 mm window to account for the up to 3 cm tumor motion.
3) The similarity metric used to conduct template matching is changed from block NCC to orientation correlation.
4) A spatial probabilistic method developed by Poulsen *et al* [118] is used to reconstruct 3D tumor positions from 2D tumor positions than using simple backprojection technique in the original framework.

The main adaptions will be introduced in the following sections.

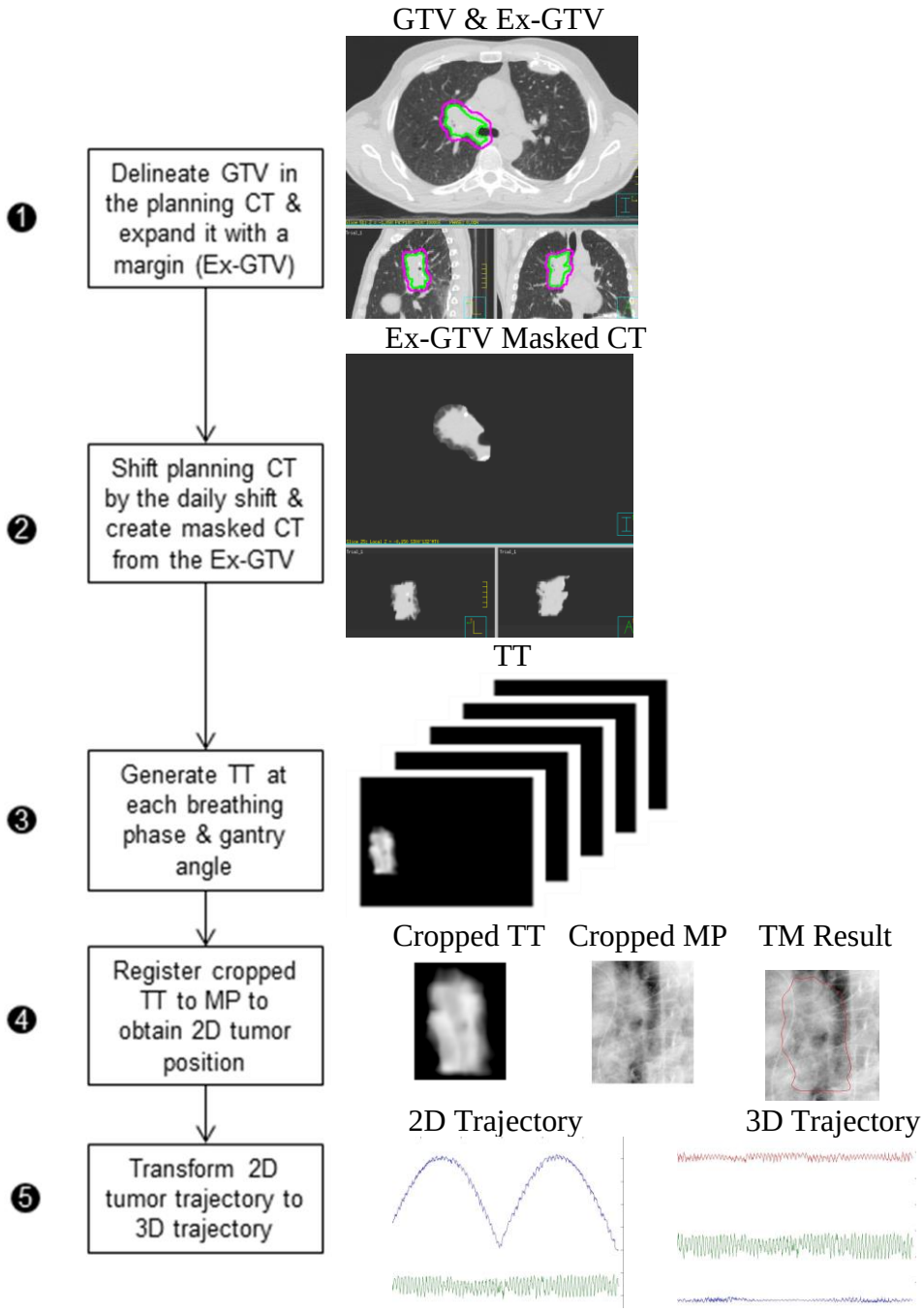

Figure 5. Workflow of MLTM in CBCT projections.

3.3. Software Development

The central code of the MLTM is a MATLAB-based code, denoted as Tumor Detect, which outputs the tumor 3d positions of CBCT projection images. The inputs of the algorithm are a set of templates, tumor position in each template, gantry angle and phase of each projection. The previous method for generating these inputs was mainly based on using the treatment planning system Pinnacle, which has many manual steps and was time-consuming. Automatic method needs to be developed in order to improve the efficiency and reduce manual errors. An in-house data read/write and automated data processing computing framework called RCF library is available to serve these purpose at generation of inputs for the Tumor Detect code.

TT is generated from each phase of the tumor-only CT by forward projection using an already-existing in house GPU-based algorithm called 'project'. The project code simulates the generation of a projection image. The pixel intensity in a simulated projection represents the integration of the attenuation along the ray path. The simulated projections can be generated at any gantry angle. The isocenter of the rotation is an input parameter which is specified by the user. For the same structure with different positions relative to rotation isocenter of the project code, the projections of the structure in the projection image are different due to divergence. In order to make the TT image as similar to the measured projection, the tumor position relative to the isocenter of the rotation in the masked CT should be roughly the same as the tumor position relative to the isocenter in the measured CBCT. So the isocenter of rotation for the project code should be at the isocenter of the reconstructed CBCT when the planning CT and reconstructed CBCT are registered to the tumor as shown below:

$$ISO_{cor} = ISO_{CBCT} + T \tag{11}$$

where T is the translation from registering the planning CT to the CBCT (using a region of interest containing only the tumor), ISO_{cor} is the center of rotation of the project code and ISO_{CBCT} is the isocenter of the CBCT. The tumor centroid position in the Tumor Template with this setting of rotation isocenter is at the tumor position of the daily CBCT, which means that the searching window of the 2D image registration from the Tumor Template to the projections can be constrained to a small region.

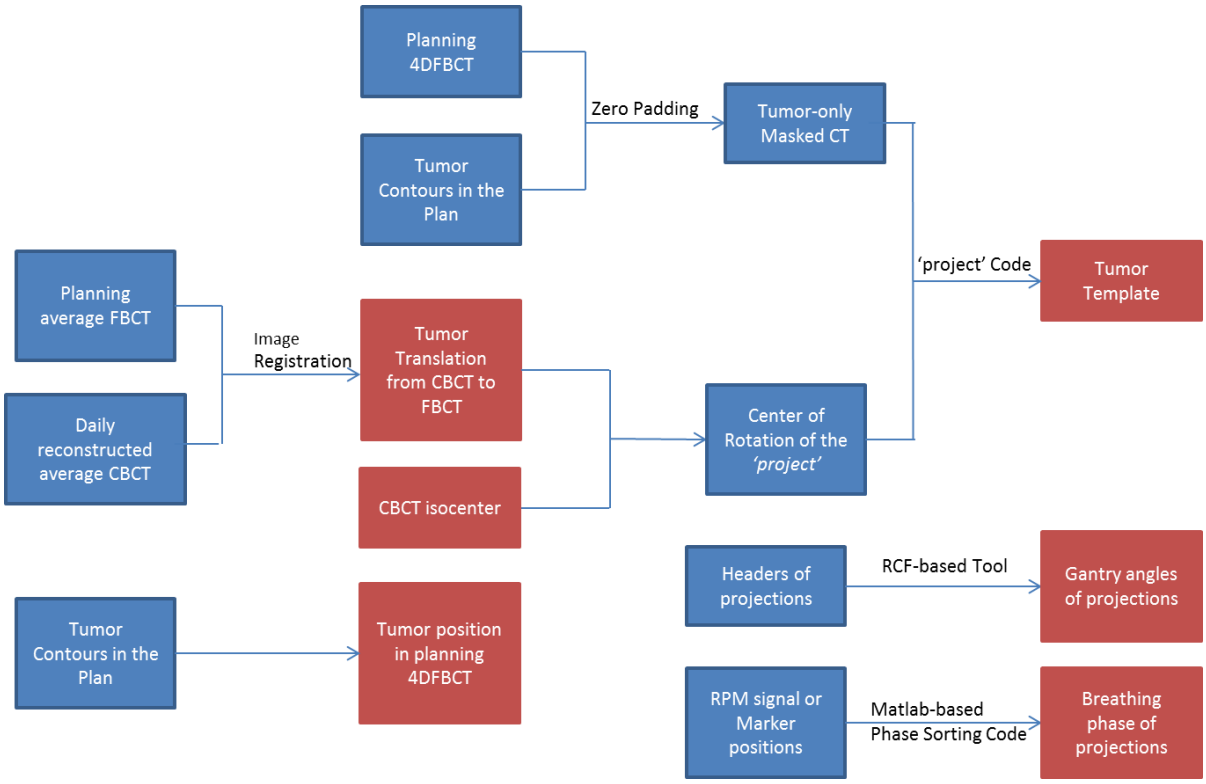

Figure 6 Flow Chart of generation of the input data for Tumor Detect algorithm. The red boxes are the input data for the Tumor Detect algorithm.

The required input data of the Tumor Detect algorithm are Tumor Templates, tumor positions of 4D FBCT, CBCT isocenter (Iso_{CBCT}), translation from the CBCT to the planning CT (T), the gantry angle and phase of each projection.

Figure 6 shows the flow chart of the generation of each of the four required pieces of input data for the Tumor Detect algorithm. The blue boxes in the figure contain the data required at each step for the generation of the input data in the red box. The summation of the computation process is shown in Table 5. The type of work and the approximate cost of time are listed for each step. Steps 1 to 3 are conducted once per patient. Other steps are conducted once per CBCT scan. The Pinnacle-based approach switches from several platforms leading to low efficiency and higher chances of calculation errors.

The RCF platform has direct access to the patient database which includes the planning CT, reconstructed CBCTs, treatment plans and contours. Hence, it doesn't need a copy of the data in as the Pinnacle-based approach. The RCF tool also has image processing package which include automatic image registration, generation of bitmap images, calculate centroid for an ROI and other functions that are required in our purpose. The process of the input data generation as listed in Table 6 is adapted to almost fully automatic which significantly improves the efficiency of the input preparation process.

Table 5. The cost of time for each step in Pinnacle-based process. If the property of a step is manual work, it only has manual cost and does not have automatic cost. Step 1-3 are done once for each patient, so the cost of time should be considered separately. The automatic cost is mostly the running of 'project' code, which depends on the capacity of the GPU-based server.

Steps		Properties	Manual cost	Automatic cost
1	Import planning CT image and plan with tumor contours into Pinnacle database	Manual work in Pinnacle	5 hours / patient	--
2	Calculate the center of mass of tumor for all the phases	Manual work in Pinnacle		
3	Expend GTV with a uniform margin and create new ROI for the expended GTV	Manual work in Pinnacle		
4	Load the reconstructed daily CBCT into Pinnacle database	Manual work in Pinnacle	20 minutes	--
5	Conduct rigid registration of the daily reconstructed CBCT and the planning CT by aligning the tumor	Manual work in Pinnacle	1 hour	--
6	Generate tumor-only masked CT	Matlab-based	20 minutes	10 minutes

		code		
7	Calculate the isocenter of the daily CBCT	Manual work	1 hour	--
8	Calculate isocenter of the rotation and generate Cliff files for the project code	Manual work		--
9	Generate templates from the 'project' code	Automatic Project code	--	5 hours
10	Obtain phase information for each projection	Matlab-based code	20 minutes	--
11	Obtain gantry angles of projections	RCF-based code		
Total Time cost per CBCT scan			3 hours /scan + 5 hours /patient	5.17 hours /scan

Table 6. The cost of time for each step in RCF-based process.

Steps		Properties	Manual cost	Automatic cost
1	Use a program to generate the of the input Cliff file for the RCF-based tool	Automatic	20 minutes /patient	Negligible
2	Download the image and plan information from the PPG website	Web download	--	10 minutes for all the patients
3	RCF-based too to do the processes 1~8,10 and 11 in Table 5	RCF-based tool	--	10 min
4	Generate templates from the 'project' code	Automatic Project code	--	5 hours
Total Time cost per CBCT scan			0.3 hours /scan	5.18 hours /scan

3.4. Refinement of MLTM Algorithm

3.4.1. Image Processing in Projection Images

The raw projections are preprocessed before any further analysis, such as dark-flood field correction, bowtie filter correction, dead pixel correction and noise filtering. Even with this preprocessing techniques, the image contrast of the projection images are limited especially in the slow gantry CBCT in which the radiation exposure/projection is less than the normal CBCT scans. Hence, contrast enhancement in the images for better tumor visualization is performed. The technique implement here is histogram equilibrium which enhances the image contrast by transforming the image intensities so that the histogram of the output image matches a specified histogram (uniform distribution here). The preprocessing process also includes the removal of

markers in the projections to eliminate the potential bias of the markers on the template matching. As described in Appendix II, markers are successfully removed from the projections by the marker painting technique.

3.4.2. Templates for Template Matching

Shape and appearance of tumor templates are investigated to preserve the real tumor boundary while minimizing introduction of artificial boundaries that may be introduced the zero padding in the generation of masked CT outside the Ex-GTV region in the planning CT. Three types of templates, including Ex-GTV template[98], a cylinder template[96], and a new padded template developed here were studied in Appendix II. All templates are created from the extended GTV which is GTV plus a 5 or 10 mm expansion. It is particularly important to conduct this study for locally-advanced lung cancers other than small, well-defined and radiosurgery eligible tumor cases. When creating DRR for tumor templates, artificial radiation beams penetrate the tumor. Large tumors attenuate the beams more than the small tumor causing large differences between zero and nonzero paddings. Therefore, these three types of templates are investigated to reduce the zero padding effect. This effect can be mitigated to include more lung tissues by increasing extended GTV expansion from 5 mm to 10 mm. However, for tumors with large volume, the increased expansion itself introduces more noise structures in the templates. Thus, in this dissertation, a10 mm expansion is chose for patient 2 and 3 with smaller tumors (less than 50 cc) located in the central lung. For the remaining patients, the 5 mm expansion was used due to large tumor volume or diffuse tumor.

Tracking results using the three types of templates are compared to the reference trajectory generated from the validation framework in Chapter 2. The absolute difference

between the MLTM and the reference trajectory is defined as the error. Template matching with padded template provides the best results with an error of 3.5 mm, which is smaller than the 5.3 mm for Ex-GTV template and 6.1 mm for cylinder template. Similar as the numbers, in Figure 8 to Figure 12, the mismatch of the template matching with the marker reference is most severe with Ex-GTV template and the template matching with padded template best matches the marker reference.

3.4.3. Search Region of Template Matching

Even with the use of padded template, there are still large errors left in MLTM. The search window in the projection imager plane is fairly large, ±2.25 cm, accounting for a potential large motion of 3 cm (such as a deep breath). Hence, a way to narrow down the search window effectively is of interest. One possible approach is to refine the template matching search window with the velocity of tumor movement. The velocity may be up to 4 cm/s and with the 5 Hz frequency for projection scanning, the tumor movement between two neighboring projections is up to 8 mm at the global coordinate leading to a ±12 mm search window to the tumor position in the previous projection. This search window is still fairly large and the errors will propagate from one projection to the other. Hence, this approach is not pursued. A constraint method is introduced in Appendix II and is summarized in the following. Because the intended application of the MLTM algorithm is not for real-time applications but for retrospective review, the tumor trajectory obtained from a first pass of the MLTM algorithm can be considered as the training data to generate an average cycle (mean tumor position of each breathing phase), which is used as the guidance for a second pass of the template matching. A narrower search window is placed

at the phase mean tumor position, so that the chance of getting true template matching position increases.

The size of the restricted search window is estimated from analyzing of marker trajectories segmented from projections. For a marker in a CBCT scan, trajectory $\mathbf{M}$ is segmented in projections $\mathbf{P}$. Let $\vec{m}_p$, $\vec{m}_p \in \mathbf{M}$ to be the marker coordinates of a single projection p, $p \in \mathbf{P}$. $\mathbf{P}$ is grouped into 10 phases bins based on the SI marker positions, phase i projection group denoted as $\mathbf{P}^i$. For projection group at phase i, the mean marker position M^i is calculated. For a projection p, $p \in \mathbf{P}$, a phase j is determined from the in-house phase sorting algorithm. The difference ε_p between the instantaneous marker position m_p and the phase j mean marker position M^j is calculated:

$$\varepsilon_p = m_p - M^j \tag{12}$$

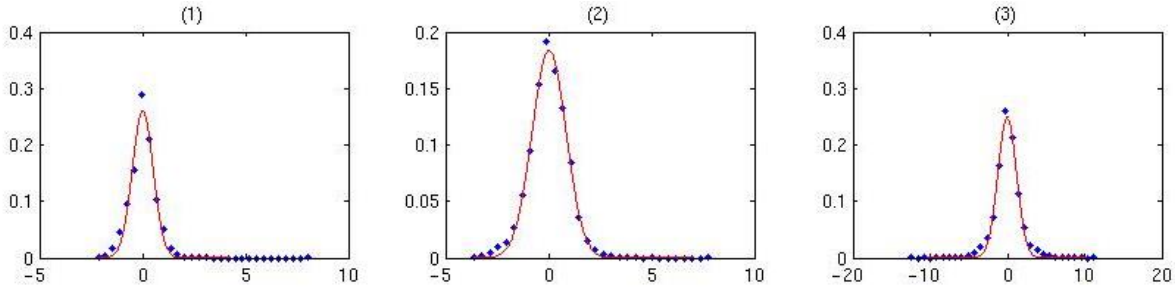

Figure 7. Probability density functions (PDF) of $\mathbf{E}$ (blue dots) and their fitted Gaussian curves (red curve). Plots (1), (2) and (3) are at LR, AP, and SI directions respectively. $\mathbf{E}$ are calculated for all the available marker trajectories, about 6 trajectories per patient.

The differences $\mathbf{E} = \left\{ \left\{ \varepsilon_p, p \in \mathbf{P} \right\}_1, \left\{ \varepsilon_p, p \in \mathbf{P} \right\}_2, \cdots \left\{ \varepsilon_p, p \in \mathbf{P} \right\}_S \right\}$, where S is the total number of marker trajectories. The standard deviation of $\varepsilon, \varepsilon \in \mathbf{E}$ and the interval included 97% of ε in $\mathbf{E}$ are computed. The distribution of ε is close to Gaussian distribution as shown in Figure 7.

The standard deviations, σ are 0.6/0.9/1.7 mm in the LR/AP/SI directions, respectively, and the 97% interval is $\pm 1.4/\pm 2.1/\pm 4.0$ mm. The search windows decided by either the 2.5σ (1.5/2.25/4.25) or the 97% interval are close to each other. Therefore, the search window of ± 3 mm at the *u* (across the imager panel) and ± 6 mm at the *v* direction (along the imager panel) is applied to the phase mean tumor position in Appendix II. As shown in Figure 8 to Figure 12, the constraint method eliminates large jumping errors and improves the match between the results of MLTM and the reference compared to the non-constraint methods.

3.5. Conclusion

The effect of the artificial boundary created by zero padding in the generation of masked CT is reduced by padded template which is selected as the tumor template for further study. The constraint method is able to reduce the search window in the template matching and improve the matching results.

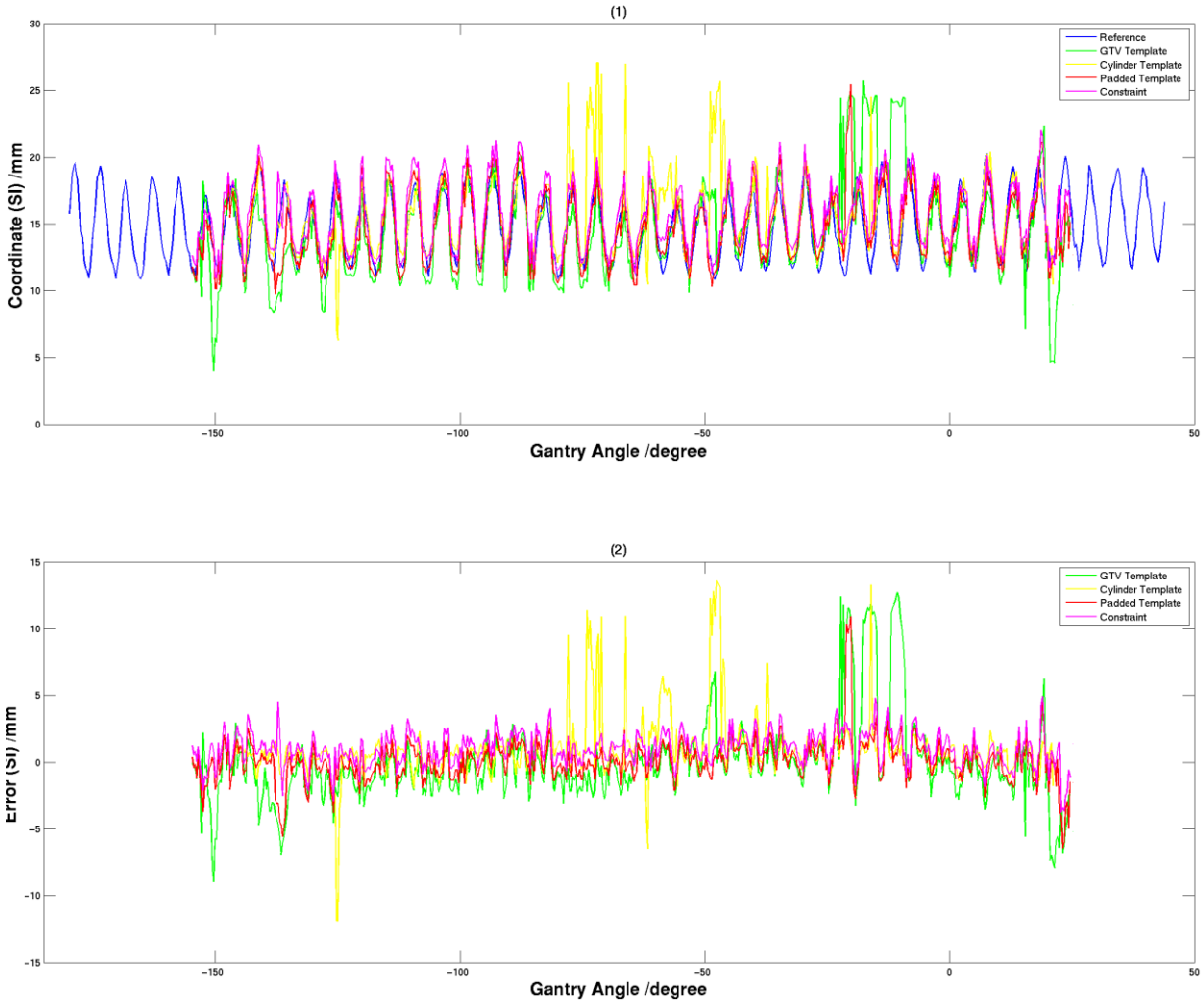

Figure 8. Patient 1 first fraction CBCT. (1) Breathing curves comparison at SI direction (2) Error comparison at SI direction.

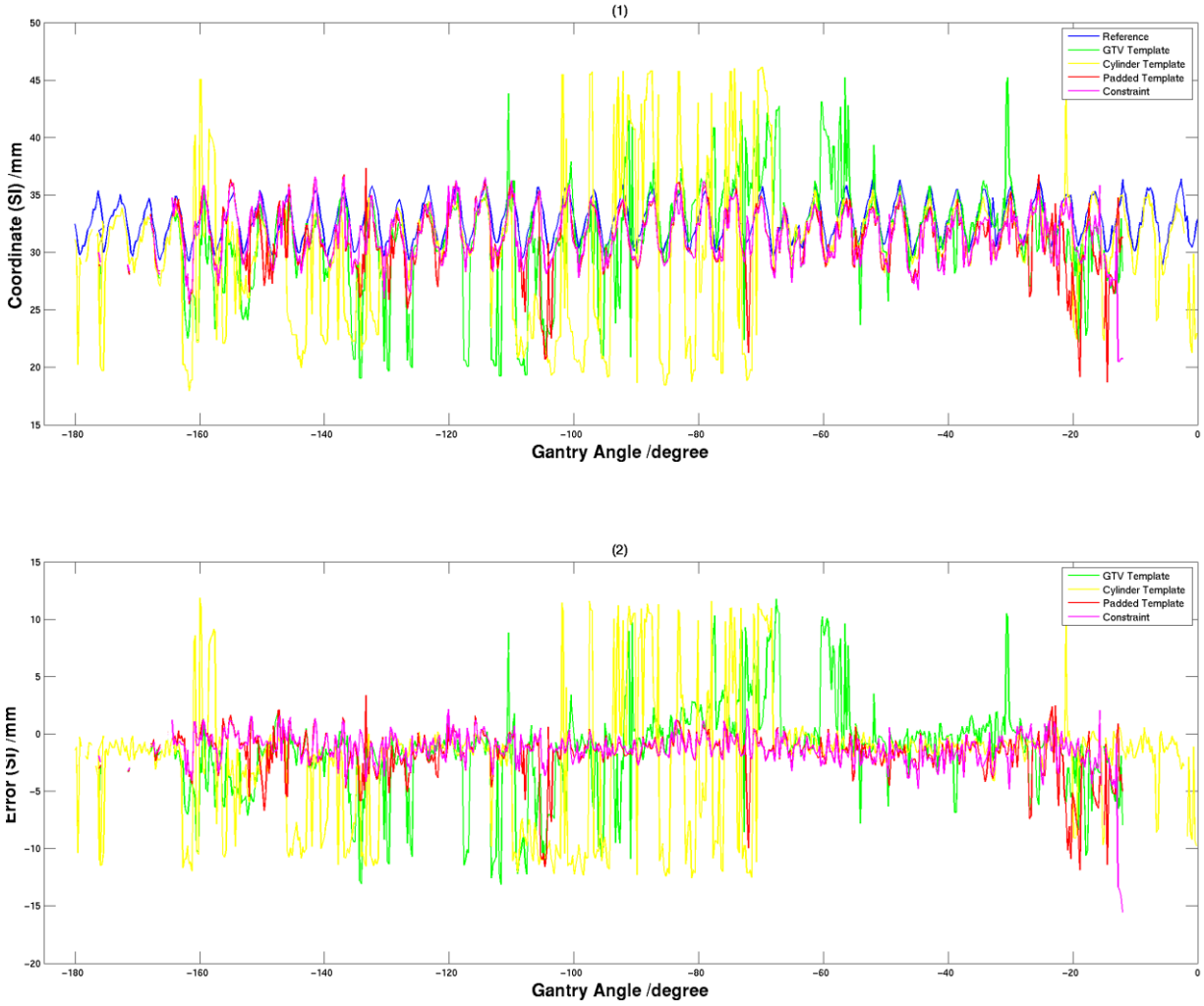

Figure 9. Patient 2 first fraction CBCT. (1) Breathing curves comparison at SI direction (2) Error comparison at SI direction.

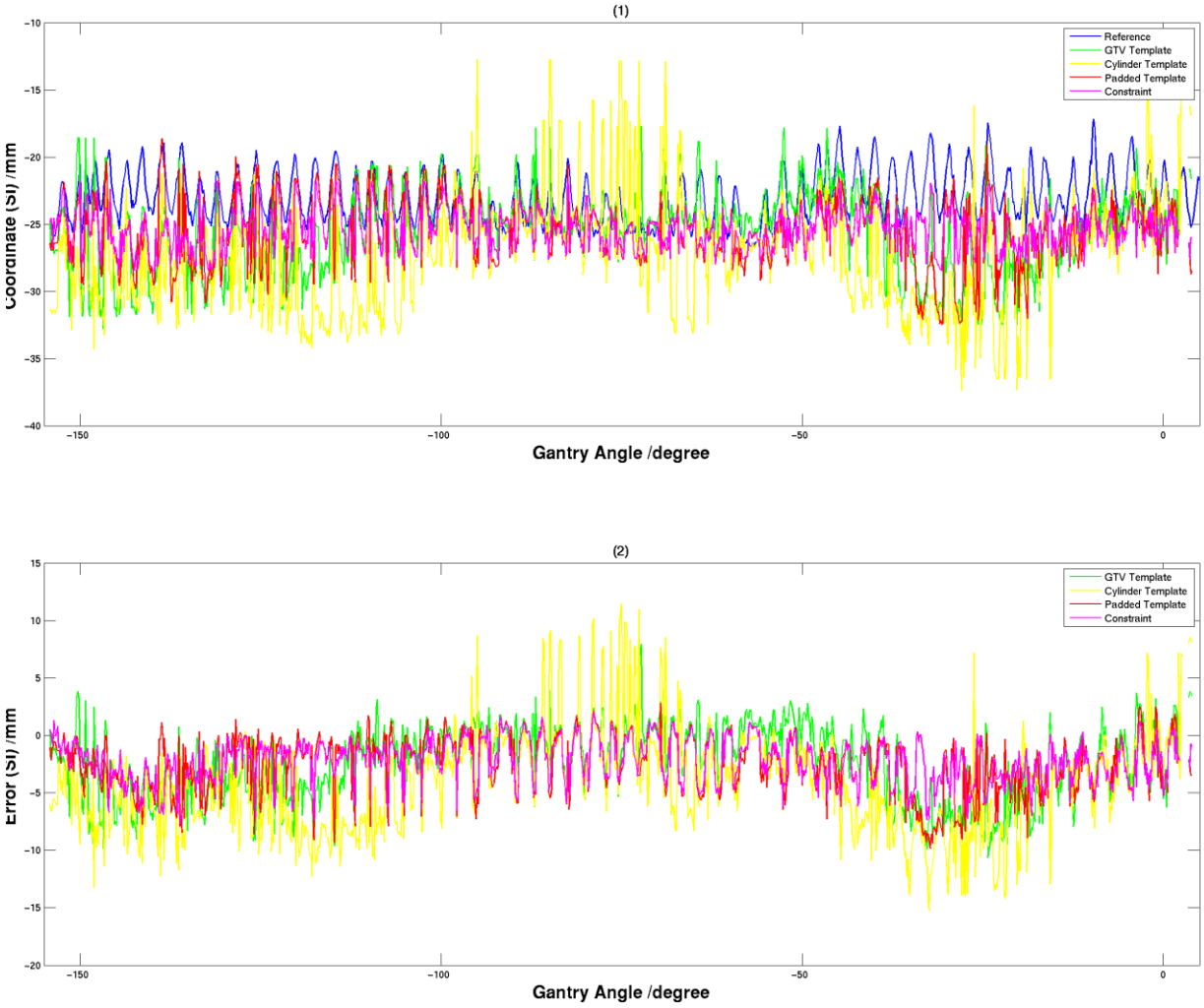

Figure 10. Patient 3 first fraction CBCT. (1) Breathing curves comparison at SI direction (2) Error comparison at SI direction.

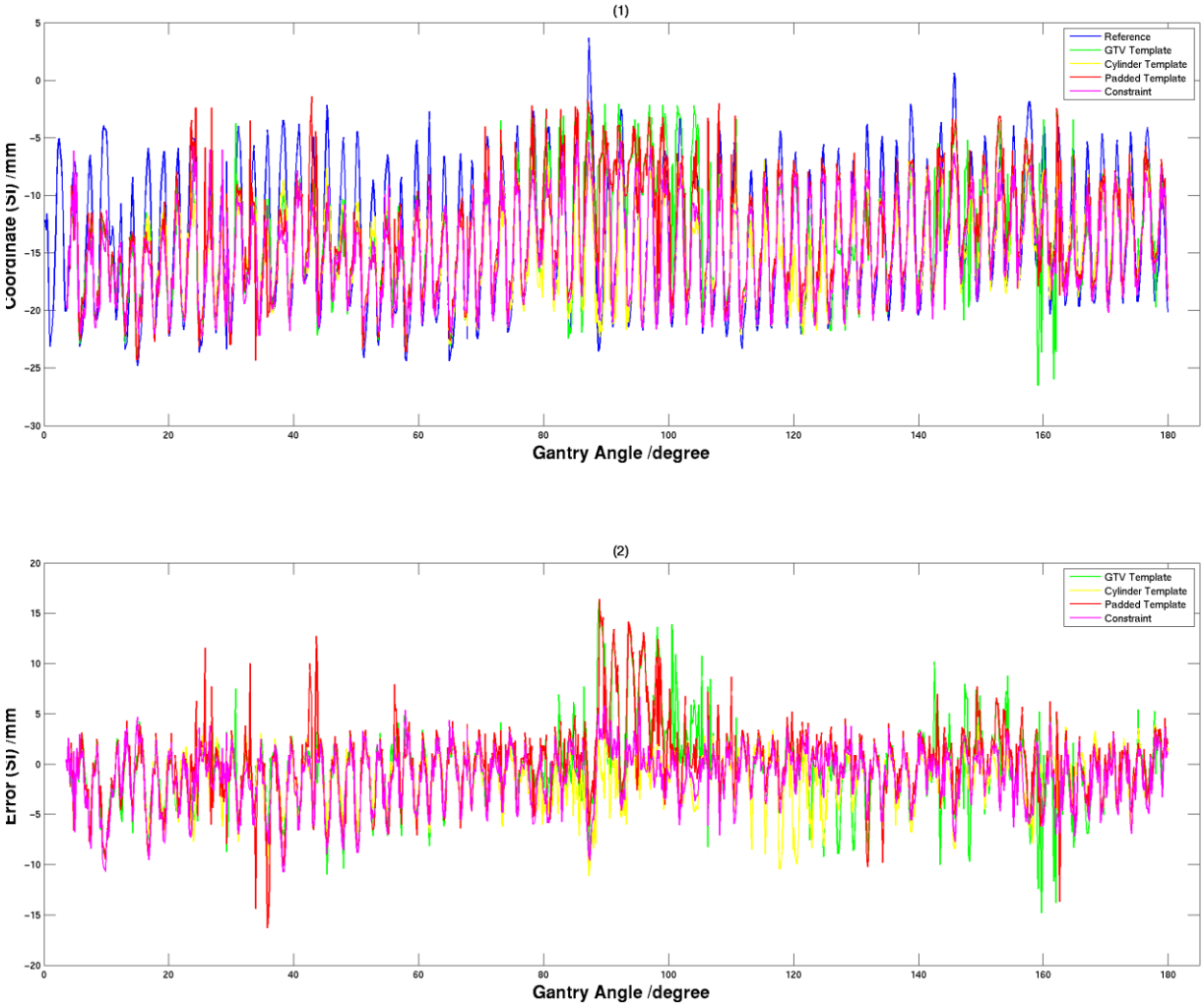

Figure 11. Patient 4 first fraction CBCT. (1) Breathing curves comparison at SI direction (2) Error comparison at SI direction.

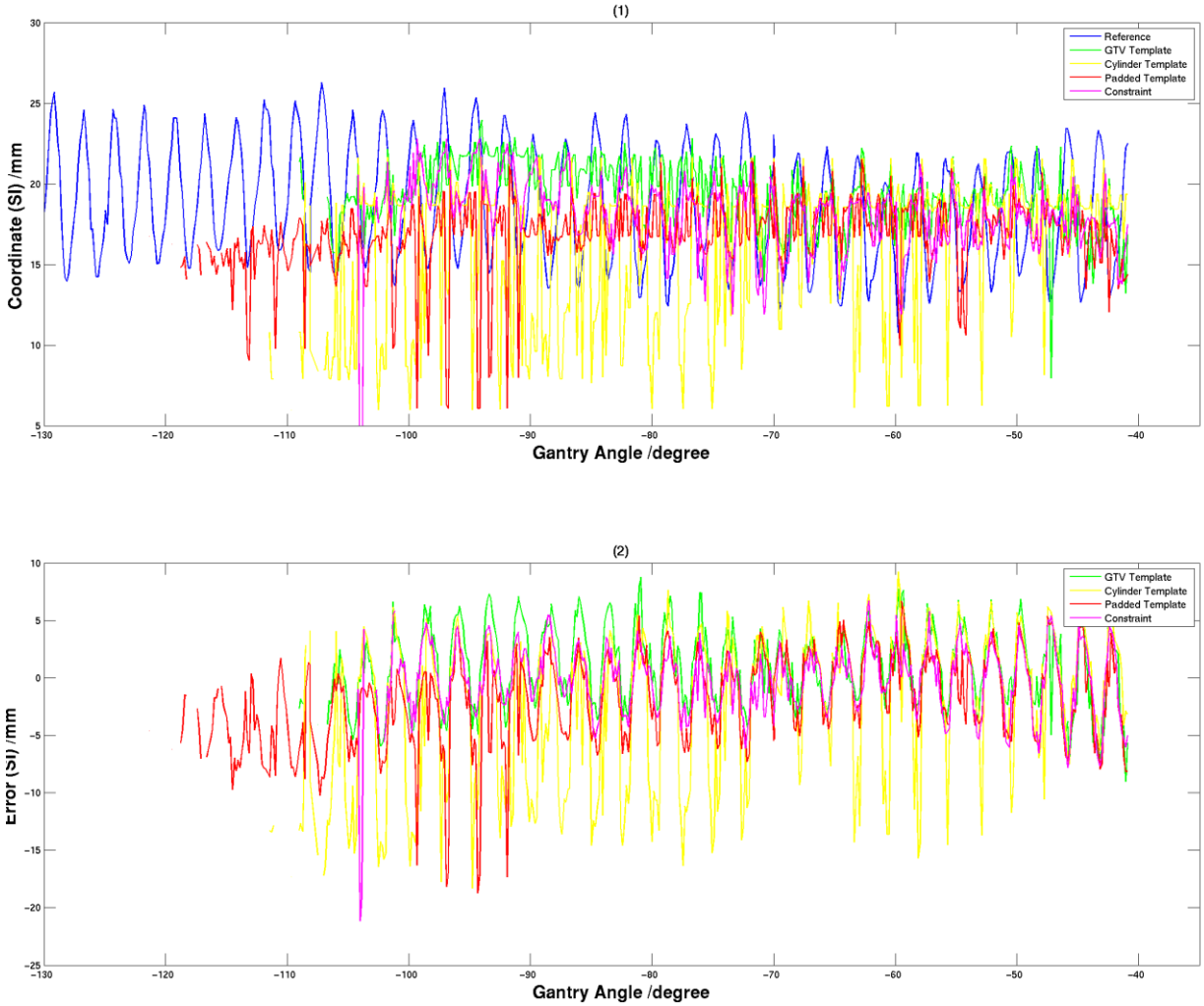

Figure 12. Patient 5 first fraction CBCT. (1) Breathing curves comparison at SI direction (2) Error comparison at SI direction.

4. MLTM Considering Target Deformation

4.1. Introduction

In the previous chapter, the MLTM algorithm considers tumors with minimal shape or volume change. Patients studied by this dissertation underwent treatments last up to 7 weeks, so there is a high chance that tumor will deform due to natural growth of the tumor or treatment response. Shape and volume of a tumor at the treatment day vary from the planning tumor, especially near the end of the treatment course. Compared to the pretreatment tumor volume on planning CT, tumors regressed 30% to 65% at the end of the treatment for patients involved in this dissertation. If shape and volume of a tumor change too much at the treatment day compared the planning CT, the algorithm may fail. In previous chapter, templates are directly made from pre-treatment planning FBCT. The MLTM with those templates is not able to obtain correct results for fractions with large tumor deformation, because the tumor in the template differs too much from the daily tumor. Therefore, the next major aim of this dissertation is to adapt the MLTM algorithm for tumors with large shape or volume change.

The key issue for the adaptation of the template matching is how to generate a set of templates that represent the daily tumor shape. Rescanning and re-delineating the patient with FBCT is one option. But it is too costly, both in time and resources. The other option is to generate tumor templates from the delineated daily CBCT. However, the image quality of CBCT is low, and the tumor definition for the DRR generation requires high image quality. A

way to transform the planning tumor to the daily tumor is considered in this thesis to accommodate the need to obtain tumor templates with the daily tumor shape while maintaining the image quality. Different image registration methods are performed to register the planning CT to the daily CBCT by aligning tumor. In the following, how to deform the planning tumor and whether the target transformation is adequate for markerless tracking near the end of the treatment course will be investigated.

4.2. Transformation of Planning Target

In order to segment the tumor correctly in a MP by template matching, shape and size of the tumor on its corresponding TT should as similar as on MP. TT (2D) is generated from the masked CT (tumor-only CT, 3D) as mentioned in section 3.2.2. Hence, the problem is equivalent to that the tumor on the masked CT (masked tumor) should match the tumor on reconstructed daily CBCT (daily tumor). The proposed solution is to transform the tumor on the masked CT to match the daily tumor. The transformation is obtained by image registration between the planning CT and the daily CBCT. In Chapter 3, this transformation is rigid meaning no shape, size and intensity change of masked tumor compared to the planning tumor. Non-rigid or deformable transformation is needed to apply to the planning tumor to deal with shape and volume change. Both affine transformation and B-Spline DIR, which are introduced in section 2.3, are applied to register the planning CT and the daily CBCT to the tumor. The resulting transformations from the image registrations are applied to the masked CT, and the transformed masked CT is used to create TT for template matching. Affine transformation accounts for tumor expansion or shrinkage and DIR transforms the tumor in a more complex

way. The transformed tumors of the two approaches are examined visually to check whether the tumors align properly.

A study is conducted to determine which method is selected to deform the tumor by comparing the tracking results of transforming the masked CT with rigid image registration, affine transformation and B-Spline DIR. As described in Chapter 2, the average CT of the free breathing planning CT and average CBCT are registered and the resulting transformation is used to transform the phase images. The image quality of the CBCT phase images is poor and hence the average CBCT is used to obtain better registration results. The spacing of the grid for defining control points is 8.0, 4.0, 2.0, and 1.0 voxels. The DIR is running at multi-resolution with down-sampling and the resolution pyramid is 8.0, 4.0, 2.0, and 1.0 voxels. The rest of the MLTM algorithm uses the method selected in Chapter 3 (padded template + constraint method). The study is performed on the last weekly CBCT of each patient in which shape and volume of the target changes most. Table 7 shows that rigid registration is not adequate for fractions near the end of the treatment course. However, the affine transform does not improve the results as listed in Table 8. The trajectories of the MLTM using B-Spline DIR are shown in red curves in the bottom plots of figures from Figure 21 to Figure 25 (the blue curves are the reference trajectories). The accuracies are calculated in

Table 9. As suggested in the tables and the figures, B-Spline DIR improves the tracking results substantially and provides promising accuracy.

Table 7. Errors of MLTM when the masked CT is rigidly transformed.

Rigid	Absolute Error/mm			STDV/mm			90% Error Level/mm		
Patient	LR	AP	SI	LR	AP	SI	LR	AP	SI
1	1.0	5.5	2.8	1.4	7.7	3.9	2.2	12.8	4.7
2	3.8	6.7	4.1	6.0	10.3	6.2	12.0	21.0	14.0

3	7.4	1.7	5.2	1.8	1.6	4.9	9.6	3.7	9.2
4	1.6	2.0	1.8	2.5	0.9	2.5	4.2	3.3	4.0
5	3.3	4.7	4.6	1.3	2.3	5.3	4.9	7.3	10.8
Mean	4.1	4.6	3.9	3.1	5.9	4.7	7.5	11.7	9.3

Table 8. Errors of MLTM when the masked CT is transformed by affine transformation.

Affine	**Absolute Error/mm**			**STDV/mm**			**90% Error Level/mm**		
Patient	LR	AP	SI	LR	AP	SI	LR	AP	SI
1	0.9	5.3	2.5	1.2	7.8	4.4	1.8	12.3	6.4
2	2.8	5.7	3.3	4.8	9.3	4.8	8.0	15.0	7.7
3	4.4	4.0	4.7	1.6	3.4	5.2	5.8	6.8	8.7
4	4.6	1.4	2.1	2.5	0.9	2.5	6.6	2.5	4.1
5	6.6	10.7	7.5	1.5	13.1	8.5	8.9	21.8	16.3
Mean	4.3	6.2	4.5	2.7	8.1	5.4	6.7	13.4	9.6

Table 9. Errors of MLTM when the masked CT is transformed by B-Spline DIR.

B-Splines	**Absolute Error/mm**			**STDV/mm**			**90% Error Level/mm**		
Patient	LR	AP	SI	LR	AP	SI	LR	AP	SI
1	0.7	1.9	0.7	0.6	0.8	1.0	1.3	2.5	1.6
2	0.3	0.7	1.1	0.2	0.7	0.8	0.5	1.4	2.1
3	1.5	1.6	1.3	0.6	1.2	1.8	2.2	3.6	3.0
4	1.6	0.6	1.0	0.3	0.7	1.3	1.9	1.2	2.1
5	2.4	1.2	2.1	1.1	0.9	2.7	3.8	2.2	4.8
Mean	1.5	1.3	1.3	0.6	0.9	1.7	2.2	2.3	2.9

4.3. Conclusion

Affine transformation fails to provide an accurate target registration. Transforming masked CT by B-spline DIR results in best tracking results, 1.5/1.3/1.3 mm at LR/AP/SI directions. The transformed masked tumor matches well to the daily tumor in shape and volume therefore B-spline DIR should be conducted to the planning CT in the process of MLTM.

5. Result Analysis of MLTM

5.1. Introduction

The major goal of this thesis is to produce a method that is better than 4D CBCT in estimating tumor trajectory. The algorithm is developed in Chapters 3 and 4 along with Appendix II. How the algorithm performs and whether it outperforms 4D CBCT is a question yet to be answered. Hence, the next major aim of the thesis is to analyze to accuracy of the MLTM algorithm and compare against 4D CBCT. The major contribution of this chapter is to analyze the results of MLTM in the following ways. Firstly, the tracking errors of each scan of every patient are calculated and studied. Due to the rotation geometry of the CBCT projections, the tracking results are expected to be different at different gantry angles. The correlation of the tracking errors and gantry angle are studied to determine whether the errors correlate consistently among patients with the gantry angles. If there is a correlation, certain gantry angles with larger tracking errors can be avoid to be used in the creation tumor trajectory or pdf of tumor motion. Secondly, the markerless tracking algorithm is compared against the clinical standard 4D CBCT. The full trajectory of MLTM and the 4D CBCT are compared and the errors are calculated. In the following, angular correlation of tracking errors and whether MLTM outperforms 4D CBCT will be determined.

5.2. Angular Error Analysis

MLTM is performed on projection images which are planer image rotating with the rotation of the gantry. For the images evaluated here, the gantry rotated during CBCT acquisition from -180 ºto 180 º, or the opposite. Image at 0 ºis AP view, 180 º(or -180 º) is PA view, 90 ºis RL view and -90 ºis RL view. The errors are defined as the absolute difference between the MLTM trajectories and the reference trajectories obtained from Chapter 2. Figure 16 to Figure 20 plot the errors of the MLTM trajectories at the SI direction against gantry angles of the 5 patients. For statistical analysis, projections are grouped in 36 groups by gantry angles with an interval of 10 º. Projections with gantry angles from -180 ºto -170 ºbelong to group 1, where the mean gantry angle -175 ºis the gantry angle of the group, and projections with gantry angles from 170 º to 180 ºbelong to group 36, whose group gantry angle is 175 º. Analysis of variance (ANOVA) test is used to evaluate if there was any relationship between the mean errors of the 36 groups of projections with the gantry angles. Figure 13, Figure 14 and Figure 15 are the results of ANOVA test at LR, AP and SI directions. The p values of these 3 tests are all less than 0.0001. Therefore, there are significant difference between groups and the tracking errors are gantry angle dependent. As the gantry rotates, the contrast of tumor differs because the length of tissues or bones that the radiation beams penetrates are different at different gantry angles. The errors are generally worse at oblique angles such as -135 º, -115 º, -35 º, 25 º, 35 ºand 105 º. The number of outliers (outside the blue lines in figures from Figure 16 to Figure 20) for each group, which are errors lying outside region [-2, 2] mm, is greater at gantry angles from -150 ºto -110 º and -60 ºto -30 ºfor patients 1, 2, 3 as well as 5, especially patient 3, and from 10 ºto 40 º, 100 ºto 120 º, 140 ºto 150 ºfor patient 4. These results are consistent to the ANOVA results. These

oblique angles are between lateral and AP/PA views, where beams penetrate more bony structures (ribs) leading to worse results.

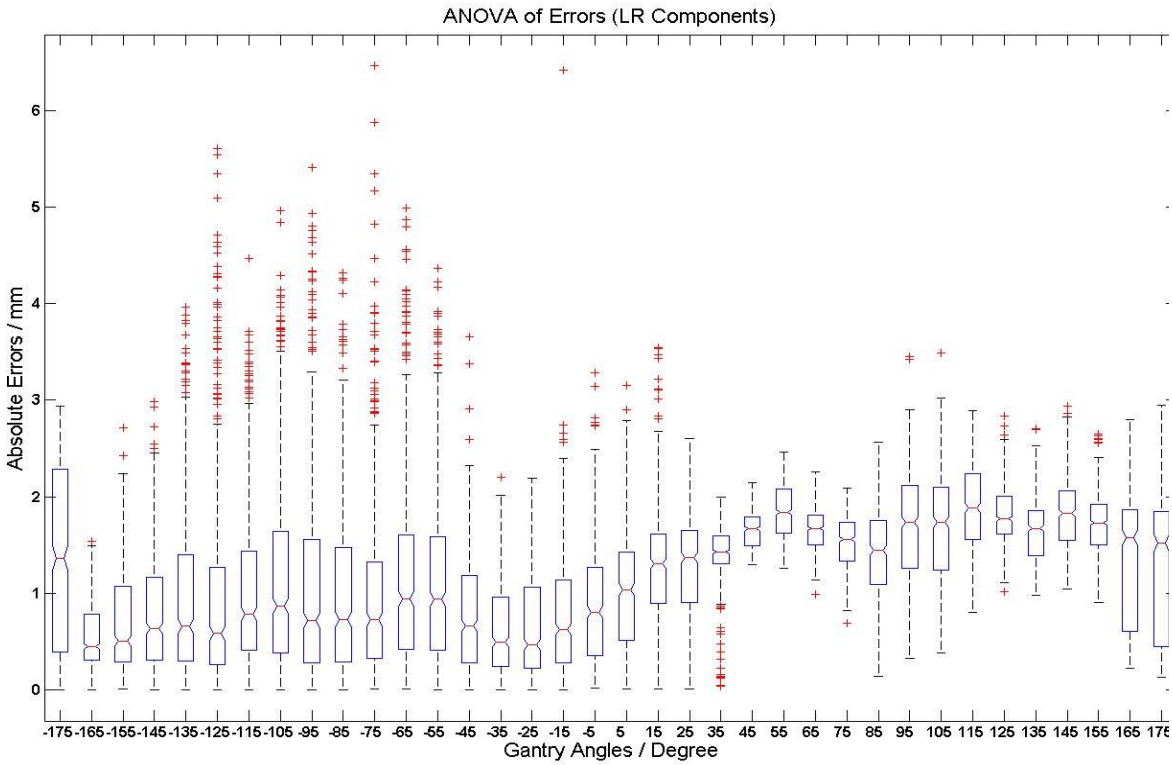

Figure 13. ANOVA test results for LR components of absolute errors with gantry angle grouping. For each group, the mean gantry angle is used to represent the group. The central of the box indicates the median value of the group and the lower and upper boundary line of the box are at the 25%/75% quantile of the data. The tick marks represent the outliers.

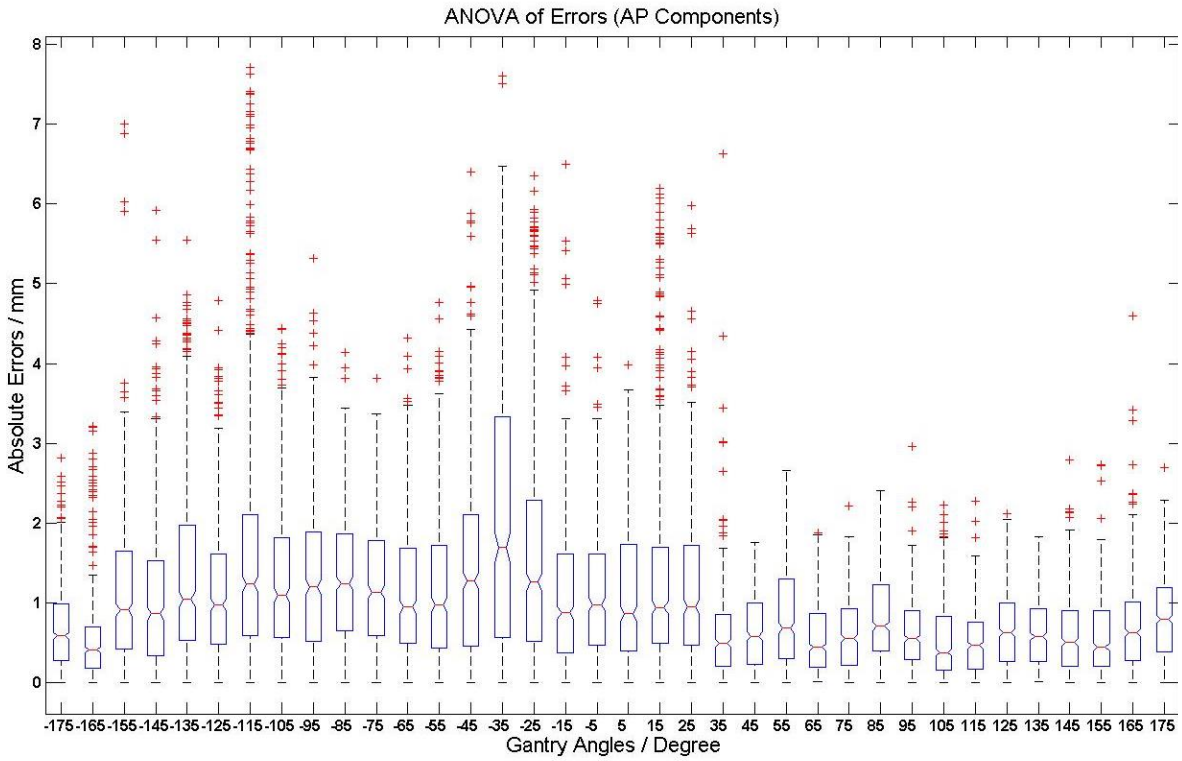

Figure 14. ANOVA test results for AP components of absolute errors with gantry angle grouping. For each group, the mean gantry angle is used to represent the group. The central of the box indicates the median value of the group and the lower and upper boundary line of the box are at the 25%/75% quantile of the data. The tick marks represent the outliers.

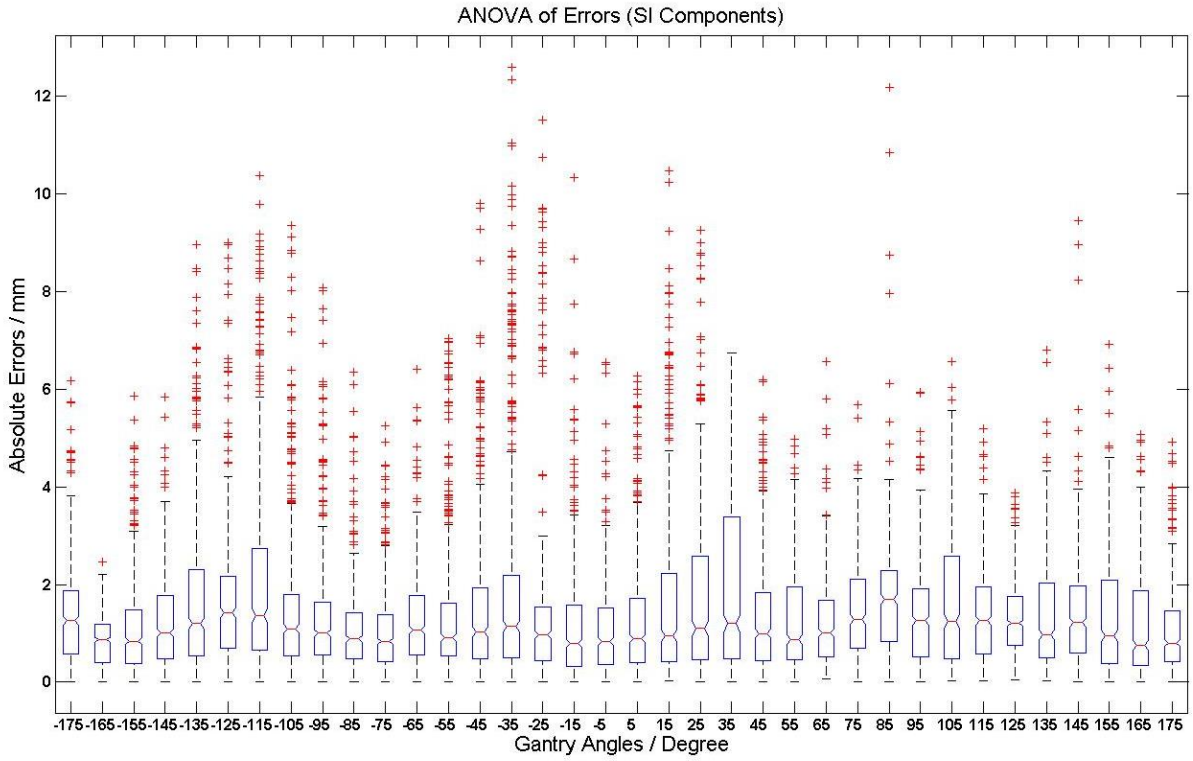

Figure 15. ANOVA test results for SI components of absolute errors with gantry angle grouping. For each group, the mean gantry angle is used to represent the group. The central of the box indicates the median value of the group and the lower and upper boundary line of the box are at the 25%/75% quantile of the data. The tick marks represent the outliers.

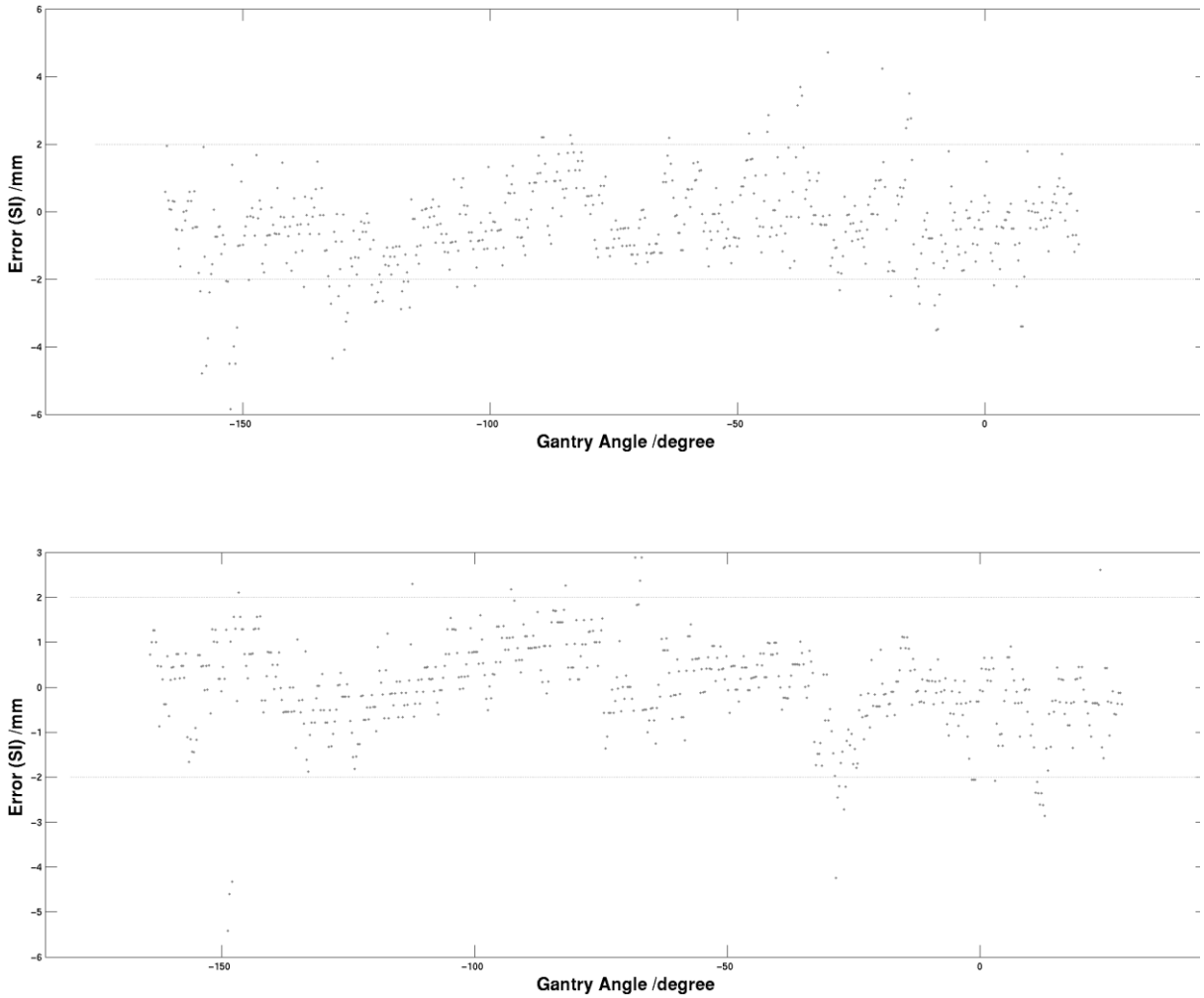

Figure 16. Patient 1 MLTM trajectory errors at SI direction. Top is the first scan and bottom is the last scan. The dots are the errors and the lines indicate error levels of ±2 mm.

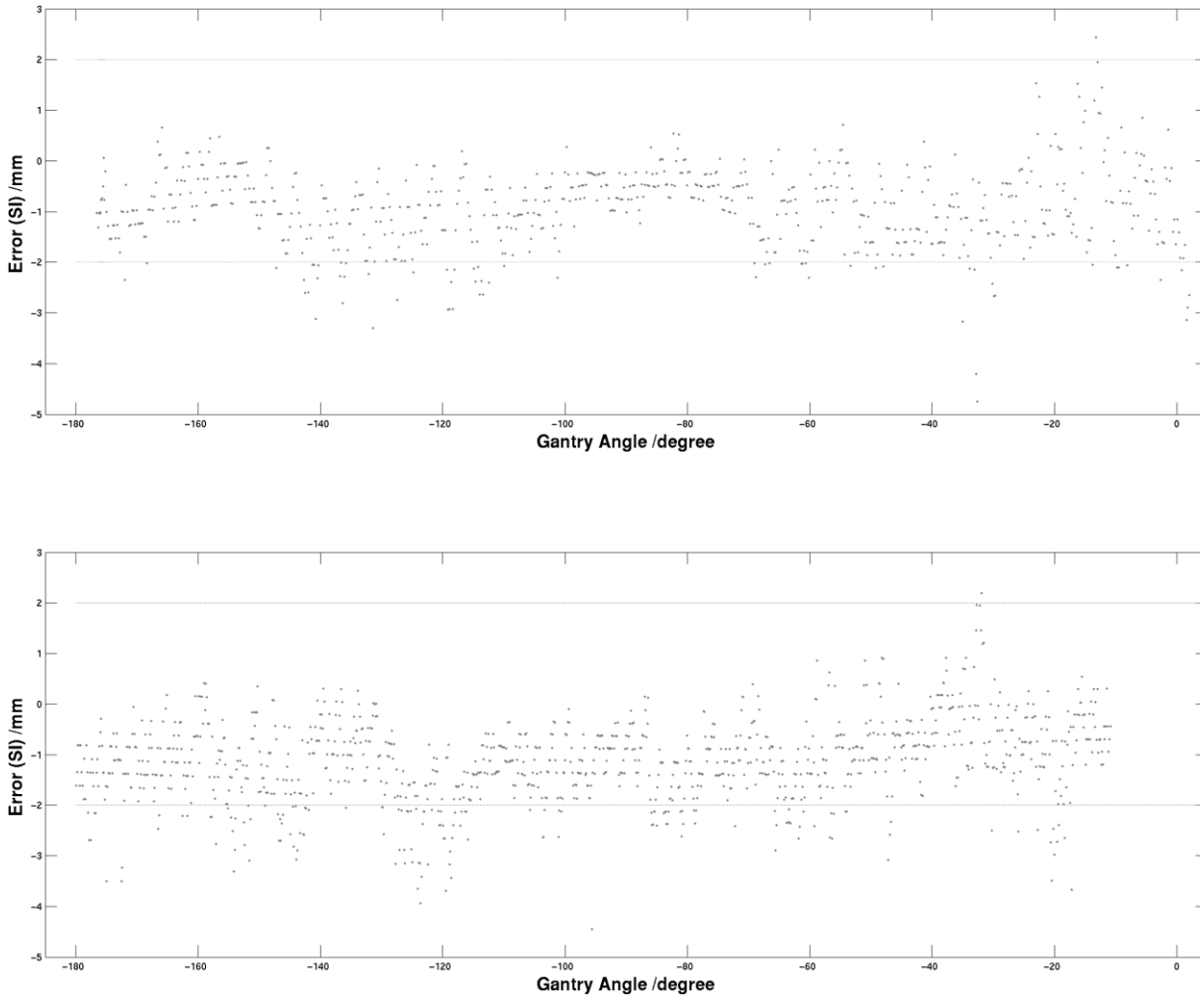

Figure 17. Patient 2 MLTM trajectory errors at SI direction. Top is the first scan and bottom is the last scan. The dots are the errors and the lines indicate error levels of ±2 mm.

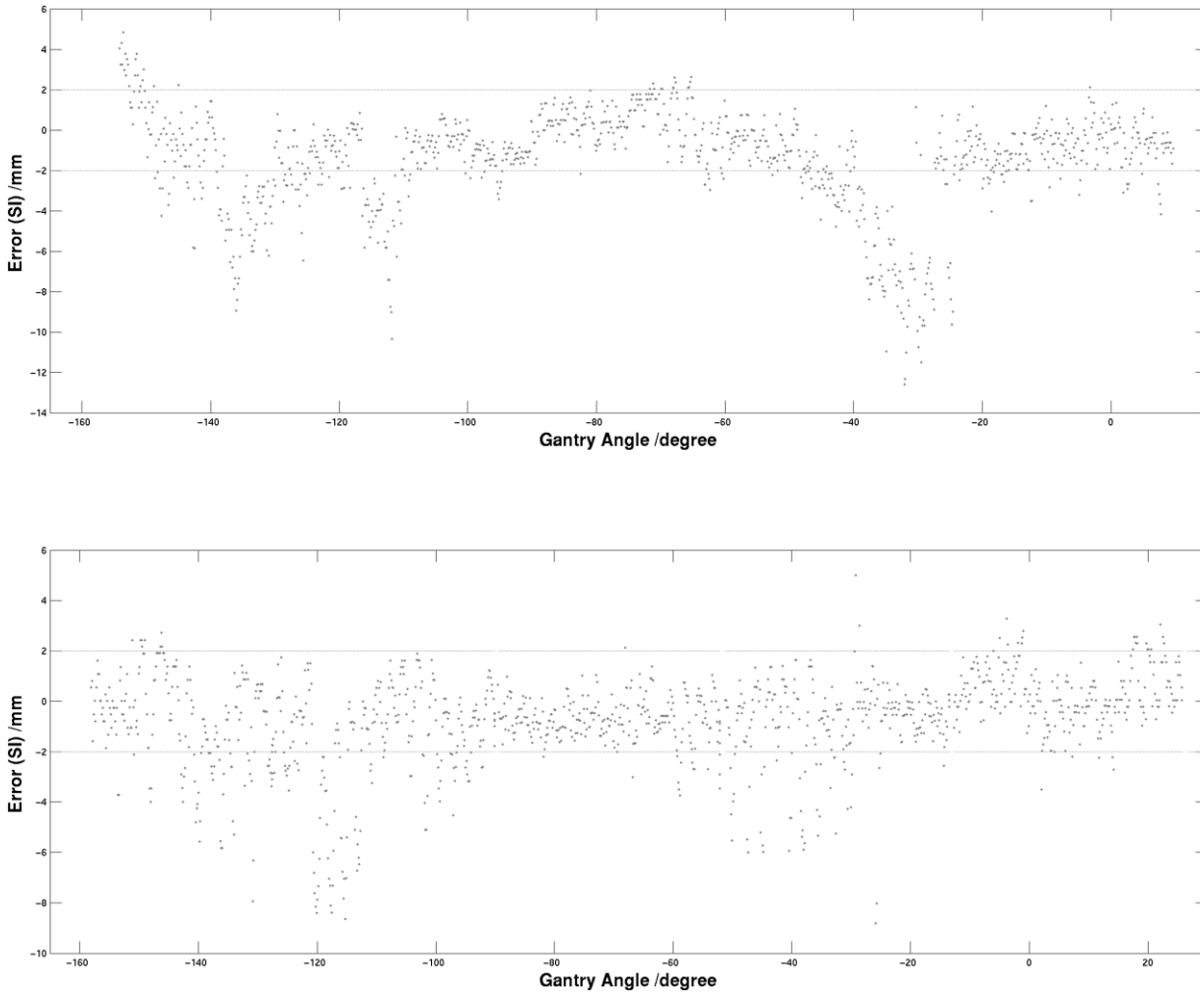

Figure 18. Patient 3 MLTM trajectory errors at SI direction. Top is the first scan and bottom is the last scan. The dots are the errors and the lines indicate error levels of ±2 mm.

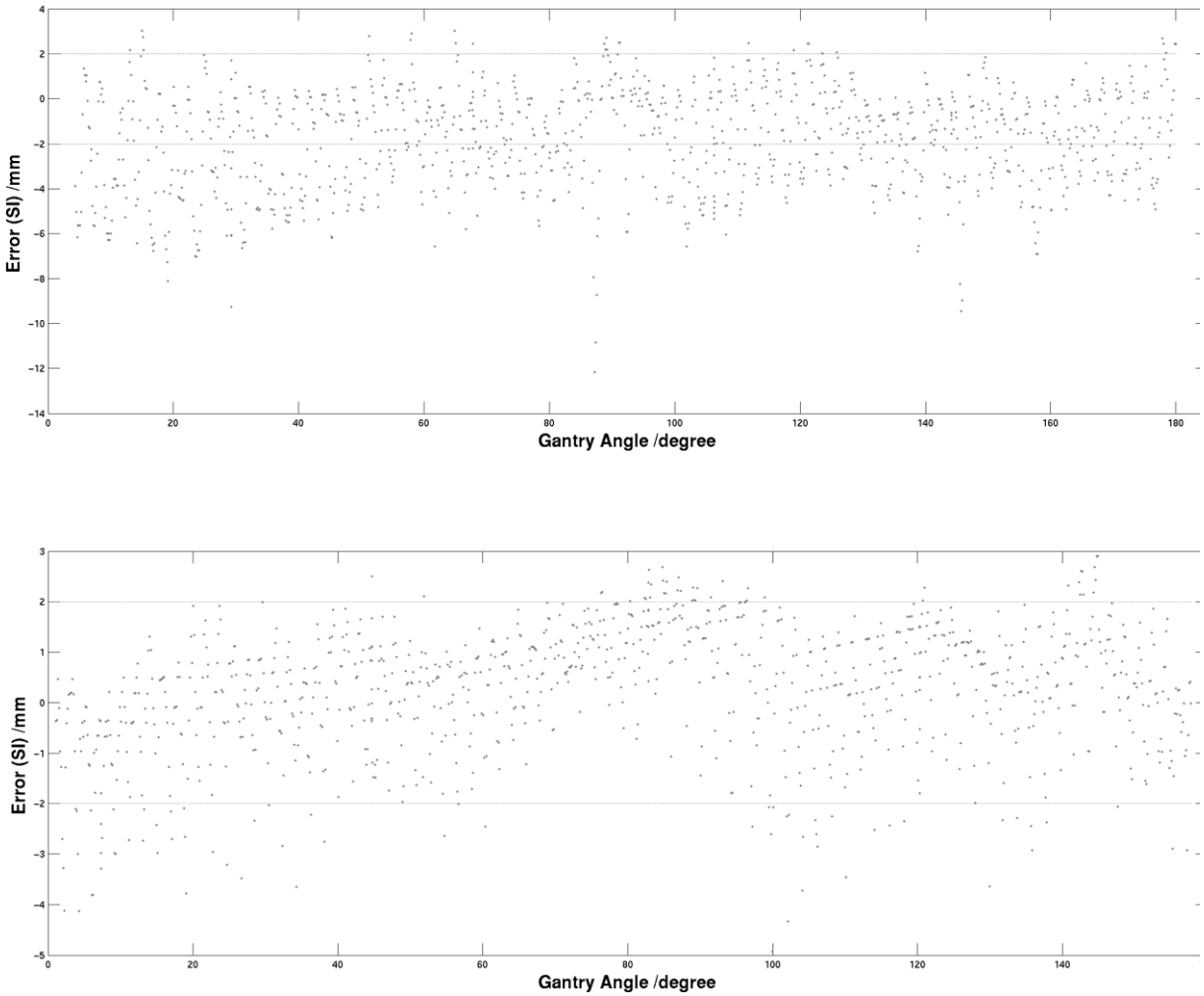

Figure 19. Patient 4 MLTM trajectory errors at SI direction. Top is the first scan and bottom is the last scan. The dots are the errors and the lines indicate error levels of ±2 mm.

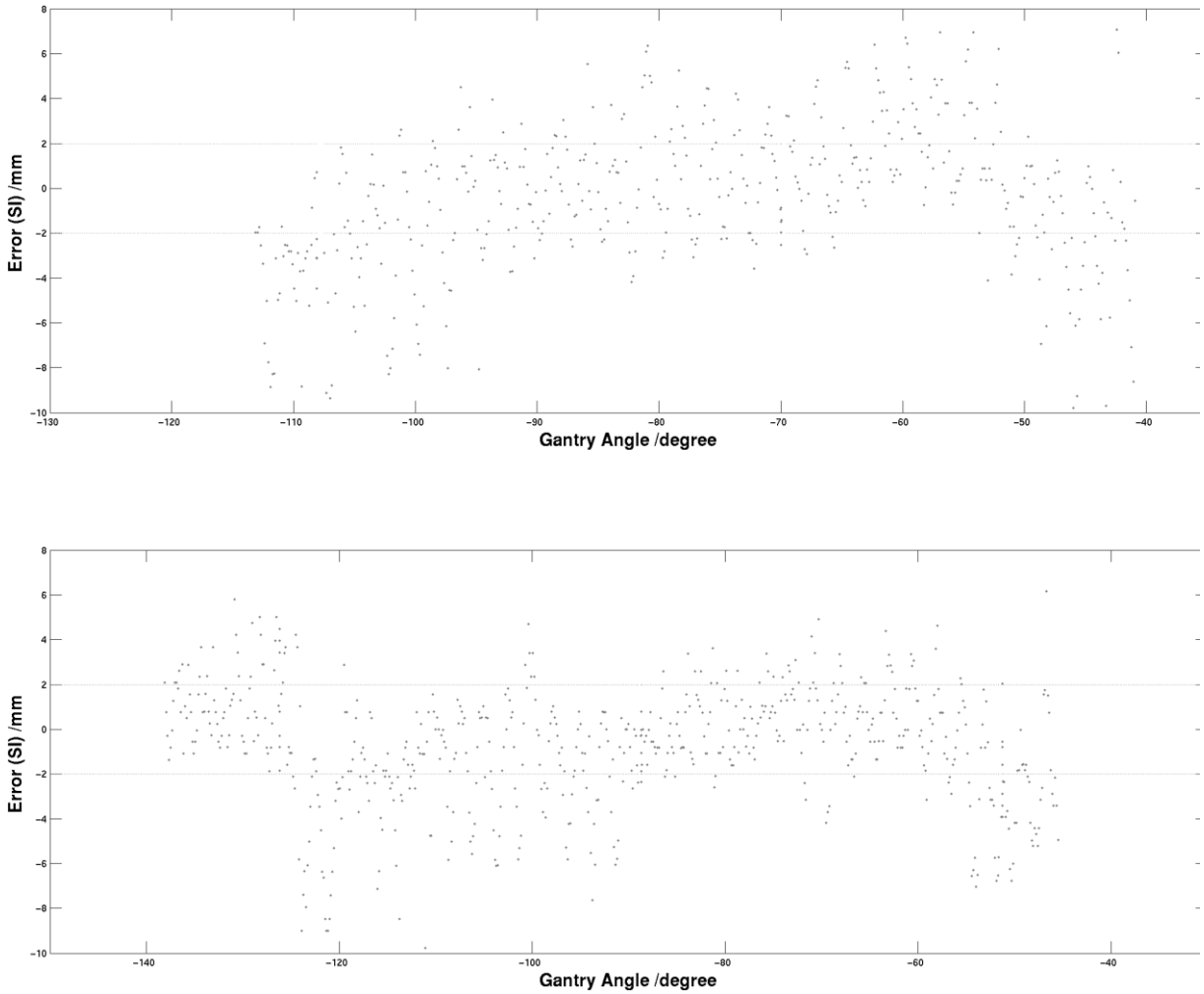

Figure 20. Patient 5 MLTM trajectory errors at SI direction. Top is the first scan and bottom is the last scan. The dots are the errors and the lines indicate error levels of ±2 mm.

5.3. Benchmarking MLTM against 4D CBCT

4D CBCT is the current clinical method to determine tumor trajectory for lung tumors. Whether MLTM outperforms the 4D CBCT needs to be evaluated. The tumor trajectory obtained from MLTM is compared against the 4D CBCT trajectory. The output of MLTM is

tumor positions as a function of time (gantry angle) while the 4D CBCT only provides average tumor position as a function of breathing phase. Tumors are delineated in every phase of the reconstructed 4D CBCT resulting the average cycle of tumor positions which includes one tumor position at each of the 10 phases. In order to conduct the comparison, the average cycle of the 4D CBCT need to be expanded to a full trajectory. Phases of all projections are predetermined. For a projection, the average phase tumor position obtained from the 4D CBCT is used to represent the tumor position of the projection and the computation is done for all projections. These positions are plot against the projections' gantry angles, resulting the 4D CBCT full trajectory. The errors of both the MLTM trajectory and the 4D CBCT full trajectory are calculated and compared. The errors of the MLTM trajectory and the 4D CBCT full tumor trajectory are listed in Table 10 and Table 11. The plots of comparing full tumor trajectories at SI direction are shown in figures from Figure 21 to Figure 25 and the average trajectories at the SI direction by grouping projections into 10 phases are shown in figures from Figure 26 to Figure 30. These tables and figures show that the MLTM algorithm outperforms the 4D CBCT in 3 patients (Patient 1,2 and 4) and no worse in 2 patients (Patient 3 and 5). The average amplitude of tumor motion measured from the 4D CBCT and the markers does not always match each other. 4D CBCT underestimates the tumor motion in several cases, for example plot (2) of Figure 26 and plot (1) of Figure 27. The factors that may cause this disagreement are delineation uncertainties, phase sorting deficiency of 4D CBCT and 4D CBCT reconstruction artifacts.

Table 10. Errors of tumor trajectory obtained from MLTM.

		Absolute Error			STDV			90% Error Level				Absolute Error			STDV			90% Error Level		
Patient	1st scan	x	y	z	x	y	z	x	y	z	Last scan	x	y	z	x	y	Z	x	y	z
1		0.9	1.2	1.0	0.5	1.2	1.2	1.5	2.5	2.2		0.7	1.9	0.7	0.6	0.8	1.0	1.3	2.5	1.6
2		0.5	0.5	1.0	0.6	0.6	0.7	1.1	2.0	1.9		0.3	0.7	1.1	0.2	0.7	0.8	0.5	1.4	2.1

3	0.5	1.4	1.8	0.7	1.1	2.1	1.1	2.7	3.9		1.5	1.6	1.3	0.6	1.2	1.8	2.2	3.6	3.0
4	1.8	0.8	2.2	0.5	0.9	2.3	2.6	1.6	4.7		1.6	0.6	1.0	0.3	0.7	1.3	1.9	1.2	2.1
5	1.4	2.0	2.6	1.3	1.4	3.3	2.8	3.5	5.8		2.4	1.2	2.1	1.1	0.9	2.7	3.8	2.2	4.8
Mean	1.1	1.3	1.8	0.8	1.1	2.1	2.0	2.5	4.0		1.5	1.3	1.3	0.6	0.9	1.7	2.2	2.3	2.9

Table 11. Errors of 4D CBCT full tumor trajectory.

		Absolute Error			**STDV**			**90% Error Level**				**Absolute Error**			**STDV**			**90% Error Level**		
Patient		x	y	z	X	y	z	x	y	Z		x	y	Z	x	y	z	x	y	z
1		1.1	3.1	3.0	0.4	1.1	1.4	1.5	4.4	4.6		2.8	3.5	2.1	0.8	1.0	1.3	3.8	4.7	3.6
2	**1st Scan**	0.8	2.0	1.6	0.7	1.0	1.8	1.6	3.4	3.2	**Last Scan**	1.7	0.7	1.3	0.6	0.8	1.4	2.4	1.5	2.9
3		0.9	0.9	1.0	1.0	0.6	1.3	1.8	1.6	2.2		6.1	1.2	1.5	0.5	0.5	1.8	6.9	1.9	3.4
4		2.3	1.4	3.1	1.3	1.3	3.9	3.6	2.5	6.2		2.2	2.2	2.0	0.4	0.8	2.0	2.7	3.3	3.8
5		3.4	1.2	2.0	1.0	1.1	2.3	4.6	2.4	4.1		4.0	2.2	3.7	1.1	0.7	1.9	5.4	3.1	6.3
Mean		2.0	1.9	2.3	0.9	1.0	2.3	2.9	3.0	4.3		3.7	2.2	2.3	0.7	0.8	1.7	4.6	3.1	4.2

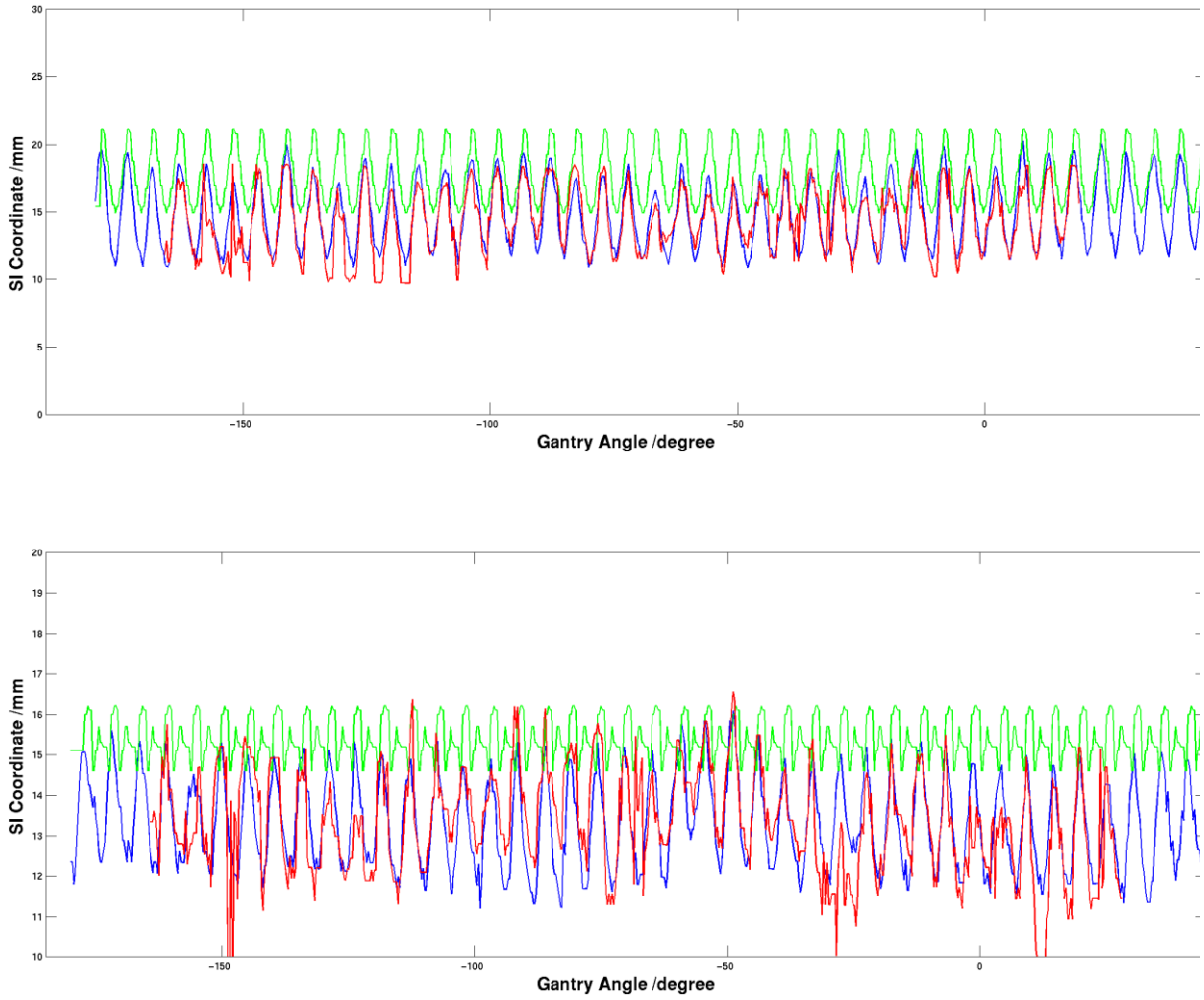

Figure 21. Patient 1 trajectories comparison at SI direction. The green curve in each plot is the 4D CBCT full trajectory, red curve is the MLTM trajectory, and blue curve is the reference trajectory. The top plot shows the trajectories of the first scan and the bottom plot shows trajectories of the last scan.

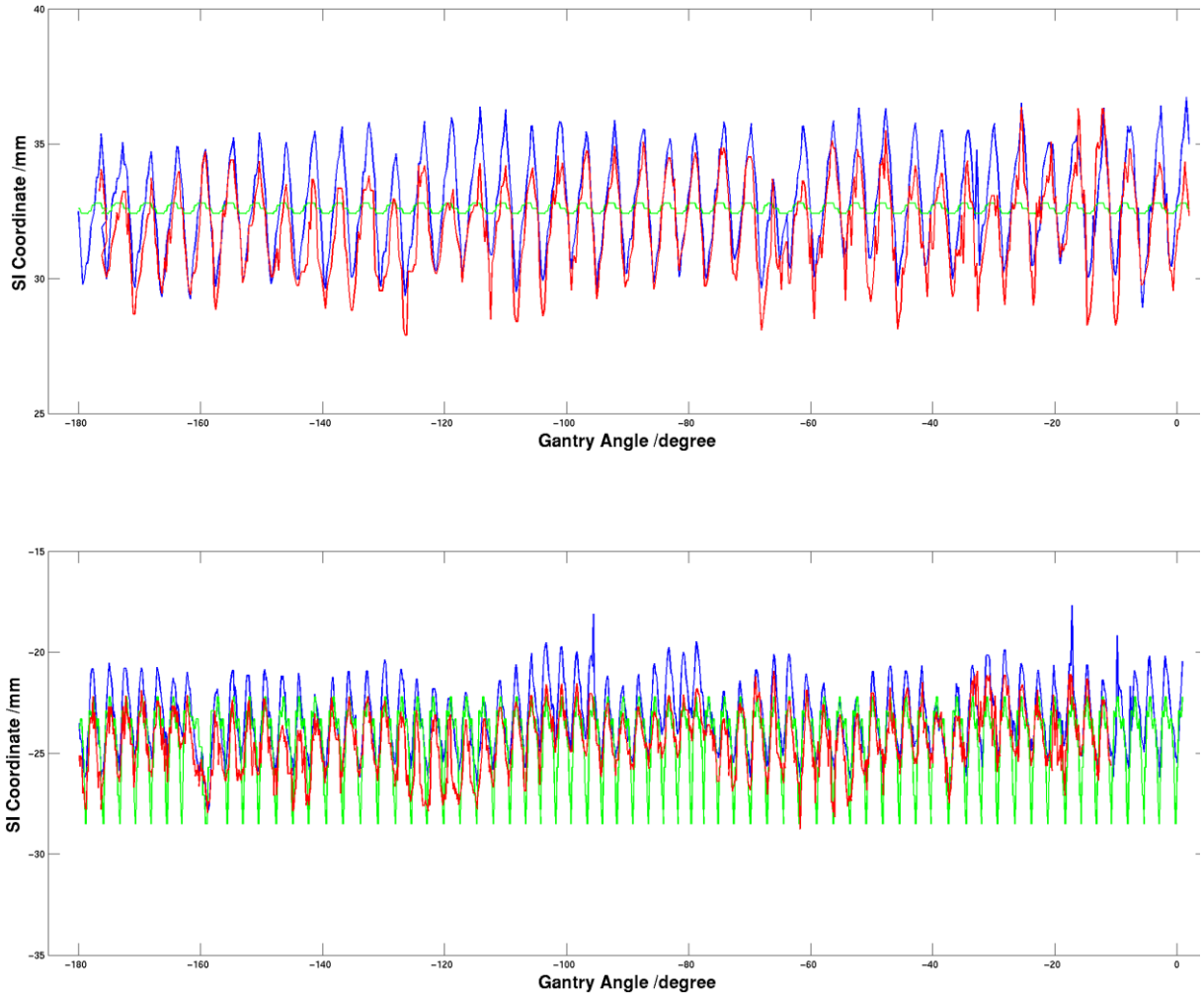

Figure 22. Patient 2 trajectories comparison at SI direction. The green curve in each plot is the 4D CBCT full trajectory, red curve is the MLTM trajectory, and blue curve is the reference trajectory. The top plot shows the trajectories of the first scan and the bottom plot shows trajectories of the last scan.

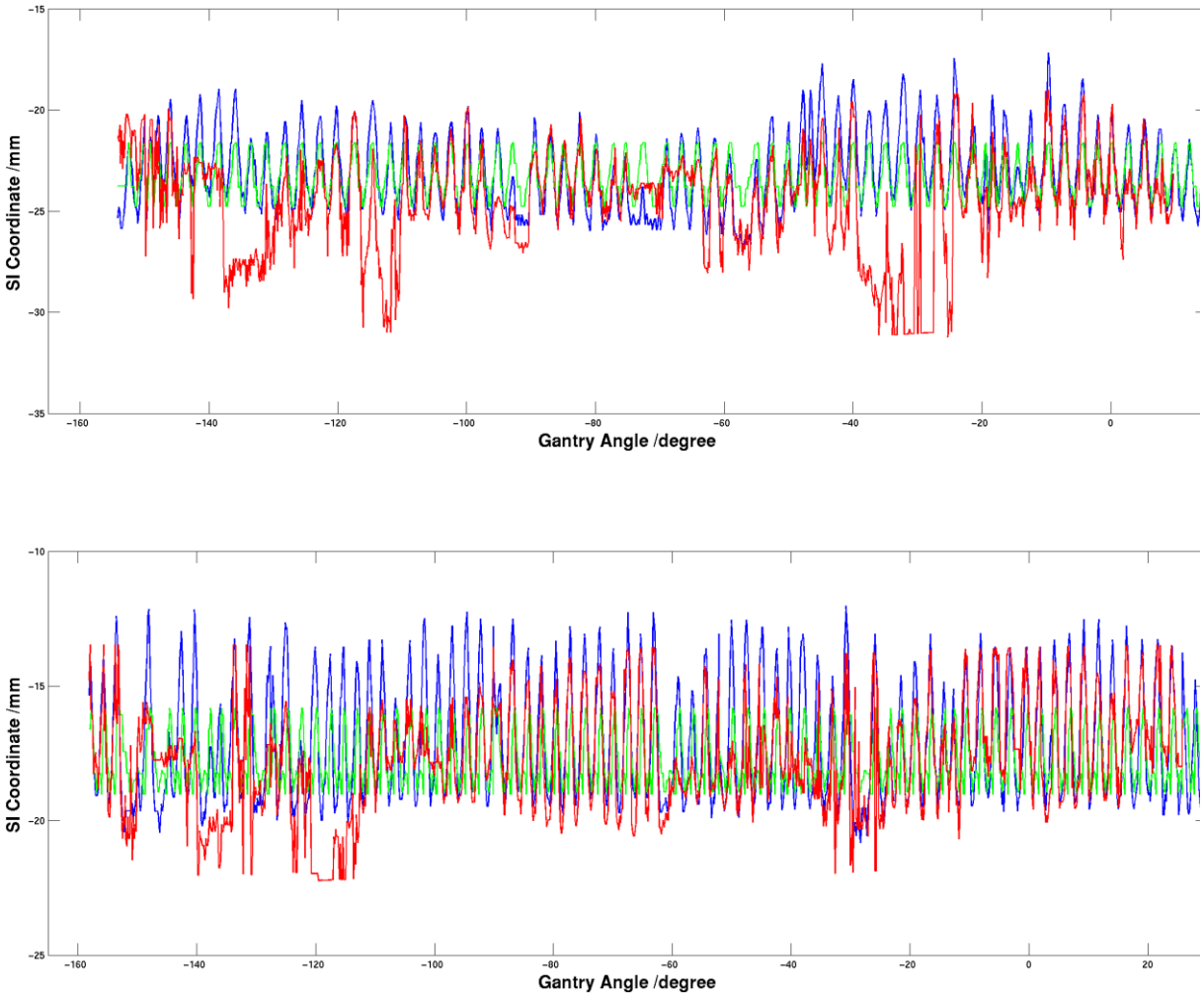

Figure 23. Patient 3 trajectories comparison at SI direction. The green curve in each plot is the 4D CBCT full trajectory, red curve is the MLTM trajectory, and blue curve is the reference trajectory. The top plot shows the trajectories of the first scan and the bottom plot shows trajectories of the last scan.

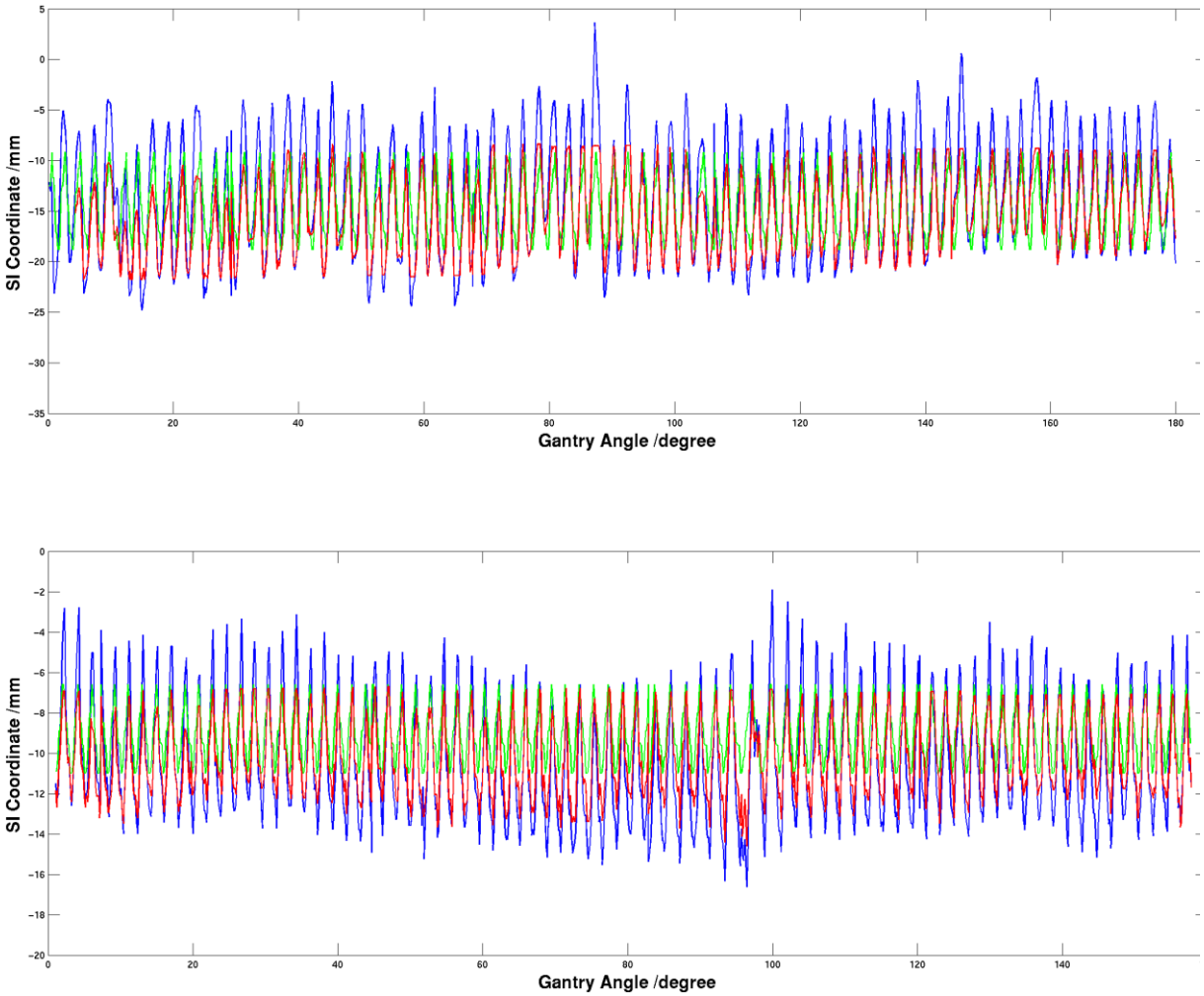

Figure 24. Patient 4 trajectories comparison at SI direction. The green curve in each plot is the 4D CBCT full trajectory, red curve is the MLTM trajectory, and blue curve is the reference trajectory. The top plot shows the trajectories of the first scan and the bottom plot shows trajectories of the last scan.

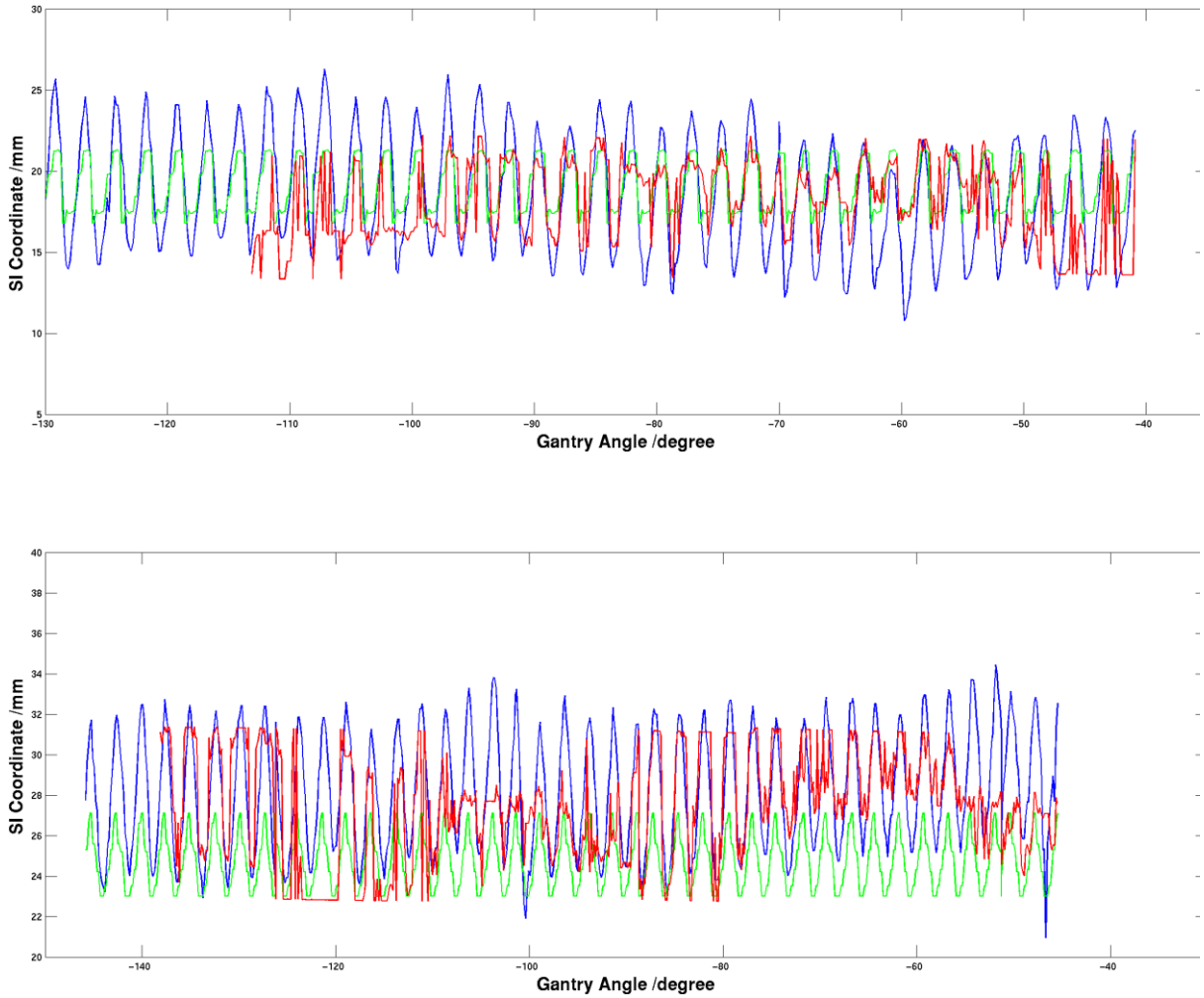

Figure 25. Patient 5 trajectories comparison at SI direction. The green curve in each plot is the 4D CBCT full trajectory, red curve is the MLTM trajectory, and blue curve is the reference trajectory. The top plot shows the trajectories of the first scan and the bottom plot shows trajectories of the last scan.

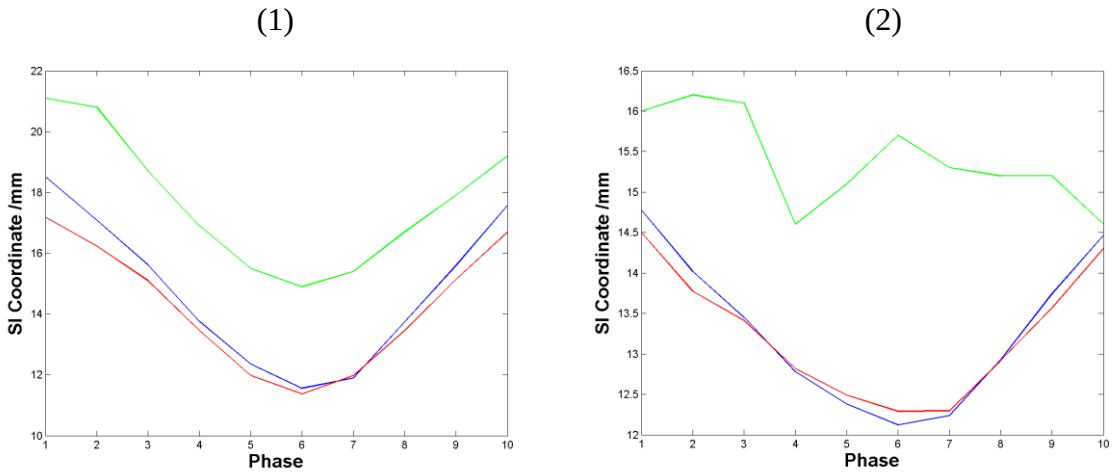

Figure 26. Patient 1 average trajectories comparison at SI direction. The green curve in each plot is the 4D CBCT average trajectory, red curve is the MLTM average trajectory, and blue curve is the reference average trajectory. The left plot shows the trajectories of the first scan and the right plot shows the trajectories of last scan.

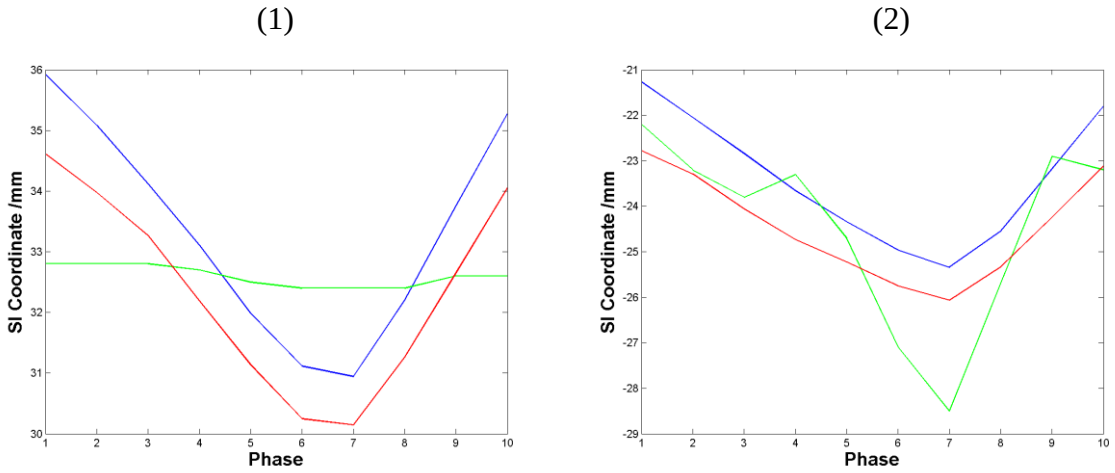

Figure 27. Patient 2 average trajectories comparison at SI direction. The green curve in each plot is the 4D CBCT average trajectory, red curve is the MLTM average trajectory, and blue curve is the reference average trajectory. The left plot shows the trajectories of the first scan and the right plot shows the trajectories of last scan.

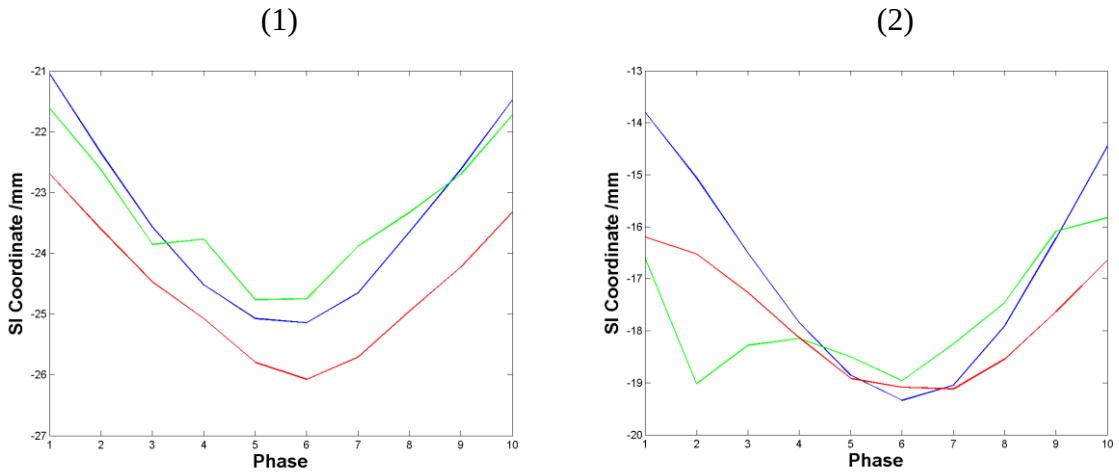

Figure 28. Patient 3 average trajectories comparison at SI direction. The green curve in each plot is the 4D CBCT average trajectory, red curve is the MLTM average trajectory, and blue curve is the reference average trajectory. The left plot shows the trajectories of the first scan and the right plot shows the trajectories of last scan.

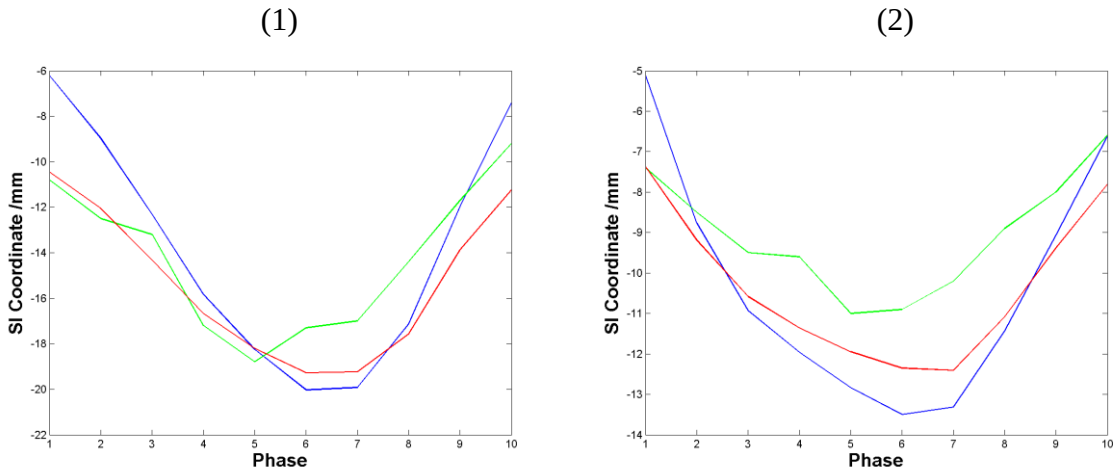

Figure 29. Patient 4 average trajectories comparison at SI direction. The green curve in each plot is the 4D CBCT average trajectory, red curve is the MLTM average trajectory, and blue curve is the reference average trajectory. The left plot shows the trajectories of the first scan and the right plot shows the trajectories of last scan.

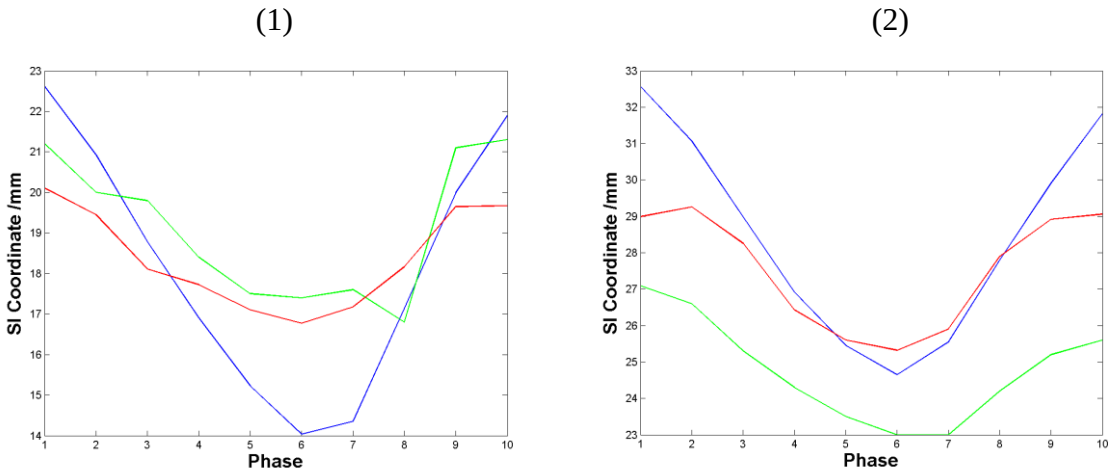

Figure 30. Patient 5 average trajectories comparison at SI direction. The green curve in each plot is the 4D CBCT average trajectory, red curve is the MLTM average trajectory, and blue curve is the reference average trajectory. The left plot shows the trajectories of the first scan and the right plot shows the trajectories of last scan.

5.4. Conclusion

The tracking results are not as good at some gantry angles. One may avoid use data from those angles as to form the final tumor trajectory. The results also indicate that MLTM is at least not worse than 4D CBCT and it outperforms 4D CBCT in sum.

6. Discussion and Conclusions

6.1. Discussion and Conclusions

This dissertation is focused on the development of a temporal markerless lung tumor trajectory estimation algorithm with clinical acceptable accuracy. By this, one is able to characterize the patient-specific tumor motion pattern, which outperforms 4D CBCT without the need for invasive fiducial implantation. The resulting tumor motion pattern is a crucial input component for generating patient-specific GTV to PTV margin in adaptive radiotherapy and incorporating variability models into 4D inverse treatment planning. The reduced margin treatment plans could spare more normal tissue or escalate the dose prescribed to the tumor. This motivated the implementation and development of MLTM as the primary focus of this dissertation. Chapter 1 introduced the rationale for the research problem and intended research design.

As a reliable validation method is lacking, a validation framework based on fiducial markers is developed and evaluated in Chapter 2 to assess MLTM. TMD_DIR is selected to correct the segmented marker trajectory to tumor trajectory as the reference. The accuracy of the validation framework is 1.8 mm, indicating that TMD_DIR + marker trajectory is a reliable validation method for MLTM. The major limitation is that the calculation of the uncertainties is based on the assumption that the physician delineation is the ground truth. However, the delineation itself introduces uncertainties. In this study, the patients are delineated by one physician, so inter-

observer variability is not considered. Ideally, the intra-observer variation of tumor delineation could be separately quantified to enable calculation of uncertainties. It is not separated from the inter- and intra-fractional variation due to the overall small magnitude of the total variability.

MLTM is developed and improved to acquire tumor trajectory with clinical acceptable accuracy for lung patients with locally advanced lesions in Chapter 3 and Chapter 4. The development is separated into two parts by whether considering tumor deformation. The first development (Chapter 3) is taken place on the first available weekly CBCT under the assumption that time is not a variable in consideration meaning that tumor is with minimal or none deformation. Shape and appearance of the template is investigated, and 3 types of templates (Ex-GTV template, cylinder template, and padded template) are studied and compared. A constraint method is introduced to constrain template matching searching region for more precise matching results. Padded template is selected as the template and the constraint method further reduce the tracking errors from 3.5 mm to 2.1 mm. The second part (Chapter 4) is to accommodate the MLDM to account for time influence which is tumor deformation due to treatment response for the later fraction CBCT. B-spline DIR is demonstrated to be accurate and adequate to transform masked CT for the generation of TT in MLDM and the accuracy is 2.4 mm.

In Chapter 5, the results of MLDM are analyzed and compared against 4D CBCT. Statistically, gantry angles affect the tracking results. At gantry angles from -150 ºto -110 º, -60 º to -30 º, the MLDM algorithm has worse results. At these angles, radiation beams penetrating more bony structures (ribs) than other angles and the tumor contrast is poorer. MLDM is at least not worse than 4D CBCT and outperforms 4D CBCT in summary.

One limitation of MLDM is the tumor contrast. One direction of the future work will be developing a robust method to improve tumor contrast. A challenging task will be adapting the algorithm to real time. The latency due to the computation time of the algorithm and how to acquire daily tumor information before the daily CBCT will be the main concern.

6.2. Original Contributions

In this dissertation, specific contributions include:

(1). A marker painting technique is employed to eliminate the effect of markers on template matching as stated in Appendix I. Fiducial markers are implanted in the patients inside the tumors. They are radiopaque and with high intensity contrast in radiographic images. When conducting template matching of planning tumor to daily tumor, the existence of marker inside the tumor may bias the results. An interpolation based marker painting technique is developed to remove markers from every projection image of a CBCT scan. The technique successfully removes markers and reduces the effect of markers on template matching by both phantom and clinical observations.

(2). A new method to validate markerless tracking algorithm is developed and investigated in this work. The validation framework is based on fiducial markers that implanted inside or near the tumors. The details of the framework development are introduced in Chapter 2. The validation method is with acceptable accuracy and is employed in the result analysis in this dissertation.

(3). A new type of tumor template, padded template, is introduced and compared to the existing templates, i.e. Ex-GTV template and cylinder template in Chapter 3. Padded template is edited in the gradient map of Ex-GTV template. This editing is more direct

and results in more accurate definition of tumor in tumor template. The results support this statement and they show that the tracking errors are much smaller by using padded template.

(4). A novel prediction method is developed to constrain the search region for template matching to obtain better matching results in Chapter 3. The method is developed under the condition that it is a retrospective study. The method iterates the process of MLTM twice. The first running is considered as the training data to obtain an average breathing cycle which is considered as the predicted position in the second running. This method is able to reduce the search region in the template matching process and provides more accurate tracking results.

The author also makes contributions in improving the efficiency of computation, development and writing of the codes, data collection of marker segmentation, as well as bug detection of RCF library.

References

1 J. Ferlay, H. Shin, F. Bray, D. Forman, C. Mathers, D.M. Parkin, "Estimates of worldwide burden of cancer in 2008: GLOBOCAN 2008," International journal of cancer **127**, 2893-2917 (2010).

2 D.M. Parkin, F. Bray, J. Ferlay, P. Pisani, "Global cancer statistics, 2002," CA: a cancer journal for clinicians **55**, 74-108 (2005).

3 G.S. Sibley M.D., P.D. Jamieson M.D. Timothy A., L.B. Marks M.D., M.S. Anscher M.D., L.R. Prosnitz M.D., "Radiotherapy Alone for Medically Inoperable Stage I Non-Small–Cell Lung Cancer: The Duke Experience," International Journal of Radiation Oncology*Biology*Physics **40**, 149-154 (1998).

4 M. van Herk, "Errors and margins in radiotherapy," presented at Seminars in radiation oncology.

5 J.M. Links, L.S. Beach, B. Subramaniam, M.A. Rubin, J.G. Hennessey, A.L. Reiss, "Edge complexity and partial volume effects," J. Comput. Assist. Tomogr. **22**, 450-458 (1998).

6 International Commission on Radiation Units and Measurements, *Prescribing, Recording, and Reporting Photon Beam Therapy* (International Commission on Radiation Units and Measurements, Bethesda, MD, U.S.A., 1993).

7 L. Ekberg, O. Holmberg, L. Wittgren, G. Bjelkengren, T. Landberg, "What margins should be added to the clinical target volume in radiotherapy treatment planning for lung cancer?" Radiotherapy and Oncology **48**, 71-77 (1998).

8 H.C.J. de Boer, van Sörnsen de Koste,John R., S. Senan, A.G. Visser, B.J.M. Heijmen, "Analysis and reduction of 3D systematic and random setup errors during the simulation and treatment of lung cancer patients with CT-based external beam radiotherapy dose planning," International Journal of Radiation Oncology*Biology*Physics **49**, 857-868 (2001).

9 S.C. Erridge, Y. Seppenwoolde, S.H. Muller, M. van Herk, K. De Jaeger, J.S.A. Belderbos, L.J. Boersma, J.V. Lebesque, "Portal imaging to assess set-up errors, tumor motion and tumor shrinkage during conformal radiotherapy of non-small cell lung cancer," Radiotherapy and Oncology **66**, 75-85 (2003).

10 G.R. Borst, J. Sonke, A. Betgen, P. Remeijer, M. van Herk, J.V. Lebesque, "Kilo-Voltage Cone-Beam Computed Tomography Setup Measurements for Lung Cancer Patients; First Clinical Results and Comparison With Electronic Portal-Imaging Device," International Journal of Radiation Oncology*Biology*Physics **68**, 555-561 (2007).

11 P. Giraud, M. Antoine, A. Larrouy, B. Milleron, P. Callard, Y. De Rycke, M. Carette, J. Rosenwald, J. Cosset, M. Housset, E. Touboul, "Evaluation of microscopic tumor extension

in non–small-cell lung cancer for three-dimensional conformal radiotherapy planning," International Journal of Radiation Oncology*Biology*Physics **48**, 1015-1024 (2000).

12 I.S. Grills, D.L. Fitch, N.S. Goldstein, D. Yan, G.W. Chmielewski, R.J. Welsh, L.L. Kestin, "Clinicopathologic Analysis of Microscopic Extension in Lung Adenocarcinoma: Defining Clinical Target Volume for Radiotherapy," International Journal of Radiation Oncology*Biology*Physics **69**, 334-341 (2007).

13 G. Hugo, C. Vargas, J. Liang, L. Kestin, J.W. Wong, D. Yan, "Changes in the respiratory pattern during radiotherapy for cancer in the lung," Radiother. Oncol. **78**, 326-331 (2006).

14 J. Chang, G.S. Mageras, E. Yorke, F. De Arruda, J. Sillanpaa, K.E. Rosenzweig, A. Hertanto, H. Pham, E. Seppi, A. Pevsner, "Observation of interfractional variations in lung tumor position using respiratory gated and ungated megavoltage cone-beam CT," Int. J. Radiat. Oncol. Biol. Phys. **67**, 1548 (2007).

15 J.J. Sonke, J. Lebesque, M. van Herk, "Variability of four-dimensional computed tomography patient models," Int. J. Radiat. Oncol. Biol. Phys. **70**, 590-598 (2008).

16 L. Ekberg, O. Holmberg, L. Wittgren, G. Bjelkengren, T. Landberg, "What margins should be added to the clinical target volume in radiotherapy treatment planning for lung cancer?" Radiotherapy and oncology **48**, 71-77 (1998).

17 Y. Seppenwoolde, H. Shirato, K. Kitamura, S. Shimizu, M. van Herk, J. Lebesque, K. Miyasaka, "Precise and real-time measurement of 3D tumor motion in lung due to breathing

and heartbeat, measured during radiotherapy." Int. J. Radiat. Oncol. Biol. Phys. **53**, 822-834 (2002).

18 H. Shirato, Y. Seppenwoolde, K. Kitamura, R. Onimura, S. Shimizu, "Intrafractional tumor motion: lung and liver." Semin. Radiat. Oncol. **14**, 10-18 (2004).

19 International Commission on Radiation Units and Measurements, *Prescribing, Recording, and Reporting Photon Beam Therapy* (International Commission on Radiation Units and Measurements, Bethesda, Md., 1999).

20 C. Schaake-Koning, d.B. van, O. Dalesio, J. Festen, J. Hoogenhout, P. van Houtte, A. Kirkpatrick, M. Koolen, B. Maat, A. Nijs, A. Renaud, P. Rodrigus, L. Schuster-Uitterhoeve, J. Sculier, N. van Zandwijk, H. Bartelink, "Effects of Concomitant Cisplatin and Radiotherapy on Inoperable Non-Small-Cell Lung Cancer," N. Engl. J. Med. **326**, 524-530 (1992).

21 M.K. Martel, R.K. Ten Haken, M.B. Hazuka, M.L. Kessler, M. Strawderman, A.T. Turrisi, T.S. Lawrence, B.A. Fraass, A.S. Lichter, "Estimation of tumor control probability model parameters from 3-D dose distributions of non-small cell lung cancer patients," Lung Cancer **24**, 31-37 (1999).

22 M. Mehta, R. Scrimger, R. Mackie, B. Paliwal, R. Chappell, J. Fowler, "A new approach to dose escalation in non–small-cell lung cancer," International Journal of Radiation Oncology*Biology*Physics **49**, 23-33 (2001).

23 F. Kong, R.K. Ten Haken, M.J. Schipper, M.A. Sullivan, M. Chen, C. Lopez, G.P. Kalemkerian, J.A. Hayman, "High-dose radiation improved local tumor control and overall survival in patients with inoperable/unresectable non–small-cell lung cancer: Long-term results of a radiation dose escalation study," International Journal of Radiation Oncology*Biology*Physics **63**, 324-333 (2005).

24 J.S.A. Belderbos, W.D. Heemsbergen, K. De Jaeger, P. Baas, J.V. Lebesque, "Final results of a Phase I/II dose escalation trial in non–small-cell lung cancer using three-dimensional conformal radiotherapy," International Journal of Radiation Oncology*Biology*Physics **66**, 126-134 (2006).

25 A. Auperin, E. Rolland, W.J. Curran, K. Furuse, P. Fournel, J. Belderbos, G. Clamon, H.C. Ulutin, L. Stewart, C. Le Pechoux, "Concomitant radio-chemotherapy (RT-CT) versus sequential RT-CT in locally advanced non-small cell lung cancer (NSCLC): A meta-analysis using individual patient data (IPD) from randomised clinical trials (RCTs): A1-05," Journal of Thoracic Oncology **2**, S310 (2007).

26 S. Shimizu, H. Shirato, S. Ogura, H. Akita-Dosaka, K. Kitamura, T. Nishioka, K. Kagei, M. Nishimura, K. Miyasaka, "Detection of lung tumor movement in real-time tumor-tracking radiotherapy," International Journal of Radiation Oncology* Biology* Physics **51**, 304-310 (2001).

27 Q. Xu and R.J. Hamilton, "A novel respiratory detection method based on automated analysis of ultrasound diaphragm video," Med. Phys. **33**, 916 (2006).

28 J.W. Wong, M.B. Sharpe, D.A. Jaffray, V.R. Kini, J.M. Robertson, J.S. Stromberg, A.A. Martinez, "The use of active breathing control (ABC) to reduce margin for breathing motion* 1," International Journal of Radiation Oncology* Biology* Physics **44**, 911-919 (1999).

29 M.J. Murphy, J.R. Adler, M. Bodduluri, J. Dooley, K. Forster, J. Hai, Q. Le, G. Luxton, D. Martin, J. Poen, "Image-guided radiosurgery for the spine and pancreas," Computer Aided Surgery **5**, 278-288 (2000).

30 M.J. Murphy, "Tracking moving organs in real time," presented at Seminars in radiation oncology.

31 D. Yan, F. Vicini, J. Wong, A. Martinez, "Adaptive radiation therapy." Phys. Med. Biol. **42**, 123-132 (1997).

32 J. Löf, B.K. Lind, A. Brahme, "An adaptive control algorithm for optimization of intensity modulated radiotherapy considering uncertainties in beam profiles, patient set-up and internal organ motion," Phys. Med. Biol. **43**, 1605 (1998).

33 D. Yan, D. Lockman, D. Brabbins, L. Tyburski, A. Martinez, "An off-line strategy for constructing a patient-specific planning target volume in adaptive treatment process for prostate cancer." Int. J. Radiat. Oncol. Biol. Phys. **48**, 289-302 (2000).

34 G. Hugo, D. Yan, J. Liang, "Population and patient-specific target margins for 4D adaptive radiotherapy to account for intra- and inter-fraction variation in lung tumour position." Phys. Med. Biol. **52**, 257-274 (2007).

35 D. Yan, "Adaptive radiotherapy: merging principle into clinical practice." Semin. Radiat. Oncol. **20**, 79-83 (2010).

36 T. Zhang, R. Jeraj, H. Keller, W. Lu, G.H. Olivera, T.R. McNutt, T.R. Mackie, B. Paliwal, "Treatment plan optimization incorporating respiratory motion," Med. Phys. **31**, 1576 (2004).

37 I.J. Chetty, M. Rosu, D.L. McShan, B.A. Fraass, J.M. Balter, R.K. Ten Haken, "Accounting for center-of-mass target motion using convolution methods in Monte Carlo-based dose calculations of the lung," Med. Phys. **31**, 925 (2004).

38 A. Trofimov, E. Rietzel, H.M. Lu, B. Martin, S. Jiang, G.T.Y. Chen, T. Bortfeld, "Temporo-spatial IMRT optimization: concepts, implementation and initial results," Phys. Med. Biol. **50**, 2779 (2005).

39 X. Li, P. Zhang, D. Mah, R. Gewanter, G. Kutcher, "Novel lung IMRT planning algorithms with nonuniform dose delivery strategy to account for respiratory motion," Med. Phys. **33**, 3390 (2006).

40 T. Zhang, H. Keller, M.J. O'Brien, T.R. Mackie, B. Paliwal, "Application of the spirometer in respiratory gated radiotherapy," Med. Phys. **30**, 3165 (2003).

41 H.D. Kubo, P.M. Len, S. Minohara, H. Mostafavi, "Breathing-synchronized radiotherapy program at the University of California Davis Cancer Center," Med. Phys. **27**, 346 (2000).

42 A. Schweikard, G. Glosser, M. Bodduluri, M.J. Murphy, J.R. Adler, "Robotic motion compensation for respiratory movement during radiosurgery," Computer Aided Surgery **5**, 263-277 (2000).

43 Y. Seppenwoolde, R.I. Berbeco, S. Nishioka, H. Shirato, B. Heijmen, "Accuracy of tumor motion compensation algorithm from a robotic respiratory tracking system: a simulation study," Med. Phys. **34**, 2774 (2007).

44 C. OZHASOGLU and M.J. MURPHY, "Issues in respiratory motion compensation during external-beam radiotherapy," Int. J. Radiat. Oncol. Biol. Phys. **52**, 1389-1399 (2002).

45 S. Vedam, V. Kini, P. Keall, V. Ramakrishnan, H. Mostafavi, R. Mohan, "Quantifying the predictability of diaphragm motion during respiration with a noninvasive external marker," Med. Phys. **30**, 505 (2003).

46 J.D.P. Hoisak, K. Sixel, R. Tirona, P.C.F. Cheung, J. Pignol, "Correlation of lung tumor motion with external surrogate indicators of respiration." Int. J. Radiat. Oncol. Biol. Phys. **60**, 1298-1306 (2004).

47 S. Ahn, B. Yi, Y. Suh, J. Kim, S. Lee, S. Shin, E. Choi, "A feasibility study on the prediction of tumour location in the lung from skin motion," Br. J. Radiol. **77**, 588 (2004).

48 N. Koch, H.H. Liu, G. Starkschall, M. Jacobson, K. Forster, Z. Liao, R. Komaki, C.W. Stevens, "Evaluation of internal lung motion for respiratory-gated radiotherapy using MRI: Part I--correlating internal lung motion with skin fiducial motion* 1," International Journal of Radiation Oncology* Biology* Physics **60**, 1459-1472 (2004).

49 D. Ionascu, S. Jiang, S. Nishioka, H. Shirato, R. Berbeco, "Internal-external correlation investigations of respiratory induced motion of lung tumors." Med. Phys. **34**, 3893-3903 (2007).

50 S. Hunjan, G. Starkschall, K. Prado, L. Dong, P. Balter, "Lack of correlation between external fiducial positions and internal tumor positions during breath-hold CT." Int. J. Radiat. Oncol. Biol. Phys. **76**, 1586-1591 (2010).

51 Y. Tsunashima, T. Sakae, Y. Shioyama, K. Kagei, T. Terunuma, A. Nohtomi, Y. Akine, "Correlation between the respiratory waveform measured using a respiratory sensor and 3D tumor motion in gated radiotherapy," Int. J. Radiat. Oncol. Biol. Phys. **60** (2004).

52 J.H. Killoran, A.M. Allen, B.H. Kann, Y. Lyatskaya, "Inter fractional variability of breathing phase definition as determined by fiducial location," Med. Phys. **35**, 753 (2008).

53 S. Shimizu, H. Shirato, K. Kitamura, N. Shinohara, T. Harabayashi, T. Tsukamoto, T. Koyanagi, K. Miyasaka, "Use of an implanted marker and real-time tracking of the marker for the positioning of prostate and bladder cancers," International Journal of Radiation Oncology* Biology* Physics **48**, 1591-1597 (2000).

54 X. Tang, G.C. Sharp, S.B. Jiang, "Fluoroscopic tracking of multiple implanted fiducial markers using multiple object tracking," Phys. Med. Biol. **52**, 4081 (2007).

55 P G Seiler and H Blattmann and S Kirsch and R K Muench and,Ch Schilling, "A novel tracking technique for the continuous precise measurement of tumour positions in conformal radiotherapy," Phys. Med. Biol. **45**, N103 (2000).

56 J.M. Balter, J.N. Wright, L.J. Newell, B. Friemel, S. Dimmer, Y. Cheng, J. Wong, E. Vertatschitsch, T.P. Mate, "Accuracy of a wireless localization system for radiotherapy," International Journal of Radiation Oncology*Biology*Physics **61**, 933-937 (2005).

57 H. Shirato, S. Shimizu, T. Shimizu, T. Nishioka, K. Miyasaka, "Real-time tumour-tracking radiotherapy," Lancet **353**, 1331-1332 (1999).

58 H. Shirato, S. Shimizu, T. Kunieda, K. Kitamura, M. van Herk, K. Kagei, T. Nishioka, S. Hashimoto, K. Fujita, H. Aoyama, "Physical aspects of a real-time tumor-tracking system for gated radiotherapy," International Journal of Radiation Oncology Biology Physics **48**, 1187-1196 (2000).

59 H. Shirato, T. Harada, T. Harabayashi, K. Hida, H. Endo, K. Kitamura, R. Onimaru, K. Yamazaki, N. Kurauchi, T. Shimizu, "Feasibility of insertion/implantation of 2.0-mm-diameter gold internal fiducial markers for precise setup and real-time tumor tracking in radiotherapy," International Journal of Radiation Oncology* Biology* Physics **56**, 240-247 (2003).

60 S. Shimizu, H. Shirato, S. Ogura, H. Akita-Dosaka, K. Kitamura, T. Nishioka, K. Kagei, M. Nishimura, K. Miyasaka, "Detection of lung tumor movement in real-time tumor-tracking radiotherapy* 1," International Journal of Radiation Oncology* Biology* Physics **51**, 304-310 (2001).

61 T. Harada, H. Shirato, S. Ogura, S. Oizumi, K. Yamazaki, S. Shimizu, R. Onimaru, K. Miyasaka, M. Nishimura, H. Dosaka-Akita, "Real-time tumor-tracking radiation therapy for lung carcinoma by the aid of insertion of a gold marker using bronchofiberscopy," Cancer **95**, 1720-1727 (2002).

62 F. Laurent, V. Latrabe, B. Vergier, M. Montaudon, J.M. VERNEJOUX, J. Dubrez, "CT-guided transthoracic needle biopsy of pulmonary nodules smaller than 20 mm: results with an automated 20-gauge coaxial cutting needle," Clin. Radiol. **55**, 281-287 (2000).

63 S. Arslan, A. Yilmaz, B. Bayramgurler, O. Uzman, E. Nver, E. Akkaya, "CT- guided transthoracic fine needle aspiration of pulmonary lesions: accuracy and complications in 294 patients," Med. Sci. Monit. **8**, CR493-7 (2002).

64 P.R. Geraghty, S.T. Kee, G. McFarlane, M.K. Razavi, D.Y. Sze, M.D. Dake, "CT-guided Transthoracic Needle Aspiration Biopsy of Pulmonary Nodules: Needle Size and Pneumothorax Rate1," Radiology **229**, 475 (2003).

65 U. TOPAL and B. Ediz, "Transthoracic needle biopsy: factors effecting risk of pneumothorax," Eur. J. Radiol. **48**, 263-267 (2003).

66 S. Yousefi, B.T. Collins, C.A. Reichner, E.D. Anderson, C. Jamis-Dow, G. Gagnon, S. Malik, B. Marshall, T. Chang, F. Banovac, "Complications of Thoracic Computed Tomography–Guided Fiducial Placement for the Purpose of Stereotactic Body Radiation Therapy," Clinical Lung Cancer **8**, 252-256 (2007).

67 N. Kothary, J.J. Heit, J.D. Louie, W.T. Kuo, B.W. Loo Jr, A. Koong, D.T. Chang, D. Hovsepian, D.Y. Sze, L.V. Hofmann, "Safety and Efficacy of Percutaneous Fiducial Marker Implantation for Image-guided Radiation Therapy," Journal of Vascular and Interventional Radiology **20**, 235-239 (2009).

68 N. Bhagat, N. Fidelman, J.C. Durack, J. Collins, R.L. Gordon, J.M. LaBerge, R.K. Kerlan Jr, "Complications associated with the percutaneous insertion of fiducial markers in the thorax," Cardiovasc. Intervent. Radiol. **33**, 1186-1191 (2010).

69 K. Kitamura, H. Shirato, S. Shimizu, N. Shinohara, T. Harabayashi, T. Shimizu, Y. Kodama, H. Endo, R. Onimaru, S. Nishioka, H. Aoyama, K. Tsuchiya, K. Miyasaka, "Registration accuracy and possible migration of internal fiducial gold marker implanted in prostate and liver treated with real-time tumor-tracking radiation therapy (RTRT)," Radiotherapy and Oncology **62**, 275-281 (2002).

70 E. Kanoulas, J.A. Aslam, G.C. Sharp, R.I. Berbeco, S. Nishioka, H. Shirato, S.B. Jiang, "Derivation of the tumor position from external respiratory surrogates with periodical updating of the internal/external correlation." Phys. Med. Biol. **52**, 5443-5456 (2007).

71 B. Cho, P.R. Poulsen, P.J. Keall, "Real-time tumor tracking using sequential kV imaging combined with respiratory monitoring: a general framework applicable to commonly used IGRT systems," Phys. Med. Biol. **55**, 3299 (2010).

72 L.I. Cerviño, A.K.Y. Chao, A. Sandhu, S.B. Jiang, "The diaphragm as an anatomic surrogate for lung tumor motion," Phys. Med. Biol. **54**, 3529 (2009).

73 L.I. Cerviño, Y. Jiang, A. Sandhu, S.B. Jiang, "Tumor motion prediction with the diaphragm as a surrogate: a feasibility study," Phys. Med. Biol. **55**, N221 (2010).

74 L. van der Weide, van Sörnsen de Koste, J.R., F.J. Lagerwaard, A. Vincent, B. van Triest, B.J. Slotman, S. Senan, "Analysis of carina position as surrogate marker for delivering phase-gated radiotherapy," Int. J. Radiat. Oncol. Biol. Phys. (2007).

75 F.O.B. Spoelstra, D.E.K. VAN SÖRNSEN, R. John, A. VINCENT, J.P. CUIJPERS, B.J. SLOTMAN, S. SENAN, "An evaluation of two internal surrogates for determining the three-dimensional position of peripheral lung tumors," Int. J. Radiat. Oncol. Biol. Phys. **74**, 623-629 (2009).

76 T. Lin, L. Cervio, X. Tang, N. Vasconcelos, S. Jiang, "Fluoroscopic tumor tracking for image-guided lung cancer radiotherapy." Phys. Med. Biol. **54**, 981-992 (2009).

77 S.S. Vedam, P.J. Keall, V.R. Kini, H. Mostafavi, H.P. Shukla, R. Mohan, "Acquiring a four-dimensional computed tomography dataset using an external respiratory signal." Phys. Med. Biol. **48**, 45-62 (2003).

78 D. Low, M. Nystrom, E. Kalinin, P. Parikh, J. Dempsey, J. Bradley, S. Mutic, S. Wahab, T. Islam, G. Christensen, D. Politte, B. Whiting, "A method for the reconstruction of four-dimensional synchronized CT scans acquired during free breathing." Med. Phys. **30**, 1254-1263 (2003).

79 T. Pan, T. Lee, E. Rietzel, G.T.Y. Chen, "4D-CT imaging of a volume influenced by respiratory motion on multi-slice CT." Med. Phys. **31**, 333-340 (2004).

80 J. Sonke, L. Zijp, P. Remeijer, M. van Herk, "Respiratory correlated cone beam CT." Med. Phys. **32**, 1176-1186 (2005).

81 L. Zijp, J. Sonke, M.v. Herk, "Extraction of the respiratory signal from sequential thorax cone-beam X-ray images," presented at International Conference on the Use of Computers in Radiation Therapy.

82 J. Blackall, S. Ahmad, M. Miquel, J. McClelland, D. Landau, D. Hawkes, "MRI-based measurements of respiratory motion variability and assessment of imaging strategies for radiotherapy planning," Phys. Med. Biol. **51**, 4147 (2006).

83 Y. Cui, J. Dy, G. Sharp, B. Alexander, S. Jiang, "Multiple template-based fluoroscopic tracking of lung tumor mass without implanted fiducial markers." Phys. Med. Biol. **52**, 6229-6242 (2007).

84 Q. Xu, R.J. Hamilton, R.A. Schowengerdt, B. Alexander, S.B. Jiang, "Lung tumor tracking in fluoroscopic video based on optical flow," Med. Phys. **35**, 5351 (2008).

85 Q. Xu, R.J. Hamilton, R.A. Schowengerdt, S.B. Jiang, "A deformable lung tumor tracking method in fluoroscopic video using active shape models: a feasibility study," Phys. Med. Biol. **52**, 5277 (2007).

86 R.I. Berbeco, H. Mostafavi, G.C. Sharp, S.B. Jiang, "Towards fluoroscopic respiratory gating for lung tumours without radiopaque markers," Phys. Med. Biol. **50**, 4481 (2005).

87 Y. Cui, J.G. Dy, B. Alexander, S.B. Jiang, "Fluoroscopic gating without implanted fiducial markers for lung cancer radiotherapy based on support vector machines," Phys. Med. Biol. **53**, N315 (2008).

88 R. Li, J.H. Lewis, L.I. Cerviño, S.B. Jiang, "A feasibility study of markerless fluoroscopic gating for lung cancer radiotherapy using 4DCT templates," Phys. Med. Biol. **54**, N489 (2009).

89 R. Zeng, J. Fessler, J. Balter, "Respiratory motion estimation from slowly rotating x-ray projections: theory and simulation." Med. Phys. **32**, 984-991 (2005).

90 ---. "Estimating 3-D respiratory motion from orbiting views by tomographic image registration." IEEE Trans. Med. Imaging **26**, 153-163 (2007).

91 A. Docef and M.J. Murphy, "Reconstruction of 4D deformed CT for moving anatomy," International Journal of Computer Assisted Radiology and Surgery **3**, 591-598 (2008).

92 R. Li, X. Jia, J. Lewis, X. Gu, M. Folkerts, C. Men, S. Jiang, "Real-time volumetric image reconstruction and 3D tumor localization based on a single x-ray projection image for lung cancer radiotherapy." Med. Phys. **37**, 2822-2826 (2010).

93 Y. Long, J. Fessler, J. Balter, "Accuracy estimation for projection-to-volume targeting during rotational therapy: a feasibility study." Med. Phys. **37**, 2480-2490 (2010).

94 M. Van Herk, L. Zijp, P. Remeijer, J. Wolthaus, J. Sonke, "On-line 4D cone beam CT for daily correction of lung tumour position during hypofractionated radiotherapy," ICCR, Toronto, Canada (2007).

95 H. Yan, X. Wang, W. Yin, T. Pan, M. Ahmad, X. Mou, L. Cerviño, X. Jia, S.B. Jiang, "Extracting respiratory signals from thoracic cone beam CT projections," Phys. Med. Biol. **58**, 1447 (2013).

96 J.H. Lewis, R. Li, W.T. Watkins, J.D. Lawson, W.P. Segars, L.I. Cerviño, W.Y. Song, S.B. Jiang, "Markerless lung tumor tracking and trajectory reconstruction using rotational cone-beam projections: a feasibility study," Phys. Med. Biol. **55**, 2505 (2010).

97 Y. Yang, Z. Zhong, X. Guo, J. Wang, J. Anderson, T. Solberg, W. Mao, "A novel markerless technique to evaluate daily lung tumor motion based on conventional cone-beam CT projection data," International Journal of Radiation Oncology* Biology* Physics **82**, e749-e756 (2012).

98 G.D. Hugo, J. Liang, D. Yan, "Marker-free lung tumor trajectory estimation from a cone beam CT sinogram," Phys. Med. Biol. **55**, 2637 (2010).

99 C. Shieh, P.J. Keall, Z. Kuncic, C. Huang, I. Feain, "Markerless tumor tracking using short kilovoltage imaging arcs for lung image-guided radiotherapy," Physics in medicine & biology **60**, 9437-9454 (2015).

100 S. Chen, P. Poulsen, E. Weiss, P. Keall, G. Hugo, "TU-E-204B-05: Feasibility of Markerless 3D Tumor Trajectory Tracking in CBCT Projections Using Digital Subtraction Method," Med. Phys. **37**, 3402 (2010).

101 A. Bharatha, M. Hirose, N. Hata, S.K. Warfield, M. Ferrant, K.H. Zou, E. Suarez-Santana, J. Ruiz-Alzola, A. D'Amico, R.A. Cormack, R. Kikinis, F.A. Jolesz, C.M. Tempany, "Evaluation of three-dimensional finite element-based deformable registration of pre- and intraoperative prostate imaging," Medical physics. **28**, 2551-2560 (2001).

102 K.K. Brock, D.L. McShan, J.M. Balter, "A comparison of computer-controlled versus manual on-line patient setup adjustment," Journal of applied clinical medical physics **3**, 241-247 (2002).

103 D. Rueckert, L.I. Sonoda, C. Hayes, D.L. Hill, M.O. Leach, D.J. Hawkes, "Nonrigid registration using free-form deformations: application to breast MR images," Medical Imaging, IEEE Transactions on **18**, 712-721 (1999).

104 E. Schreibmann, G.T.Y. Chen, L. Xing, "Image interpolation in 4D CT using a BSpline deformable registration model," International journal of radiation oncology, biology, physics. **64**, 1537-1550 (2006).

105 F. Bookstein, "Thin-Plate Splines and the decomposition of deformation," IEEE Trans.Patt.Anal.Mach.Intell **10** (1988).

106 J. Lian, L. Xing, S. Hunjan, C. Dumoulin, J. Levin, A. Lo, R. Watkins, K. Rohling, R. Giaquinto, D. Kim, "Mapping of the prostate in endorectal coil-based MRI/MRSI and CT: a deformable registration and validation study," Med. Phys. **31**, 3087-3094 (2004).

107 T. Guerrero, G. Zhang, T. Huang, K. Lin, "Intrathoracic tumour motion estimation from CT imaging using the 3D optical flow methodPresented at The IASTED Second International Conference on Biomedical Engineering (BioMED 2004), Innsbruck, Austria, 16–18 February 2004." Phys. Med. Biol. **49**, 4147 (2004).

108 G.S. Mageras, A. Pevsner, E.D. Yorke, K.E. Rosenzweig, E.C. Ford, A. Hertanto, S.M. Larson, D.M. Lovelock, Y.E. Erdi, S.A. Nehmeh, "Measurement of lung tumor motion using respiration-correlated CT," International Journal of Radiation Oncology* Biology* Physics **60**, 933-941 (2004).

109 S. Klein, M. Staring, K. Murphy, M.A. Viergever, J.P. Pluim, "Elastix: a toolbox for intensity-based medical image registration," Medical Imaging, IEEE Transactions on **29**, 196-205 (2010).

110 D.P. Shamonin, E.E. Bron, B.P. Lelieveldt, M. Smits, S. Klein, M. Staring, Alzheimer's Disease Neuroimaging Initiative, "Fast parallel image registration on CPU and GPU for diagnostic classification of Alzheimer's disease," Frontiers in neuroinformatics **7** (2013).

111 P.R. Poulsen, W. Fledelius, P.J. Keall, E. Weiss, J. Lu, E. Brackbill, G.D. Hugo, "A method for robust segmentation of arbitrarily shaped radiopaque structures in cone-beam CT projections," Med. Phys. **38**, 2151 (2011).

112 H. Shirato, K. Suzuki, G.C. Sharp, K. Fujita, R. Onimaru, M. Fujino, N. Kato, Y. Osaka, R. Kinoshita, H. Taguchi, S. Onodera, K. Miyasaka, "Speed and amplitude of lung tumor motion precisely detected in four-dimensional setup and in real-time tumor-tracking radiotherapy," International journal of radiation oncology, biology, physics. **64**, 1229-1236 (2006).

113 R. Brunelli and T. Poggiot, "Template matching: Matched spatial filters and beyond," Pattern Recognit **30**, 751-768 (1997).

114 R. Brunelli, *Template Matching Techniques in Computer Vision: Theory and Practice* (Wiley, 2009).

115 A. Fitch, A. Kadyrov, W.J. Christmas, J. Kittler, "Orientation correlation," presented at British Machine Vision Conference.

116 Y. Cui, J. Dy, G. Sharp, B. Alexander, S. Jiang, "Robust fluoroscopic respiratory gating for lung cancer radiotherapy without implanted fiducial markers." Phys. Med. Biol. **52**, 741-755 (2007).

117 R. Li, J. Lewis, L. Cervio, S. Jiang, "A feasibility study of markerless fluoroscopic gating for lung cancer radiotherapy using 4DCT templates." Phys. Med. Biol. **54**, N489-N500 (2009).

118 P. Poulsen, B. Cho, K. Langen, P. Kupelian, P. Keall, "Three-dimensional prostate position estimation with a single x-ray imager utilizing the spatial probability density." Phys. Med. Biol. **53**, 4331-4353 (2008).

Development and Evaluation of Framework for Validating Image-based Target Tracking Algorithms using Implanted Markers

Shufei Chen[1], Elisabeth Weiss[1], Nick Roman[1], Walther Fledelius[2], Per Poulsen[2], Paul J. Keall[3], and Geoffrey D. Hugo[1]

[1]Department of Radiation Oncology, Virginia Commonwealth University, Richmond, Virginia 23298

[2]Department of Oncology, Aarhus University Hospital, Nr Brogade 44, 8000 Aarhus C, Denmark

[3]Radition Physics Laboratory, The University of Sydney, NSW 2006, Australia

Keywords: template-matching, tumor motion, lung cancer, markerless tracking

Corresponding Author

Geoffrey D. Hugo, Ph.D.
Department of Radiation Oncology
Virginia Commonwealth University
401 College Street
PO Box 980058
Richmond, VA 23298
Telephone: 804-628-3457
Fax: 804-628-0271
E-mail: gdhugo@vcu.edu

ABSTRACT

Purpose: To develop and evaluate a validation framework for image-based markerless target tracking algorithms.

Methods: Fiducial markers were implanted inside or near the gross tumor volume in six locally-advanced lung cancer patients, who underwent planning 4D fan beam CT and repeat 4D cone beam CT. The 3D marker trajectories were reconstructed from CBCT projections to quantify tumor motion during scan acquisition. The tumor was delineated in a subset of the reconstructed 4D CBCT scans. A correction based on the tumor-to-marker displacement (TMD) was applied to the marker trajectory to generate the reference tumor trajectory. The variability of the TMD over the treatment course was measured, and the uncertainty of the entire validation framework was estimated.

Results: The uncertainties of the TMD were 0.2/1.0/1.7 mm, for the left-right/anterior-posterior/superior-posterior directions, respectively, for delineated CBCTs. Using linear models to fit undelineated CBCTs, the uncertainties of the TMD were 1.2/1.1/2.1 mm.

Conclusions: The framework of marker-based delineation-free validation method was demonstrated to be an accurate method to estimate tumor centroid positions and hence could be used to validate image-based markerless target tracking algorithms.

I. INTRODUCTION

Algorithms to locate lung tumors directly in sequential 2-dimensional (2D+*t*) data sets such as cone beam CT (CBCT) projections or fluoroscopy are in active development, but a method to validate them in clinical data other than phantom studies is lacking. Instead, some validation studies[1] rely on manual segmentation of the target in 2D images, which is limited to comparisons in small datasets by the time-consuming nature of the segmentation. Other studies compare the result of the markerless tracking

algorithm to an average target trajectory from 4-dimensional (4D) CBCT[2,3], which does not allow for evaluation of the quality of the tracking on short time scales and in response to cycle-to-cycle variation. Fiducial markers implanted near or inside the tumor may provide a 3-dimensional (3D) reference tumor trajectory throughout the whole CBCT scan. However, lung tumors often change shape and volume during therapy, which may impact the utility of the fiducial markers as a long-term surrogate for tumor position and trajectory. We propose to calibrate the fiducial marker trajectory to the tumor position using a combination of 2D+*t* and 4D image data. The purpose of this study is to develop and evaluate a marker-based validation framework to estimate the position of the tumor in 2D+*t* data sets for validation of registration or tracking algorithms.

II. METHOD

II.A. Patient Data

Under an institutional review board-approved protocol and after providing informed consent, 2-3 fiducial markers (Visicoil, RadioMed Corporation, Tyngsboro, Massachusetts) were implanted bronchoscopically in or near the tumor prior to simulation for 6 lung cancer patients set to undergo conventionally-fractionated radiation therapy. All patients were treated with 3D conformal RT (62.6-70 Gy) with standard fractionation (1.8-2 Gy, five days per week). 4D CBCT was acquired daily for each fraction of the treatment for each patient. The gross tumor volume and any implanted fiducial markers were contoured by a physician on each phase of a 4D planning fan beam CT (4D FBCT) and several (generally weekly) 4D CBCT for all the 6 patients.

II.B. Validation Framework

The validation framework is designed to benchmark image-based markerless tracking algorithms which perform rigid measurement of tumor position, since tumor deformation during free breathing is assumed to be small. Based on this assumption, the tumor position during free breathing acquisition of a single CBCT is well-described by measurement of the tumor centroid. Therefore, a marker implanted near the

tumor centroid should describe the instantaneous translational motion of the tumor centroid, provided the offset between the tumor centroid and marker positions is known. However, day-to-day changes in shape and volume of the tumor will cause this offset, which we term the tumor to marker displacement (TMD), to vary on a day to day basis. The basic structure of the validation framework is to use the implanted marker trajectory to represent the tumor trajectory during a single CBCT scan. Then, the TMD is measured from the delineated tumor and markers on the reconstructed 4DCBCT images. The TMD over several fractions is then fit to a model to estimate residual uncertainty (i.e., tumor delineation and other factors) and enable TMD estimation for undelineated CBCT scans.

The implanted markers are segmented in each 2D projection of a CBCT scan using a template-matching algorithm[4], which results in the full 2D marker trajectory throughout the CBCT scan. A maximum likelihood estimation algorithm[5] is applied to estimate the instantaneous 3D position of each marker (denoted as $\vec{m}_p$, where $p \in (0,1,2,3,\cdots)$ is the projection index) in each projection during a CBCT scan. A single marker identified as closest to the tumor centroid on the planning CT is chosen to reconstruct the reference tumor trajectory when there are more than one marker detected in the projection images. Tumor centroid positions differ from the marker positions. Corrections needs to be applied to the known 3D+*t* marker trajectory $\vec{m}_p$ on a set of projections in order to obtain the reference 3D+*t* tumor trajectory (denoted as $\vec{t}_p$) of the same projections. Assuming TMD is constant in the domain of θ, the definition is:

$$TMD(\theta) = \vec{T}(\theta) - \vec{M}(\theta) \quad \textbf{(1)}$$

where θ is the collection of projections used for calculation, $\vec{T}$ is the mean tumor position and $\vec{M}$ is the mean marker position in the domain of θ. The reference $\vec{t}_p$ is then calculated from:

$$\vec{t}_p = \mathrm{TMD}(\theta) + \vec{m}_p \quad \textbf{(2)}$$

TMD needs to be computed daily because it varies interfractionally, up to 1.0 cm difference, as stated in Roman et al [6]. For the delineated CBCTs, $\vec{T}$ is estimated from the centroid of the delineated tumor contour (denoted as $\vec{T}_c$). $\vec{M}$ is calculated from the directly segmented marker trajectory $\vec{m}_p$, denoted as $\vec{M}_s$. Substituting $\vec{T}_c$ and $\vec{M}_s$ in equation (1) will produce TMDs for the delineated scans (denoted as TMD_c). For the non-delineated daily CBCT scans, one approach to calculate the TMD was from a linear model created from the known TMD in the delineated weekly CBCTs, assuming a slow, continuous change of the TMD due to slow, continuous change in tumor volume and shape during therapy. Given all the known TMD_c with the scan days denoted as D (the scan day of the planning CT is considered as day 1), TMD_{in} is calculated using the linear regression method with least square difference criterion from the known data:

$$TMD_{in} = \boldsymbol{\alpha} + \boldsymbol{\beta} d \quad \textbf{(3)}$$

where d is the scan day of the CBCT relative to the planning CT(day 1), $\boldsymbol{\alpha}$ and $\boldsymbol{\beta}$ are variables computed from the minimization of the sum of squared residuals.

II.C. Framework Uncertainties

The total uncertainty of using markers to estimate tumor positions includes the uncertainty of the estimation of 3D positions of the markers from 2D segmentations (σ_{seg}), the intrafractional uncertainty of tumor-to-marker displacement (σ_{intra}), the interfractional variation of tumor-to-marker displacement (σ_{inter}) for non-delineated CBCT scans, and the observer variability in tumor and marker delineation in the 4D CT scans. Based on the method of framework construction, this observer variability is already included in the variabilities σ_{intra} and σ_{inter}. The uncertainty of the estimated 3D marker positions is obtained from study Poulsen et al.[5], as the same implementation was used. At the image frequency of 4D CBCT, σ_{seg} is 0.4/0.4/0.4 mm at left-right (LR)/anterior-posterior (AP)/ superior-inferior (SI) directions

respectively [7]. To estimate the value of σ_{intra}, the tumor-to-marker displacements are calculated for each phase of each delineated 4D CBCT scan. As a measure of intrafractional variability between the tumor and markers, the standard deviation of the tumor-to-marker displacements over the 10 phases is calculated for each scan of each patient, and σ_{intra} is calculated as the root-mean-square of the standard deviations.

The value of the interfractional variation σ_{inter} for non-delineated CBCT scans was estimated from the residual errors of TMD_{in} as follows: The difference between TMD_{in} and the measured displacement TMD_c was calculated in each delineated CBCT and defined as the residual error. The root mean square of the residual errors (RMSE) was calculated as a measure of σ_{inter}. The total uncertainty of the validation framework (σ) was calculated using the equation below:

$$\sigma = \sqrt{\sigma_{seg}^2 + \sigma_{intra}^2 + \sigma_{inter}^2} \quad \textbf{(4)}$$

III. RESULT

The standard deviation (SD) of intrafractional TMD of each patient was shown in Table 1 and σ_{intra} was 1.5 mm at SI direction. The SD at LR and AP directions are close to 0.0 mm.

TMD_c were calculated for the planning CT and all delineated CBCT scans for all 6 patients, and their SI portion are plotted in Figure 1. The root mean square of the residual errors (RMSE) of TMD_{in} is calculated for each patient and shown in Table 2. The interfractional uncertainty of tumor-to-marker displacement (σ_{inter}) for non-delineated CBCT scans is 1.2/1.3/2.0 mm at LR/AP/SI directions correspondingly. Therefore, the total uncertainty of the validation framework (σ) was estimated to be 0.2/1.0/1.7 mm from the calculation using equation (4) for delineated CBCT scans and 1.2/1.6/2.6 mm for non-delineated scans at LR/AP/SI directions correspondingly.

The validation framework was tested in the second weekly CBCT scan of patient 1 as an example. The trajectory obtained from a markerless tracking algorithm[2] was compared against the reference trajectory $\vec{t}_p$. The markers were removed from the projection images using an in-painting technique so as not to

bias the markerless algorithm. The trajectories comparison at the SI direction is shown in Figure 2. The error was defined as the difference between the markerless trajectory and the reference trajectory from the validation framework. The mean absolute error was 1.7 mm with the standard deviation 1.6 mm and 90% error level was 3.3 mm.

IV. DISCUSSION

The marker-based validation framework, which employs TMD as the correction factor to generate reference tumor trajectory for the markerless tumor tracking algorithm, has an uncertainty less than 2 mm if the CBCT is delineated. Ideally, every CBCT should be delineated. But our study shows that, if the CBCT are delineated weekly, the validation framework still has promising accuracy, less than 3 mm. The intrafraction variability in TMD was 1.5 mm in the SI direction and negligible in other directions, supporting our assumption of minimal deformation of the tumor to marker configuration during free breathing. In the calculation of TMD, the marker trajectories estimated directly from the projections are used to compute mean marker position rather than the marker contours in the delineated CBCTs. One reason is that markers close to each other may not be distinguishable from each other in the reconstructed CBCT, resulting in one contour for more than one marker. The other concern is that the volume average effect is more severe for small objects like markers resulting larger delineation uncertainty, thus the higher spatial resolution of the projection images is preferred. In the computation of the linear function to calculate TMD for non-delineated CBCT scans, the planning CT was not taken into account in the model. As shown in Figure 1, the TMD in the planning CT lies far away from the linear curve especially for patients 4, 5 and 6. This result could be due to actual changes in tumor volume or shape, marker migration in the generally two weeks between planning and treatment, or differences in observer variability due to different image quality between 4DCBCT and 4D fan beam CT. In one patient, patient 6, marker migration happens and the marker existed at the first five weekly CBCT disappeared at the sixth weekly CBCT. Because of the migration, the TMD at the fifth week is drifted away from the linear model, and it is considered as the outlier as shown in Table 2 and Figure 1(f). If the outlier is not

removed from the linear model, the residual errors are fairly large which are 1.0/3.0/3.7 mm in the LR/AP/SI directions respectively. In this case, σ_{inter} is reduced to 1.2/0.5/1.3 mm as shown in the brackets in Table 2 and consequentially σ is reduced to 1.2/1.1/2.1 mm.

In the calculation of the resultant TMDs and the uncertainties, our results are based on the assumption that the physician delineation is the ground truth. However, the delineation itself introduces uncertainties into the framework, which manifests as an increase in σ. In this study, the patients are delineated by one physician, so inter-observer variability is not considered. Ideally, the intra-observer variation of tumor delineation could be separately quantified to enable calculation of the variability due to the TMD component alone. However, we did not separate the intra-observer variation from the inter- and intra-fractional variation due to the overall small magnitude of the total variability.

V. CONCLUSION

A framework of using implanted marker and a combination of 2D+*t* and 4D imaging for the validation of image-based lung tumor tracking algorithms was developed. The estimated uncertainty of the validation framework is 2-3 mm, depending on whether the tumor is delineated in the 4DCBCT scan or its position is interpolated from delineated scans. In conclusion, the framework of marker-based validation method is demonstrated to be an accurate method to estimate tumor centroid positions and hence can serve as the validation method for image-based target tracking algorithms.

Table 1. Intrafractional standard deviation of TMD for all delineated 4D CBCT scans, SI direction for each patient.

Patient	Intrafraction standard deviation of TMD (mm)						
	1	2	3	4	5	6	7
1	0.7	1.3	0.6	1.1	1.0	0.8	1.0
2	0.7	0.5	0.8	0.9	0.5	--	--
3	1.2	0.8	0.9	1.0	0.8	0.4	--
4	2.1	2.5	1.3	2.6	1.7	1.3	1.2
5	1.8	0.9	1.2	0.7	0.9	1.0	--
6	4.0	2.1	2.0	1.4	2.0	--	--
Total (σ_{intra})	1.5						

Table 2. RMSE of Linear Model.

Patient	RMSE (mm)		
	LR	AP	SI
1	0.5	0.3	0.7
2	1.3	0.6	1.9
3	2.3	0.3	1.6
4	0.9	0.6	1.3
5	0.3	0.6	1.3
6	0.8 (1.0*)	0.4 (3.0*)	0.4 (3.7*)
Total (σ_{inter})	1.2 (1.2*)	0.5 (1.3*)	1.3 (2.0*)

*Results for without ruling out the outlier for patient 4.

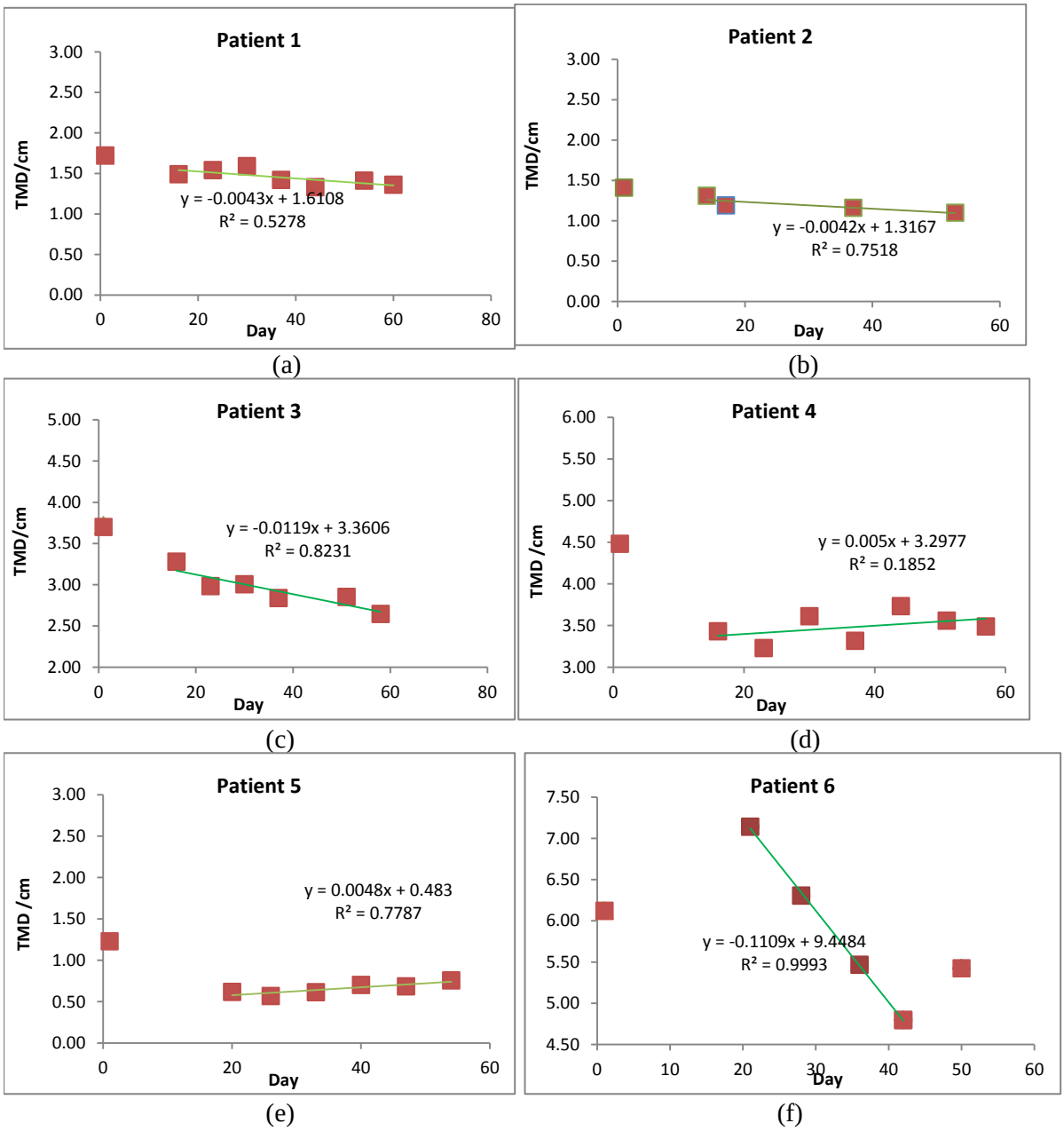

Figure 1 (a) to (f) are the plots of tumor to marker displacement as a function of time for all 6 patients. The red squares are the TMD_c for the planning CT (day 1) and all the delineated CBCTs and the straight line with the equation are the linear fit curve for TMD_{in}.

200

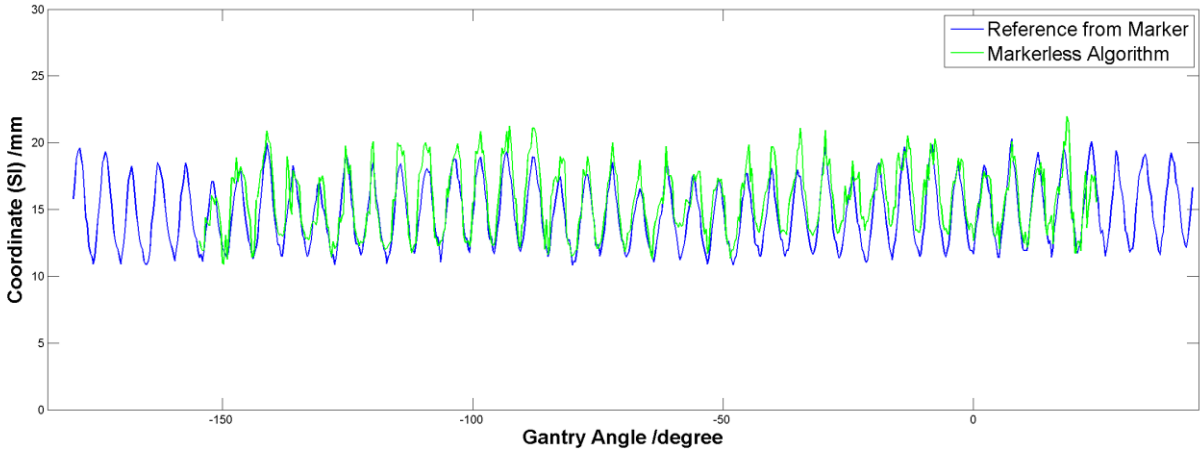

Figure 2. Example comparison of tumor trajectories measured by the validation framework and a test markerless tracking algorithm, superior-inferior (SI) direction over gantry angles -150 º to 30 º.

1 J.H. Lewis, R. Li, W.T. Watkins, J.D. Lawson, W.P. Segars, L.I. Cerviño, W.Y. Song, S.B. Jiang, "Markerless lung tumor tracking and trajectory reconstruction using rotational cone-beam projections: a feasibility study," Phys. Med. Biol. **55**, 2505 (2010).

2 G.D. Hugo, J. Liang, D. Yan, "Marker-free lung tumor trajectory estimation from a cone beam CT sinogram," Phys. Med. Biol. **55**, 2637 (2010).

3 Y. Yang, Z. Zhong, X. Guo, J. Wang, J. Anderson, T. Solberg, W. Mao, "A novel markerless technique to evaluate daily lung tumor motion based on conventional cone-beam CT projection data," International Journal of Radiation Oncology* Biology* Physics **82**, e749-e756 (2012).

4 P.R. Poulsen, W. Fledelius, P.J. Keall, E. Weiss, J. Lu, E. Brackbill, G.D. Hugo, "A method for robust segmentation of arbitrarily shaped radiopaque structures in cone-beam CT projections," Med. Phys. **38**, 2151 (2011).

5 P.R. Poulsen, B. Cho, P.J. Keall, "A method to estimate mean position, motion magnitude, motion correlation, and trajectory of a tumor from cone-beam CT projections for image-guided radiotherapy," Int. J. Radiat. Oncol. Biol. Phys. **72**, 1587-1596 (2008).

6 N.O. Roman, W. Shepherd, N. Mukhopadhyay, G.D. Hugo, E. Weiss, "Interfractional Positional Variability of Fiducial Markers and Primary Tumors in Locally Advanced Non-Small-Cell Lung Cancer During Audiovisual Biofeedback Radiotherapy," International Journal of Radiation Oncology* Biology* Physics **83**, 1566-1572 (2012).

7 P. Poulsen, B. Cho, K. Langen, P. Kupelian, P. Keall, "Three-dimensional prostate position estimation with a single x-ray imager utilizing the spatial probability density." Phys. Med. Biol. **53**, 4331-4353 (2008).

Optimizing template matching-based markerless tumor trajectory estimation algorithm in lung cancer patients

Shufei Chen and Geoffrey Hugo

Department of Radiation Oncology, Virginia Commonwealth University, Richmond, Virginia 23298

Keywords: template-matching, tumor trajectory, markerless

ABSTRACT

Purpose: The purpose of this study was to optimize the markerless template matching algorithm for estimation of the 3D tumor trajectory for cone beam CT (CBCT) projections in lung cancer patients.

Methods: Markers were planted in the patients and they were removed from the projection images using Laplacian interpolation. The effectiveness of marker removal was evaluated by a phantom study. Markerless tumor trajectory estimation uses a set of templates generated from forward projecting a region of interest of the planning fan beam CT to match the tumor in the CBCT projections. Three different template methods of registration were compared. One called Ex-GTV template, generated from GTV plus a margin. One generated from the minimum bounding cylinder of expended GTV, called cylinder template. The last template generated from zero padding at the gradient image of the Ex-GTV template, denoted as padded template. Errors of the markerless template-based matching algorithm using each set of template were calculated relative to the tumor position obtained from segmented implanted internal fiducial marker trajectories. Furthermore, a constraint method was implemented to penalize large mis-matches.

Results: Application of marker painting improved the registration by 2 pixels at each coordinate compared against the gold standard. The registration errors (mean absolute error/standard deviation/90% error level [all in mm]) obtained with five patients using the three different template methods were 5.3/6.5/12.4 for the Ex-GTV template, 6.1/6.4/13.3 for the cylinder template, and 3.5/5.0/7.9 for the padded template. The magnitudes of errors were further reduced to 2.1/2.5/4.3 after implementing the constraint method.

Conclusions: The marker removal technique we implemented here successfully reduced the effect of markers on the 2D image registration. The trajectory obtained from using padded template agreed best with the implanted marker trajectories and the constraint method further improved the results.

I. INTRODUCTION

Image guided radiotherapy (IGRT) has the potential to improve targeting by incorporating temporal patient specific geometry information and variations into the adaptive planning process[1-5]. Incorporating variability models into the treatment plan, whether through 4D inverse planning or offline adaptation, requires characterization of an individual patient's motion pattern throughout the treatment course. Because the patient-specific motion model is often built at the simulation stage, it is inadequate to fully represent the situation during treatment delivery due to interfractional geometry variation[6,7]. Therefore, monitoring tumor motion during the treatment or retrospective evaluation of treatment plans is necessary to ensure and evaluate dose delivery. Respiration correlated four-dimensional computed tomography (4DCT) [8-10] is able to provide 3D anatomy at each phase of breathing and the average cycle of respiration induced organ motion. However, the tumor motion is not simply periodic but it suffers from cycle to cycle variation and shift of the mean or exhale tumor position (drift) [11-13]. The average breathing cycle from the 4DCT cannot provide information to estimate cycle-to-cycle variation and drift. Hence, the instantaneous tumor trajectory needs to be measured in order to quantify these variations. Current techniques that are used to track the tumor can be grouped into three categories: tracking external surrogates, tracking with implanted internal fiducial markers, and markerless tracking with internal anatomical features. Although external surrogates require no radiation dose and are generally straightforward to use, the correlation between the tumor location and external surrogate signals varies within a fraction and across treatment days[14-17]. Tracking implanted radiopaque fiducial markers in fluoroscopic images and projection images of CBCT has been pursued by researchers[18-25]. Fiducial markers serve as reliable surrogate to locate or track tumors[21,24]. Marker implantation is invasive, so

physicians and patients are not always willing to use this procedure especially by those expecting a 'non-invasive' treatment modality with radiation therapy.

'Markerless' localization of the tumor mass in fluoroscopic images has been studied for tracking[26-28] and gating[29-31]. Support vector machine-based[30], template-based[26], and optical flow[27] based algorithms were developed for fixed beam angle fluoroscopic detection (no gantry rotation during acquisition). Template-based markerless tumor tracking has been extended to the case of gantry rotation[32-35]. These studies evaluated small, parenchymal lesions such as those amenable to stereotactic body radiotherapy. Here, we extend the template matching approach to larger lesions infiltrating the chest wall, hilum, or mediastinum. We optimize the template shape for these challenging cases, and evaluate a method to penalize large mis-matches.

II. METHOD

II.A. General Description of the Algorithm

A template-based matching algorithm for markerless tumor trajectory estimation (MLTM) was developed previously [32]. The procedure consists of five steps as shown in Figure 1: 1) GTV (in green) was delineated by physicians in the planning 4DCT and it was expanded with a margin to obtain Expanded GTV (Ex-GTV, in purple). 2) Generation of masked CT was by zero padding regions outside Ex-GTV and the masked CT was shifted to the daily tumor position by registering the tumor in the planning CT to the tumor in the daily CBCT, which is denoted as the daily tumor position. 3) The shifted masked CT was forward projected to generate digital reconstructed radiograph (DRR) at each phase and each gantry angle intervals and the DRRs are denoted as tumor template (TT). 4) Crop the TT and perform 2D/2D registration of TT to the measured CBCT projections (MP) by template matching (TM) within a search region of ±4 mm. The red contour is the matching result. 5) Reconstruct 2D positions to generate3D tumor trajectory by backprojection.

The following simple enhancements are added to this basic framework, but are not the main focus of this work:

1) Histogram equalization is applied to the search region in the projection images to improve the contrast.

2) The search window for template matching is adapted to ±22.5 mm, which is ±15 mm in the room coordinates, instead of the ±4 mm window to account for the up to 3 cm tumor motion.

3) The similarity metric used to conduct template matching is changed from block normalized cross correlation (NCC) to a gradient correlation metric termed the Orientation Correlation (OC) [37].

4) A spatial probabilistic method developed by Poulsen et al[36] is used to reconstruct 3D tumor positions from 2D tumor positions other than a simple backprojection in the original framework.

The main adaptions will be introduced in section II.C.

Five patients underwent CBCT imaging on a study approved by the local institutional review board after providing informed consent. The studied patients were implanted with fiducial markers, and the trajectories obtained from those markers were used to validate the markerless algorithm (Appendix I). One CBCT scan acquired early in the treatment course was analyzed to avoid the effect of large shape changes (i.e., tumor response) in this study.

II.B. Marker Removal

The patients were implanted with fiducial Au markers (Visicoil, RadioMed Corporation, Tyngsboro, Massachusetts) which were usually radiopaque and high contrast structures. The extra information introduced by fiducial markers in projection images might influence the 2D image registration. The marker effect should be eliminated in order to obtain markerless tracking results unbiased by markers, as the markers are used in the validation methodology. A marker painting technique, which was replacing the intensity of pixels inside the marker region by the interpolation value of the surrounding region, was implemented and evaluated.

The markers were segmented using a semi-automated algorithm[25] with the output of the marker centroid positions and 3D marker shape models. The 2D binary mask of markers (marker shadow) for each projection of the CBCT was generated by projecting the 3D shape model to the projection plane. The 2D marker shadows were expanded by 2 pixels to ensure coverage of the whole marker

and relocated to the centroid positions of the markers, e.g. Figure 2g. The intensity inside the marker mask was replaced by interpolating the value from surrounding pixels plus added white noise sampled from a Gaussian distribution. We chose a diffusion-based Laplacian interpolation to obtain the interpolation values [38,39].

Marker painting was applied to both phantom and clinical images to see whether the method was effective at marker removal. A phantom study was conducted to determine if the marker painting technique was effective at reducing the influence of markers on the image registration. The phantom used was a lung phantom with a tumor insert inside (QUASAR™ Cedar Lung Tumour Insert, Modus Medical Devices Inc., London, Canada) as shown in Figure 2a, attached to a dynamic motion stage. The phantom images were taken at two different couch positions to conduct rigid image registration (translation only). Five phantom projection images were taken at two couch positions with or without markers at a fixed gantry angle as shown in Figure 2 (b) to (f). At each of the two couch position, we took a projection image of the phantom without attaching any markers and the registration between these two images (Figures 2b and 2d) was considered as the gold standard. We evaluated three registration scenarios: For Scenario 1, an image of the object with markers (Figure 2c) was registered to an image of the shifted object without markers present (Figure 2d). For Scenario 2, images of the object with markers in the same location relative to the object (Figures 2c and 2e) were registered. Finally, for Scenario 3, images of the object with markers in different orientations relative to the object (Figures 2c and 2f) were registered. These three registration scenarios were repeated after marker painting. Registration error was measured in pixels, relative to the result from the gold standard.

II.C. Algorithm Refinement

II.C.1. Template Study

The templates were rectangular to allow usage of the fast Fourier transform (FFT) in the gradient correlation. In the previous study[32], tumor templates were generated from ROI of physician contoured GTV plus a 5/10 mm margin in the planning 4DCT with zero padding outside the ROI,

denoted here as the Expanded GTV (Ex-GTV) template. Artificial boundary that introduced by the zero padding in the generation of masked CT outside the Ex-GTV region in the planning CT is a particularly important issue to resolve for locally-advanced lung cancers compared to small, refined tumor cases. When creating DRR for tumor templates, artificial radiation beams penetrate the tumor. Large tumors attenuate the beams more than the small tumor causing large differences between zero and nonzero paddings. Therefore, three competing template-generation methods were studied in order to resolve this issue.

The first set of template was the Ex-GTV template (Figure 3a). The second set of templates was generated from the minimum bounding cylinder of the ROI (GTV plus a 5/10 mm margin), denoted here as the Cylinder template[33]. The templates generated from this ROI were already rectangular, so no artificial gradient after cropping was present (Figure 3b). An additional approach to avoid the artificial gradient was to only use pixels inside the expanded GTV region to conduct the gradient correlation in the template matching. But this approach is time consuming because it cannot use the FFT in the gradient correlation. Instead, the last set of templates was generated from the Ex-GTV template with some modification in the gradient image. The gradients outside the shape region of the tumor of each template were padded with zero (Padded template). Figure 3d was the zero padded gradient image of Figure 3c, which was gradient image of the Ex-GTV. The Orientation Correlation matched images using correlation, so pixels with zero gradients had no effect on the matching results, and FFT could still be utilized for speed.

II.C.2. Constraint from Training

The search margin in the template matching algorithm was ±15 mm in the global coordinate system. This search region could be constrained since the breathing phase for a given projection was known. The tumor trajectory obtained from a first pass of the template matching algorithm was used as the training data and an average cycle trajectory (mean tumor position of each breathing phase) was generated to guide a second pass of the template registration. The mean position (μ) and standard deviation (σ) of the tumor trajectory, which were obtained from the selected template method

based on the results of the previous section, were calculated. The portion of the trajectory which was within $\mu \pm 2\sigma$ was used to generate the average breathing cycle. The 3D tumor positions chose from the average breathing cycle based on the phase of the projection were forward projected from the global coordinate system to the 2D detector plane to obtain the 2D positions. A 3 mm margin was applied to the *u* direction (across the panel) of the 2D image and a 6 mm margin was applied to the *v* direction (along the panel) to refine the search region of the 2D registration. This margin was obtained from the study of the marker trajectories. The difference between the instantaneous marker positions and the mean marker position of the projection phase for each projection was calculated and analyzed. The margin was chosen from the 95% interval of the differences. The template matching was conducted at the refined search region to obtain the 2D tumor positions.

II.C.3. Evaluation

The resultant tumor trajectories from the markerless estimation were compared to the gold standard which is the tumor trajectory estimated from the marker trajectory. The errors were calculated by the difference between the trajectories of markerless estimation and marker estimation. The mean absolute errors, the standard deviation of the errors, and the 90% error level were calculated.

III. RESULTS

III.A. Marker Removal

Figure 5 shows the clinical CBCT projections with and without marker in-painting. In case 1, the marker was successfully visually removed from a relatively uniform background region. In case 2, the marker is visible over a high contrast structure. After the marker removal, the high contrast boundary beneath the marker region was preserved even though there was some blurring.

Figure 6 shows the CBCT projections of the dynamic phantom with and without marker in-painting. The phantom was scanned at the same setup with and without attached markers. The projection do

not contain markers was considered as the reference which the marker removal results were compare against. The sharp gradient introduced by the marker was successfully removed by the marker removal technique and the profile of the marker removed image was close to the reference profile. For the registration aspect of the phantom study, the registration error for the three scenarios were (-2, 0), (-2, 1) and (-3, 2) pixels correspondingly before marker removal. After applying the marker painting technique, the registration errors were all reduced to (-1, 0).

III.B. Algorithm Refinement

Table 1 shows the errors obtained by employing the Ex-GTV template, the cylinder template, and the padded template as well as the padded template plus the constraint method. Overall, use of the padded template resulted in smaller errors than the other two sets of templates. The padded template was chosen for further study. The results were further improved when the padded template was combined with the constraint method. Figure 4 showed the scatter plots of the tumor SI positions obtained from the markerless template matching method using the three methods of templates, and also from the padded template combined with the constraint method. Ideally, the plotted points should form a straight line; thus, the narrower the width of the distribution is, the more the results agree with the marker estimation. The padded template has the least amount of outliers compared to the other two templates. And the padded template combined with the constraint method further reduces the scatter. These results were consistent with the Table 1 results.

IV. DISCUSSION

Lewis *et al.* [33] developed a phase-binned based algorithm to reconstruct tumor trajectory from the 2D estimation in CBCT projections for lung tumor. This method is able to reconstruct more accurate tumor trajectory from less accurate markerless tracking results. Our study was to improve the accuracy of the markerless tracking instead of improvement by reconstruction. The cylinder template which they used in the study did not work well in our patients, because tumors in our patients were larger lesions infiltrating the chest wall, hilum, or mediastinum. For this kind of tumors,

the bounding cylinder around the GTV plus the margin included more non-tumor-related tissues (different motion pattern with tumor) compared to small well-defined tumors. The extra information degraded the 2D image registration results. The tracking results using the padded template showed better agreement with the reference trajectory from the marker as expected. The padded template had no artificial gradient compared to Ex-GTV template while had better-defined the tumor content compared to cylinder template. Their results were compared against physician contours at the projection images. Physician delineation on each projection is very time-consuming and may be very inaccurate. We employed the marker based validation method from our previous development to validate our algorithms other than the physician contours. The accuracy of the marker-based validation method was studied and the method was independent of the physician delineation.

Yang *et al.* [40] implemented digital subtraction technique in the markerless tumor tracking to remove high contrast overlying structures in the projections. They found that digital subtraction was capable to emphasis tumor visibility in projections so that easier to preform markerless tracking and also easier for physician to delineate. In this study, we focused at improving the template matching aspect of the markerless tracking by constraining the tracking region from training. By shrinking the search region to the most possible region, the template matching was able to avoid the false matching outside the region and find the real best match with a higher possibility. The limitation of the constraint method would be in the case when the tumor motion encounters sharp temporal gradient events (e.g. coughing).

The template matching method worked better for small well-defined tumors. As shown in Table 1, the final results by using the shape template and the constraint method, patients with well-defined solid tumors (Patient 1~3) demonstrated better agreement with the marker estimation. And patients with large and/or diffuse tumors (Patient4, 5), larger errors in both the validation and the tracking were observed. For large tumors, it was found in analysis of 4DCT scans of these patients[41] that the markers were sometimes implanted in clusters in one region of the tumor. Such anisotropic implantation is only a problem for those tumors that deform during breathing, causing the motion of

the markers to diverge from that of the whole tumor. To deal with these issues, multiple template tracking and deformable registration will be tested in future studies.

In this study, the impact of tumor shape change over the course of treatment was not evaluated. As treatment progresses over time, the tumor contours from the planning CT will be less accurate than at the later fractions due to tumor shrinkage. Potential solutions include affine or deformable template matching, which we plan to evaluate in the future.

V. CONCLUSION

Visually, the marker painting using Laplacian interpolation successfully removed the marker from the images and preserved high gradient boundaries with some blurring. The existence of markers in the projection images has influence on the accuracy of the image registration. The Laplacian interpolation method is effective at reducing the effect of markers on the image registration. Out of the three template generation methods, the padded template provides best results and should be used in further studies. With the implement of the constraint method, the results are further improved.

VI. FIGURES

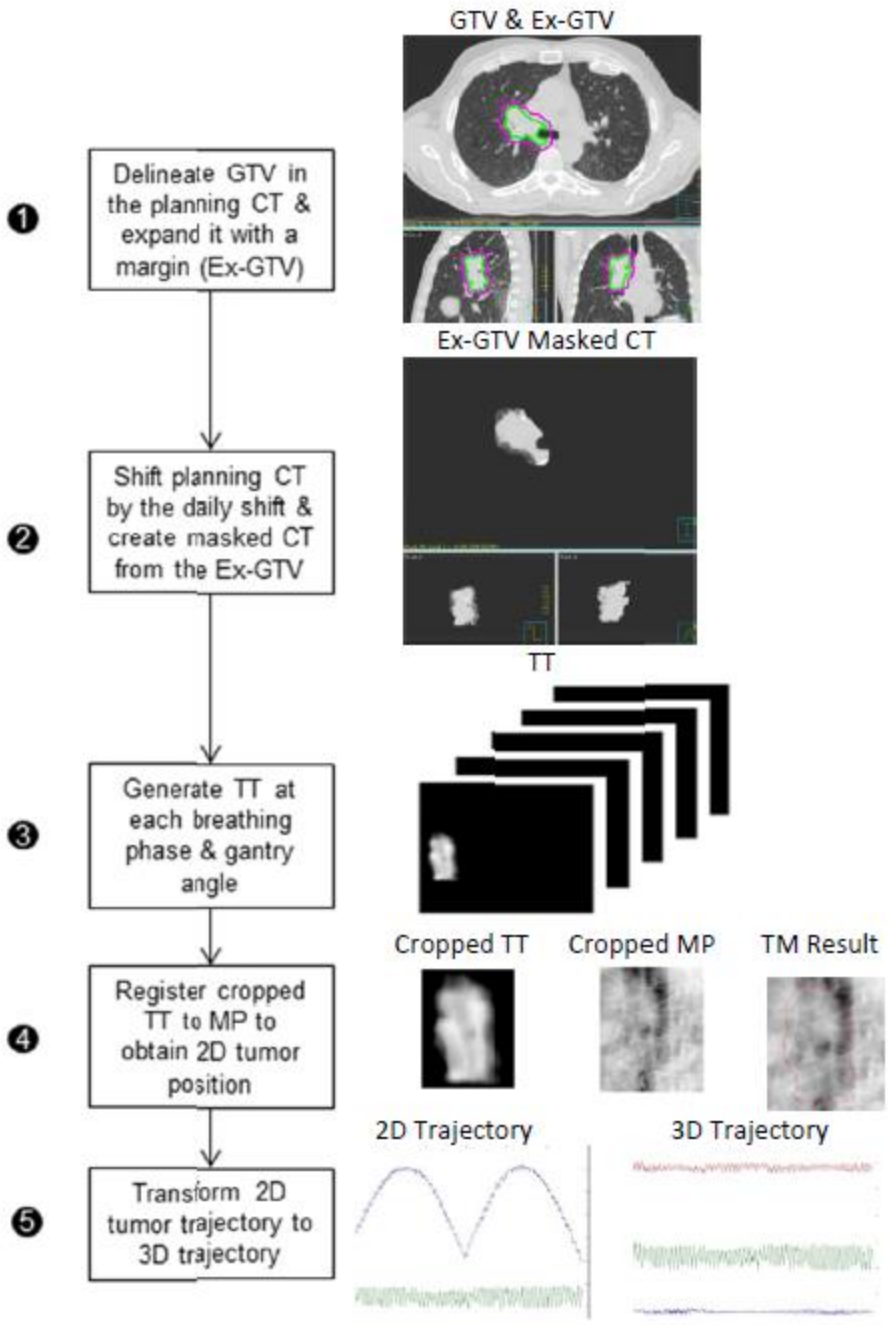

Figure 1. Workflow of the MLTM algorithm for CBCT projections.

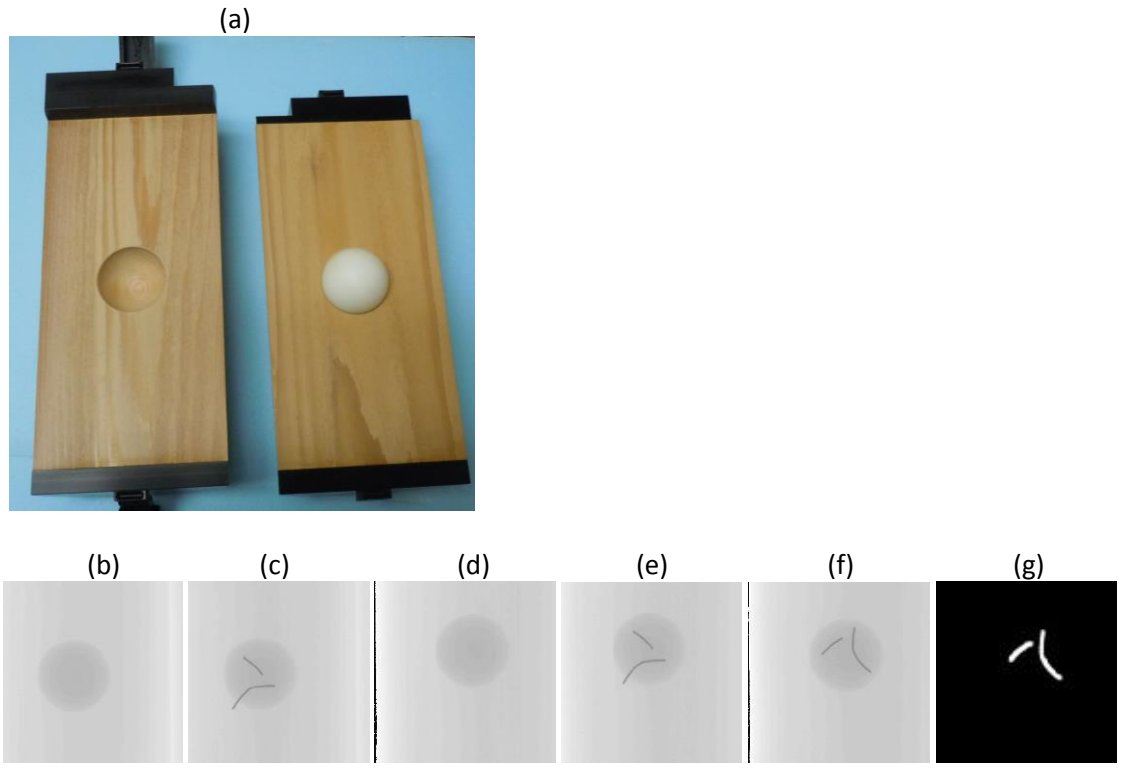

Figure 2. Phantom images. Image (a) lung phantom with the tumor insert; (b) to (f) projection images of the 5 scans. Projections (b) and (c) were scanned at the same setup couch position; projections (d), (e), and (f) were scanned at the same setup position which was shifted 1 cm anterior, inferior and right from scans (b) and (c). Image (g) was the marker masks of projection (f).

270

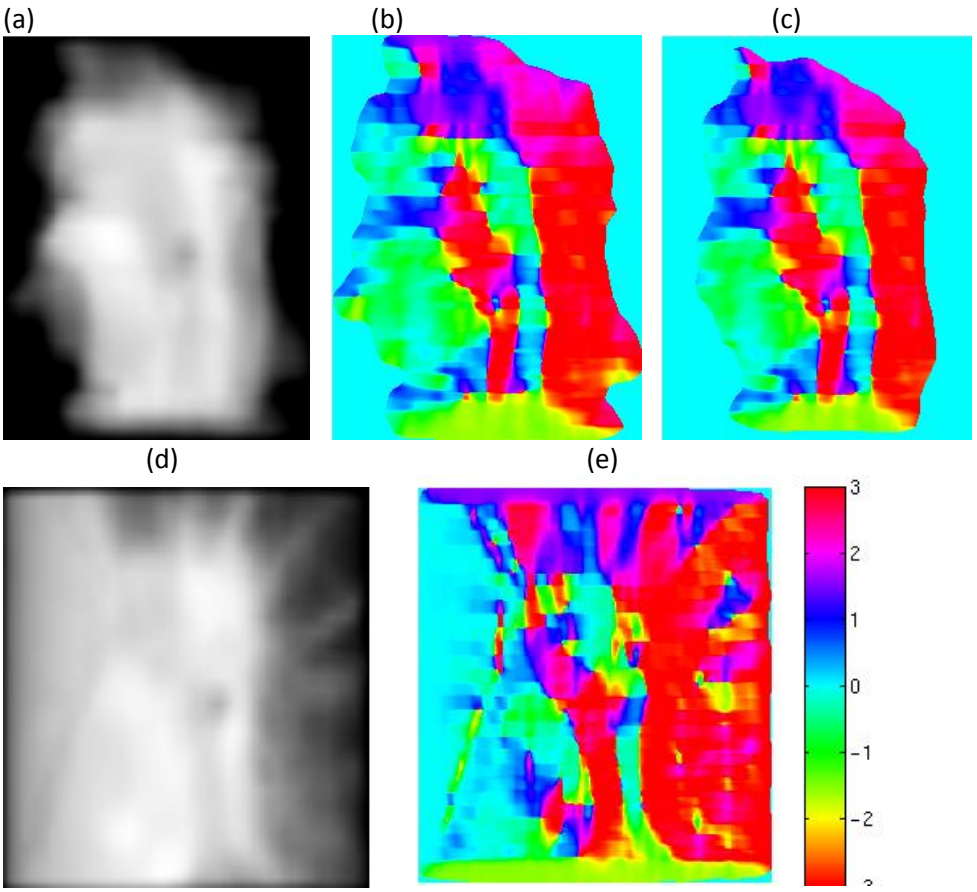

Figure 3. (a) Intensity image of Ex-GTV Template; (b) Gradient image of (a); (c) Gradient image of padded template by zero padding (b) at region outside the threshold; (d) Intensity image of cylinder Template; (e) gradient image of (d).

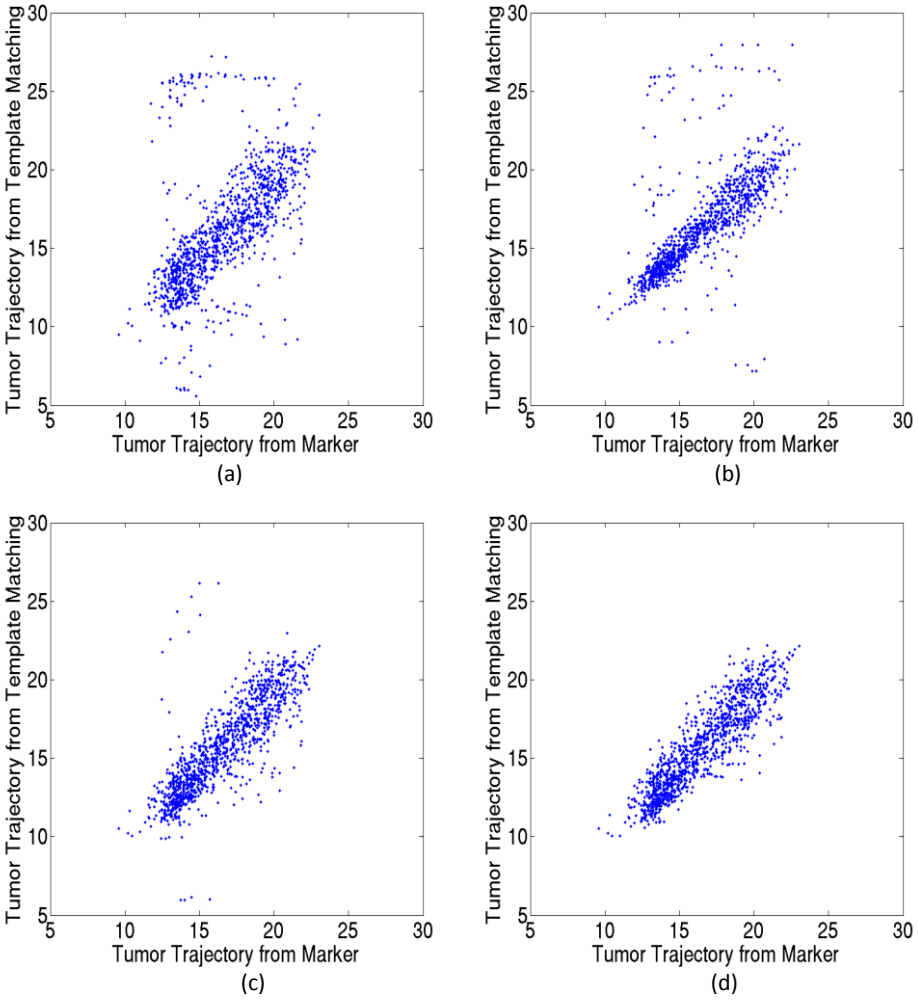

Figure 4. Scatter plots of tumor trajectories obtained from the markerless algorithm versus tumor trajectory from the marker at SI direction in mm. (a) Ex-GTV template; (b) Cylinder template; (c) Padded template; (d) Padded template + constraint method.

.

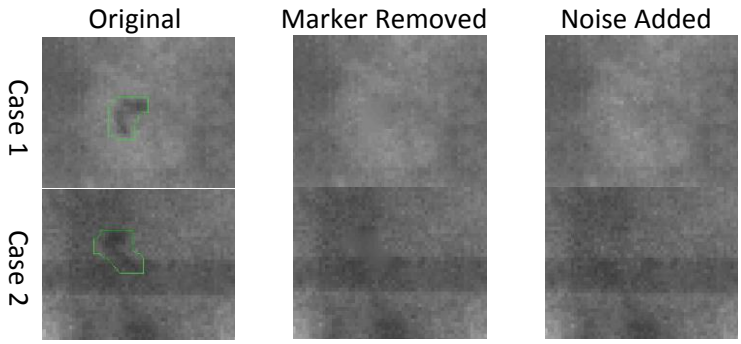

Figure 5. Visual results of marker removal of the clinical cases. The first column was the original projections with the markers contours in green; the second column was the result of marker removed and the third column showed the marker removal results with a Gaussian noise added.

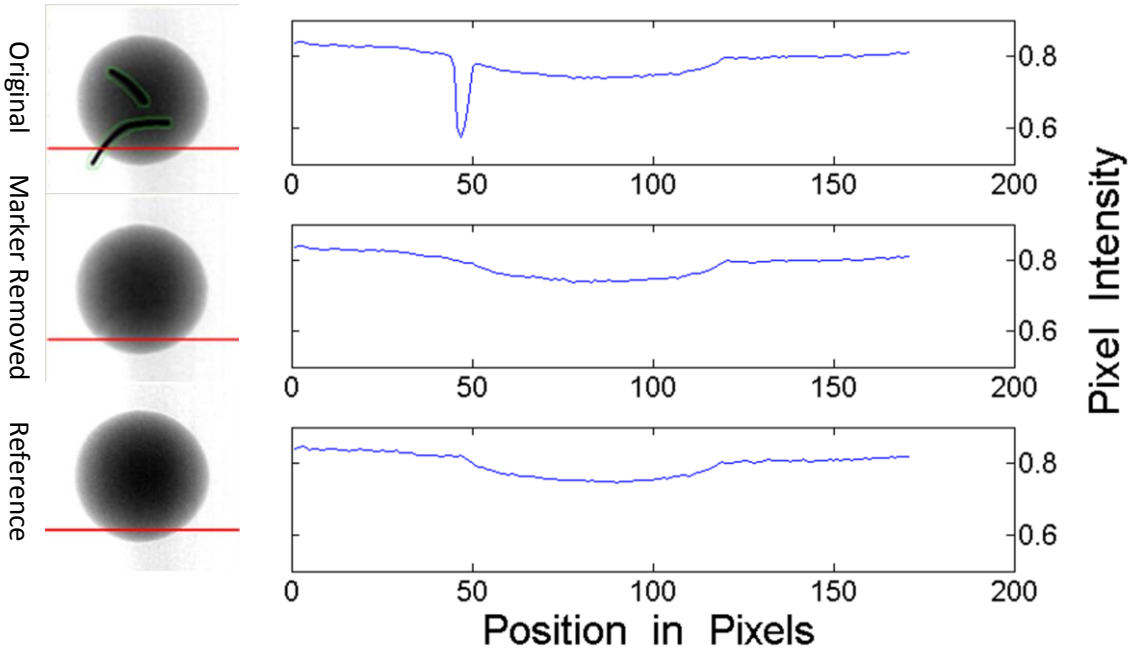

Figure 6. Visual results of marker removal and the comparison of profiles for the phantom case. The first column showed the phantom images and the profiles of the red lines were shown in the second column correspondingly. The first row was from the tumor phantom with the attached markers (green contours); the second row showed the marker removal results of row 1 and they were compared against the reference as shown in row 3.

Method	EX-GTV Template			Cylinder Template			Padded Template			Padded Template + Constraint		
Patient	MAE (mm)	SD (mm)	90% error (mm)	MAE (mm)	SD (mm)	90% error (mm)	MAE (mm)	SD (mm)	90% error (mm)	MAE (mm)	SD (mm)	90% error (mm)
1	3.4	5.6	10.1	3.1	4.5	6.8	2	2.8	3.9	1.7	1.6	3.3
2	8.6	8.5	17.9	6.3	9.0	17.8	3.1	5.3	7.3	1.0	1.3	2.0
3	4.2	5.0	9	6.8	6.8	14.8	3.1	4.3	7.3	2.3	2.6	4.9
4	4.7	6.8	13.8	6.4	3.7	9.7	4.4	6.0	10.7	2.9	3.2	5.9
5	5.6	6.2	11.5	7.9	6.7	17.6	4.7	5.8	10.3	2.7	3.3	5.5
Mean	5.3	6.5	12.4	6.1	6.4	13.3	3.5	5.0	7.9	2.1	2.5	4.3

Table 1. The mean absolute error (MAE), standard deviation (SD), 90% error interval of using each template method and using the constraint method with the selected template method.

1 A. Trofimov, E. Rietzel, H.M. Lu, B. Martin, S. Jiang, G.T.Y. Chen, T. Bortfeld, "Temporo-spatial IMRT optimization: concepts, implementation and initial results," Phys. Med. Biol. **50**, 2779 (2005).

2 D. Yan, F. Vicini, J. Wong, A. Martinez, "Adaptive radiation therapy." Phys. Med. Biol. **42**, 123-132 (1997).

3 D. Yan, D. Lockman, D. Brabbins, L. Tyburski, A. Martinez, "An off-line strategy for constructing a patient-specific planning target volume in adaptive treatment process for prostate cancer." Int. J. Radiat. Oncol. Biol. Phys. **48**, 289-302 (2000).

4 G. Hugo, D. Yan, J. Liang, "Population and patient-specific target margins for 4D adaptive radiotherapy to account for intra- and inter-fraction variation in lung tumour position." Phys. Med. Biol. **52**, 257-274 (2007).

5 D. Yan, "Adaptive radiotherapy: merging principle into clinical practice." Semin. Radiat. Oncol. **20**, 79-83 (2010).

6 G. Hugo, D. Yan, J. Liang, "Population and patient-specific target margins for 4D adaptive radiotherapy to account for intra- and inter-fraction variation in lung tumour position." Phys. Med. Biol. **52**, 257-274 (2007).

7 J.J. Sonke, J. Lebesque, M. van Herk, "Variability of four-dimensional computed tomography patient models," Int. J. Radiat. Oncol. Biol. Phys. **70**, 590-598 (2008).

8 S.S. Vedam, P.J. Keall, V.R. Kini, H. Mostafavi, H.P. Shukla, R. Mohan, "Acquiring a four-dimensional computed tomography dataset using an external respiratory signal." Phys. Med. Biol. **48**, 45-62 (2003).

9 D. Low, M. Nystrom, E. Kalinin, P. Parikh, J. Dempsey, J. Bradley, S. Mutic, S. Wahab, T. Islam, G. Christensen, D. Politte, B. Whiting, "A method for the reconstruction of four-dimensional synchronized CT scans acquired during free breathing." Med. Phys. **30**, 1254-1263 (2003).

10 T. Pan, T. Lee, E. Rietzel, G.T.Y. Chen, "4D-CT imaging of a volume influenced by respiratory motion on multi-slice CT." Med. Phys. **31**, 333-340 (2004).

11 Y. Seppenwoolde, H. Shirato, K. Kitamura, S. Shimizu, M. van Herk, J. Lebesque, K. Miyasaka, "Precise and real-time measurement of 3D tumor motion in lung due to breathing and heartbeat, measured during radiotherapy." Int. J. Radiat. Oncol. Biol. Phys. **53**, 822-834 (2002).

12 G. Hugo, C. Vargas, J. Liang, L. Kestin, J.W. Wong, D. Yan, "Changes in the respiratory pattern during radiotherapy for cancer in the lung," Radiother. Oncol. **78**, 326-331 (2006).

13 J. Blackall, S. Ahmad, M. Miquel, J. McClelland, D. Landau, D. Hawkes, "MRI-based measurements of respiratory motion variability and assessment of imaging strategies for radiotherapy planning," Phys. Med. Biol. **51**, 4147 (2006).

14 D. Ionascu, S. Jiang, S. Nishioka, H. Shirato, R. Berbeco, "Internal-external correlation investigations of respiratory induced motion of lung tumors." Med. Phys. **34**, 3893-3903 (2007).

15 C. OZHASOGLU and M.J. MURPHY, "Issues in respiratory motion compensation during external-beam radiotherapy," Int. J. Radiat. Oncol. Biol. Phys. **52**, 1389-1399 (2002).

16 Y. Tsunashima, T. Sakae, Y. Shioyama, K. Kagei, T. Terunuma, A. Nohtomi, Y. Akine, "Correlation between the respiratory waveform measured using a respiratory sensor and 3D tumor motion in gated radiotherapy," Int. J. Radiat. Oncol. Biol. Phys. **60** (2004).

17 J.D.P. Hoisak, K. Sixel, R. Tirona, P.C.F. Cheung, J. Pignol, "Correlation of lung tumor motion with external surrogate indicators of respiration." Int. J. Radiat. Oncol. Biol. Phys. **60**, 1298-1306 (2004).

18 H. Shirato, S. Shimizu, T. Shimizu, T. Nishioka, K. Miyasaka, "Real-time tumour-tracking radiotherapy," Lancet **353**, 1331-1332 (1999).

19 H. Shirato, S. Shimizu, T. Kunieda, K. Kitamura, M. van Herk, K. Kagei, T. Nishioka, S. Hashimoto, K. Fujita, H. Aoyama, "Physical aspects of a real-time tumor-tracking system for gated radiotherapy," International Journal of Radiation Oncology Biology Physics **48**, 1187-1196 (2000).

20 H. Shirato, T. Harada, T. Harabayashi, K. Hida, H. Endo, K. Kitamura, R. Onimaru, K. Yamazaki, N. Kurauchi, T. Shimizu, "Feasibility of insertion/implantation of 2.0-mm-diameter gold internal fiducial markers for precise setup and real-time tumor tracking in radiotherapy," International Journal of Radiation Oncology* Biology* Physics **56**, 240-247 (2003).

21 S. Shimizu, H. Shirato, K. Kitamura, N. Shinohara, T. Harabayashi, T. Tsukamoto, T. Koyanagi, K. Miyasaka, "Use of an implanted marker and real-time tracking of the marker for the positioning of prostate and bladder cancers," International Journal of Radiation Oncology* Biology* Physics **48**, 1591-1597 (2000).

22 S. Shimizu, H. Shirato, S. Ogura, H. Akita-Dosaka, K. Kitamura, T. Nishioka, K. Kagei, M. Nishimura, K. Miyasaka, "Detection of lung tumor movement in real-time tumor-tracking radiotherapy* 1," International Journal of Radiation Oncology* Biology* Physics **51**, 304-310 (2001).

23 T. Harada, H. Shirato, S. Ogura, S. Oizumi, K. Yamazaki, S. Shimizu, R. Onimaru, K. Miyasaka, M. Nishimura, H. Dosaka-Akita, "Real-time tumor-tracking radiation therapy for lung carcinoma by the aid of insertion of a gold marker using bronchofiberscopy," Cancer **95**, 1720-1727 (2002).

24 X. Tang, G.C. Sharp, S.B. Jiang, "Fluoroscopic tracking of multiple implanted fiducial markers using multiple object tracking," Phys. Med. Biol. **52**, 4081 (2007).

25 P.R. Poulsen, W. Fledelius, P.J. Keall, E. Weiss, J. Lu, E. Brackbill, G.D. Hugo, "A method for robust segmentation of arbitrarily shaped radiopaque structures in cone-beam CT projections," Med. Phys. **38**, 2151 (2011).

26 Y. Cui, J. Dy, G. Sharp, B. Alexander, S. Jiang, "Multiple template-based fluoroscopic tracking of lung tumor mass without implanted fiducial markers." Phys. Med. Biol. **52**, 6229-6242 (2007).

27 Q. Xu, R.J. Hamilton, R.A. Schowengerdt, B. Alexander, S.B. Jiang, "Lung tumor tracking in fluoroscopic video based on optical flow," Med. Phys. **35**, 5351 (2008).

28 Q. Xu, R.J. Hamilton, R.A. Schowengerdt, S.B. Jiang, "A deformable lung tumor tracking method in fluoroscopic video using active shape models: a feasibility study," Phys. Med. Biol. **52**, 5277 (2007).

29 R.I. Berbeco, H. Mostafavi, G.C. Sharp, S.B. Jiang, "Towards fluoroscopic respiratory gating for lung tumours without radiopaque markers," Phys. Med. Biol. **50**, 4481 (2005).

30 Y. Cui, J.G. Dy, B. Alexander, S.B. Jiang, "Fluoroscopic gating without implanted fiducial markers for lung cancer radiotherapy based on support vector machines," Phys. Med. Biol. **53**, N315 (2008).

31 R. Li, J.H. Lewis, L.I. Cerviño, S.B. Jiang, "A feasibility study of markerless fluoroscopic gating for lung cancer radiotherapy using 4DCT templates," Phys. Med. Biol. **54**, N489 (2009).

32 G.D. Hugo, J. Liang, D. Yan, "Marker-free lung tumor trajectory estimation from a cone beam CT sinogram," Phys. Med. Biol. **55**, 2637 (2010).

33 J.H. Lewis, R. Li, W.T. Watkins, J.D. Lawson, W.P. Segars, L.I. Cerviño, W.Y. Song, S.B. Jiang, "Markerless lung tumor tracking and trajectory reconstruction using rotational cone-beam projections: a feasibility study," Phys. Med. Biol. **55**, 2505 (2010).

34 Y. Yang, Z. Zhong, X. Guo, J. Wang, J. Anderson, T. Solberg, W. Mao, "A novel markerless technique to evaluate daily lung tumor motion based on conventional cone-beam CT projection data," International Journal of Radiation Oncology* Biology* Physics **82**, e749-e756 (2012).

35 C. Shieh, P.J. Keall, Z. Kuncic, C. Huang, I. Feain, "Markerless tumor tracking using short kilovoltage imaging arcs for lung image-guided radiotherapy," Physics in medicine & biology **60**, 9437-9454 (2015).

36 P. Poulsen, B. Cho, K. Langen, P. Kupelian, P. Keall, "Three-dimensional prostate position estimation with a single x-ray imager utilizing the spatial probability density." Phys. Med. Biol. **53**, 4331-4353 (2008).

37 A. Fitch, A. Kadyrov, W.J. Christmas, J. Kittler, "Orientation correlation," presented at British Machine Vision Conference.

38 P. Pérez, M. Gangnet, A. Blake, "Poisson image editing," presented at ACM Transactions on Graphics (TOG).

39 Y. Zhang, L. Zhang, X.R. Zhu, A. Lee, M. Chambers, L. Dong, "Reducing metal artifacts in cone-beam CT images by preprocessing projection data." Int. J. Radiat. Oncol. Biol. Phys. **67**, 924 (2007).

40 Y. Yang, Z. Zhong, X. Guo, J. Wang, J. Anderson, T. Solberg, W. Mao, "A novel markerless technique to evaluate daily lung tumor motion based on conventional cone-beam CT projection data," International Journal of Radiation Oncology* Biology* Physics **82**, e749-e756 (2012).

41 N.O. Roman, W. Shepherd, N. Mukhopadhyay, G.D. Hugo, E. Weiss, "Interfractional Positional Variability of Fiducial Markers and Primary Tumors in Locally Advanced Non-Small-Cell Lung Cancer During Audiovisual Biofeedback Radiotherapy," International Journal of Radiation Oncology* Biology* Physics **83**, 1566-1572 (2012).